HIGH ANGULAR RESOLUTION DIFFUSION-WEIGHTED MAGNETIC RESONANCE IMAGING: ADAPTIVE SMOOTHING AND APPLICATIONS

A Dissertation
Presented to
The Academic Faculty

by

Nader S. Metwalli

In Partial Fulfillment
of the Requirements for the Degree
Doctor of Philosophy in the
School of Biomedical Engineering

Georgia Institute of Technology
August 2010

HIGH ANGULAR RESOLUTION DIFFUSION-WEIGHTED MAGNETIC RESONANCE IMAGING: ADATIVE SMOOTHING AND APPLICATIONS

Approved by:

Dr. Xiaoping Hu, Advisor
School of Biomedical Engineering
Georgia Institute of Technology
School of Medicine
Emory University

Dr. John D. Carew, Co-advisor
R. S. Dickson Institute of Health Studies
Carolinas HealthCare System
School of Public Health
Emory University

Dr. Diego Martin
School of Medicine
Emory University

Dr. Michael Benatar
School of Medicine
EmoryUniversity
School of Public Health
Emory University

Dr. John Oshinski
School of Biomedical Engineering
Georgia Institute of Technology
School of Medicine
Emory University

Date Approved: July 2nd, 2010

ACKNOWLEDGEMENTS

I would like to express my deepest gratitude to both my advisors, Dr. Xiaoping Hu and Dr. John D. Carew, for their continued guidance, support and patience throughout my graduate experience. They both enabled me to pursue my research interests and my knowledge has grown considerably under their mentorships. I am also grateful to my committee, Dr. Diego Martin, Dr. Michael Benatar and Dr. John Oshinski for their input, feedback and advice throughout my dissertation research.

I have had the privilege of working in two outstanding labs: the Biomedical Imaging Technology Center (BITC) of Georgia Tech / Emory University and the Magnetic Resonance Research Lab of Emory University's School of Medicine. I would like to thank all members of both labs, past and present, for their support. In particular, I would like to thank Dr. Xiangyang (Shawn) Ma, Danli Wang, Dr. Omar Zurkiya, Dr. Keith Heberlein, Dr. Scott Peltier, Dr. Zhihao Li, Dr. Lei Zhou, Dr. George (Andy) James, Dr. Tiejun Zhao, Dr. Gopi Deshpande, Dr. Roger Nana, Dr. Christopher B. Glielmi, Jaemin Shin, Dr. Richard Cameron Craddock, Dr. Zhi Yang, Dr. Govind Nair, Dr. Jaekeun Park, Katrina Gourdet and Robert Smith from BITC for their support. And from the Magnetic Resonance Research Lab, I would also like to thank Dr. Brandon

Fornwalt, Dr. Daniel Karolyi, Ian Campbell, Jonathan Suever, and Margaret Duello for their support and advice.

I am indebted to Dr. Stephen M. LaConte and Dr. Yasser M. Kadah for their advice and guidance especially in my first graduate years.

Special thanks go to Dr. Xianhong Xie, Dr. Maxime Descoteaux, Dr. Christopher Hess, and Dr. Pratik Mukherjee for sharing their experiences and helpful discussions.

I am profoundly grateful to my entire family, especially mother, father, brother, wife Sarah, and my sons, Yahya and Karim for their unwavering love, understanding, encouragement, and moral support in all my endeavors.

This work was supported in part by the National Institutes of Health (RO1 EB002009), the National Institutes of Health / National Institute on Drug Abuse (DA017795-01), the Georgia Research Alliance, an Emory University Faculty Distinction Award to John D. Carew, and the Wallace H. Coulter Department of Biomedical Engineering at Georgia Tech and Emory University. This research was also supported in part by an Emory University Research Committee grant, an Emory University Radiology / Georgia Tech Biomedical Engineering seed grant, the amyotrophic lateral sclerosis association (ID 1712).

TABLE OF CONTENTS

LIST OF TABLES

LIST OF FIGURES

Page

LIST OF ABBREVIATIONS

2D	two-dimensional
3D	three-dimensional
ADC	apparent diffusion coefficient or constant
ALS	amyotrophic lateral sclerosis
ALSFRS-R	revised ALS functional rating scale
CC	corpus callosum
CR	corona radiata
CST	corticospinal tract
DSI	diffusion spectrum imaging
DTI	diffusion-weighted imaging
DWI	diffusion tensor imaging
EPI	echo planar imaging
FA	fractional anisotropy
FVC	forced vital capacity
FOV	field-of-view
FRT	Funk-Radon transform
FT	Fourier transform
GCV	generalized cross-validation
HARDI	high angular resolution diffusion-weighted imaging
IC	internal capsule
IRB	institutional review board
LMN	lower motor neuron
MD	mean diffusivity

MNI	Montreal Neurological Institute
MPRAGE	magnetization prepared rapid gradient echo
MR	magnetic resonance
MRI	magnetic resonance imaging
MSE	mean squared error
NMR	nuclear magnetic resonance
ODF	orientation distribution function
PDE	partial differential equation
PDF	probability density function
PGSE	pulsed-gradient spin echo
QBI	*q*-ball imaging
RA	relative anisotropy
ROI	region-of-interest
RF	radio frequency
sRBFs	spherical radial basis functions
SHT	spherical harmonic transform
SLF	superior longitudinal fasiculus
SNR	signal-to-noise ratio
TBSS	tract-based spatial statistics
TE	echo time
TR	repetition time
UMN	upper motor neuron

LIST OF SYMBOLS

b	diffusion weighting
b0	image with negligible diffusion weighting
δ	duration of gradient
D	self-diffusion coefficient
$\boldsymbol{D}$	diffusion tensor
$E(\mathbf{q})$	diffusion signal
$\mathbf{g}$	diffusion-encoding magnetic field gradient
γ	nuclear gyromagnetic ratio for water protons
$\mathbf{I}$	interpolation reproducing kernel
$J(u)$	squared norm of a Laplace-Beltrami operation on function u
λ	regularization or smoothing parameter
$\hat{\lambda}$	generalized cross-validation estimate of smoothing parameter
$\lambda_{\|\|}$	axial diffusivity
$\lambda_{\perp}$	radial diffusivity
l	spherical harmonic expansion order
n	number of diffusion encoding sampling directions
ϕ	longitude
$\mathbf{P}$	Kronecker tensor product matrix
$\mathbf{q}$	diffusion-encoding spatial modulation
$R(\theta)$	axially symmetric response function
$R(P,P_i)$	reproducing kernel
σ_i	interpolation kernel width
t	diffusion time

θ	latitude
T_1	spin-lattice relaxation time
T_2	spin-spin relaxation time
u	smoothing splines on the sphere function
z	sampled noisy diffusion-weighted data
Z	normalization constant
ζ	angle between points P and P_i

SUMMARY

Diffusion-weighted magnetic resonance imaging (MRI) has allowed unprecedented non-invasive mapping of brain neural connectivity in vivo by means of fiber tractography applications. Fiber tractography has emerged as a useful tool for mapping brain white matter connectivity prior to surgery or in an intraoperative setting. The advent of high angular resolution diffusion-weighted imaging (HARDI) techniques in MRI for fiber tractography has allowed mapping of fiber tracts in areas of complex white matter fiber crossings. Raw HARDI images, as a result of elevated diffusion-weighting, suffer from depressed signal-to-noise ratio (SNR) levels. The accuracy of fiber tractography is dependent on the performance of the various methods extracting dominant fiber orientations from the HARDI-measured noisy diffusivity profiles. These methods will be sensitive to and directly affected by the noise. In the first part of the thesis this issue is addressed by applying an objective and adaptive smoothing to the noisy HARDI data via generalized cross-validation (GCV) by means of the smoothing splines on the sphere method for estimating the smooth diffusivity profiles in three dimensional diffusion space. Subsequently, fiber orientation distribution functions (ODFs) that reveal dominant fiber orientations in fiber crossings are then reconstructed from the smoothed diffusivity profiles using the Funk-Radon transform. Previous ODF smoothing techniques have been subjective and non-adaptive to data SNR. The GCV-

smoothed ODFs from our method are accurate and are smoothed without external intervention facilitating more precise fiber tractography.

Diffusion-weighted MRI studies in amyotrophic lateral sclerosis (ALS) have revealed significant changes in diffusion parameters in ALS patient brains. With the need for early detection of possibly discrete upper motor neuron (UMN) degeneration signs in patients with early ALS, a HARDI study is applied in order to investigate diffusion-sensitive changes reflected in the diffusion tensor imaging (DTI) measures axial and radial diffusivity as well as the more commonly used measures fractional anisotropy (FA) and mean diffusivity (MD). The hypothesis is that there would be added utility in considering axial and radial diffusivities which directly reflect changes in the diffusion tensors in addition to FA and MD to aid in revealing neurodegenerative changes in ALS. In addition, applying adaptive smoothing via GCV to the HARDI data further facilitates the application of fiber tractography by automatically eliminating spurious noisy peaks in reconstructed ODFs that would mislead fiber tracking.

CHAPTER 1

INTRODUCTION

1.1 General Introduction

Fiber tractography has emerged as a useful tool for mapping brain white matter prior to surgery or in an intraoperative setting. The advent of high angular resolution diffusion-weighted imaging (HARDI) techniques in MRI for fiber tractography have allowed mapping of fiber tracts in areas of complex architecture. HARDI data are customarily noisy with low signal-to-noise (SNR) ratios prompting some smoothing or regularization in fiber orientation distribution function (ODF) reconstruction techniques. Past regularization or smoothing techniques of ODFs have been subjective and non-adaptive to data SNR. The first part of this thesis addresses this issue by applying an objective and adaptive smoothing to inherently noisy HARDI data via generalized cross-validation (GCV) by means of the smoothing splines on the sphere method prior to ODF reconstruction. The resulting ODFs are smoothed out without subjective intervention.

Past diffusion tensor imaging (DTI) MRI studies in amyotrophic lateral sclerosis (ALS) have demonstrated significant changes in diffusion parameters in ALS patient brains. In early stages of the disease, upper motor neuron (UMN) signs may be very discrete and difficult to detect with currently used DTI measures, fractional anisotropy (FA) and mean diffusivity (MD). It is hypothesized that there may be an added utility in considering directional diffusivities from the diffusion tensor, axial diffusivity and radial

diffusivity, in addition to the more commonly used measures FA and MD to aid in revealing neurodegenerative changes in early ALS. In the second part of this thesis, this hypothesis is tested using voxel-based and region-of-interest analysis techniques.

1.2 Statement of Thesis

Revealing complex white matter fiber crossings in the brain in connection with fiber tractography applications requires that high angular resolution diffusion-weighted imaging (HARDI) scans be acquired with high diffusion-weighting. As a result raw HARDI images have lower signal-to-noise ratios (SNR) than typical diffusion-weighted images. HARDI data are diffusion-weighted samples on the sphere of an originally smooth diffusion profile in each imaging voxel with an added nuisance noise term. The accuracy of fiber tractography is dependent on the performance of the various methods extracting orientational structure information from the diffusion profile. These methods will be sensitive to and directly affected by the noise. This thesis first aims to assess the applicability of the smoothing splines on the sphere estimation problem to HARDI. An objective and adaptive means of smoothing HARDI data via generalized cross-validation (GCV) is applied and analyzed in estimating the smooth diffusivity profiles in three dimensional diffusion space.

1.2.1 Chapter 2: Adaptive Smoothing of High Angular Resolution Diffusion-weighted Imaging Data by Generalized Cross-validation for Q-Ball Orientation Distribution Function Reconstruction

Noisy diffusivity profiles will lead to noisy reconstructed orientation distribution functions (ODFs) with spurious peaks that would ultimately mislead fiber tractography. In this chapter, an objective and adaptive means of smoothing HARDI data is applied. A GCV criterion is minimized to determine the amount of smoothing to be applied in the smoothing splines on the sphere method. Subsequently, a fiber ODF technique based on the Funk-Radon transform (FRT) is applied to reconstruct smooth ODFs with no need for subjective intervention.

1.2.2 Chapter 3: Towards an Objective Marker for Upper Motor Neuron Involvement in Amyotrophic Lateral Sclerosis: A High Angular Resolution Diffusion-weighted Imaging Study

With the need for early detection of possibility discrete upper motor neuron (UMN) degeneration signs in patients with early amyotrophic lateral sclerosis (ALS), a HARDI study is applied in this chapter in order to investigate diffusion-sensitive changes reflected in the DTI measures axial and radial diffusivities as well as the more commonly used FA and MD. The hypothesis is that there may be an added utility in considering axial diffusivity and radial diffusivity in addition to the more commonly used measures FA and MD to aid in revealing neurodegenerative changes in early ALS.

1.3 Background

Molecular diffusion referring to the random motion of particles suspended in a fluid is termed ‘Brownian motion’ after the Scottish botanist, Robert Brown. In 1827,

Brown while studying *Clarckia pulchella* pollen particles suspended in water under a microscope observed 'many of them very evidently in motion'(1) . He went on to attribute such motion to the particles themselves and not resulting from currents in the fluid or from the fluids' evaporation. It was not until Albert Einstein in 1905 who in his investigations on the theory of Brownian motion attributed it formally to the molecular theory of heat stating that microscopic bodies suspended in a liquid will undergo movement with magnitudes easily observed under a microscope due to molecular motions of heat (2,3). It is this microscopic phenomenon, Brownian motion, which is responsible for the macroscopical effect of diffusion. This encompasses the diffusion of a certain substance in another substance or the diffusion of that substance in its own medium as the diffusion of water in water. This latter case is termed self-diffusion. In the following we review, briefly, the history of diffusion measurements with nuclear magnetic resonance (NMR) to the developments leading to *in vivo* imaging of diffusion with MRI.

1.3.1 Diffusion and Nuclear Magnetic Resonance

In the case of the self-diffusion of water in a glass container, the water molecules undergo Brownian motion in which their motion is completely random. The water molecules are also described as undergoing a random walk. The movement of the molecules is only constrained by the walls of the container. In statistical terms, this random motion is best described by a displacement distribution (4) depicting the proportion of molecules undergoing displacement in a specific direction and to a specific

extent. The displacement distribution for self-diffusion water molecules undergoing free unrestricted diffusion is a three-dimensional Gaussian function.

Of the early mentions of diffusion and its effects in the nuclear magnetic resonance setting comes from Hahn in his ground breaking paper introducing the spin echo concept (5). He notes that the self-diffusing liquid molecules contribute to an added attenuation in the signal over the decay due to just T_1 and T_2 relaxation effects that he attributes to the inhomogeneities in the main static magnetic field. He further adds that the relative values of the self-diffusion coefficient D could be measured. Shortly after, Carr and Purcell (6) derived equations estimating the diffusion constant in NMR and reported as an application measuring the self-diffusion constant of water at 25°C using a variation of Hahn's spin echo method.

Torrey was the early pioneer who added diffusion terms in the original Bloch equations governing the magnetic resonance (MR) signal dynamics that represent the effects of self-diffusion (7). These additional terms would formally lead to an added attenuation of the MR signal. He derived equations for estimating the attenuated signal amplitude due to self-diffusion. In 1965, Stejskal and Tanner provided a derivation to the effect of applying a time-dependent magnetic field on the spin-echo experiment in the presence of spin (proton) diffusion (8). In their seminal paper, they introduced the theory, developed the methodology, describe an apparatus, and essentially laid the groundwork for special sequences known now as the 'pulsed-gradient spin echo' (PGSE) sequences used in imaging diffusion today. They measured, using their new technique, the self-

diffusion coefficients for both water at 25.5°± 0.5°C and glycerol at 26°± 1°C. The study of restricted diffusion and flow using pulsed-magnetic field gradients in spin echoes immediately followed (9).

1.3.1.1 The pulsed-gradient spin echo (PGSE) sequence

Stejskal and Tanner (8) offer an eloquent description of the main physical processes occurring while the PGSE sequence is applied. Assuming there are stationary and moving proton spins in the volume to be imaged. Applying a gradient radio frequency (RF) pulse for a specified duration after the 90° RF excitation pulse will give all spins, stationary and mobile, an equal amount of phase, i.e., all spins will have the same phase difference, as all spins started off having the same phase. After a certain time passes, the mobile spins will have moved, i.e., protons have diffused in a random-walk to different locations in the volume. Since the phase added to proton spins in an MR experiment depends on the locations of those spins, applying a gradient RF pulse after the 180° pulse will cause the stationary spins to forfeit all the phase they gained when the first gradient pulse was applied whereas the mobile spins will not. In the absence of diffusion, a second gradient pulse, aided by the 180° pulse, would undo the effect of the first exactly. The diffusion of some nuclei causes the refocusing to be incomplete. Stejskal and Tanner explain the PGSE sequence as it would apply to one-dimensional NMR but the physical processes occurring would still apply in 2D MRI. Further details regarding use of the PGSE sequence in 2D imaging will be presented in a following section.

1.3.2 Diffusion and Magnetic Resonance Imaging

With Peter Lauterbur's insight of using magnetic field gradients to achieve spin spatial localization, magnetic resonance imaging (MRI) was born in the 1970s (10). It was not until 1985, however, when diffusion MR imaging was introduced by LeBihan and Breton (11). This development allowed NMR imaging to be used to measure the diffusivity of not just water but of other metabolites *in vivo* noninvasively at microscopic scales. Diffusion-weighted imaging (DWI), as it is sometimes called, measures an apparent diffusion coefficient or constant (ADC) in each voxel from a series of diffusion-weighted images. The effect of diffusion on the MRI signal, as was previously mentioned, is an attenuation which was found to depend exponentially on the ADC in a voxel and on a scalar *b*-factor characterizing the gradient pulses (timing, amplitude, shape) used in the imaging sequence. The ADC is estimated for each voxel from that relation. Essentially in DWI, in each voxel, it is assumed that the water three-dimensional displacement is spherical. The presumed and widely accepted assumption is that the water molecules in their diffusion throughout the body encounter microscopic structures. It was observed that in highly structured tissues such as brain white matter, the ADC varied as the angle between the fiber-tract axis and the applied magnetic field gradient was changed (12). The ADC was observed the largest when the diffusion-sensitizing gradient was parallel to the fiber direction and smallest when it was applied perpendicular to it (13). Anisotropic diffusion was first shown to exist in the muscle by Cleveland *et al.* (14). In highly oriented structures like white matter, it is assumed that there would be greater hindrance to diffusion across rather than along the fiber tract axis. As a result, the direction of fastest diffusion is assumed to coincide with the orientation of the underlying

fibers. This was shown to be the case, using manganese-enhanced MRI, in the optic tract of the rat (15). It was clear that a simple scalar, such as, the ADC could not accurately characterize diffusion in an anisotropic tissue and that lead to the introduction of diffusion tensor imaging (13).

1.3.3 Diffusion Tensor Imaging (DTI)

Diffusion Tensor Imaging (DTI) was introduced by Basser *et al.* (13) to address the inadequacy of estimating a single scalar to characterize anisotropic diffusion. Diffusion-weighted MRI analysis has seen ever increasing attention and focus ever since the introduction of DTI. The ADC estimate was replaced by an effective diffusion tensor (16) that attempts to characterize the diffusion in both anisotropic and isotropic media by a rank-2 tensor. DTI attempts to noninvasively reveal tissue microstructure and organization at scales unattainable from ordinary structural magnetic resonance images. DTI has become a very commonly used approach in modeling diffusion. Estimating a rank-2 tensor provides a simple and powerful model that is appropriate for the majority of brain voxels. Tensor-derived anisotropy indices such as Fractional Anisotropy (FA) and Relative Anisotropy (RA) (17) have also become a staple in characterizing diffusion anisotropy in the research and clinical communities.

The main underlying assumption of the DTI model is that the diffusion process follows a multivariate Gaussian distribution, with the diffusion tensor as the covariance matrix to be estimated. Contours of the multivariate normal density function form ellipsoids (18). The shape and orientation of the ellipsoid is directly determined by the

covariance matrix (the diffusion tensor) through its principle directions (eigenvectors) and variances (eigenvalues) along those principle directions. This multivariate Gaussianity assumption, however, is not always satisfied. One particular case is where voxels in regions of high tissue complexity contain multiple fiber orientations and intersections (19). The multivariate normal, and thus the diffusion tensor, can have only one directional maximum thus one orientation maximum pointing in the direction where maximum diffusion occurs. Multiple fiber orientations are expected. These multiple orientations are due to fibers crossing or diverging within the millimeter scale voxels. Since DTI can only fit a single Gaussian to the underlying measurements, multiple orientations are problematic. It will incorrectly estimate a single fiber orientation as the mean of the underlying fiber directions. This average direction will obviously not be representative of the true fiber directions (20). Accordingly in these situations, the tensor model is inadequate.

1.3.4 High Angular Resolution Diffusion-weighted Imaging (HARDI)

High angular resolution diffusion-weighted imaging (HARDI) was proposed as a method that can reveal non-Gaussian diffusion (21). Capturing complex fiber crossings with HARDI often requires higher diffusion-weightings than typically used in DTI. The diffusion time allotted for the spins movement is extended to allow them further time to diffuse and prod the underlying microstructure. With higher diffusion-weightings, raw HARDI data have even lower SNR levels than typical DTI data. Tuch *et al.* (22) early on proposed modeling the diffusion signal as a finite mixture of Gaussian diffusion processes in slow exchange so as to reveal intravoxel white matter fiber heterogeneity.

The underlying mixture of tensors was solved for using a gradient descent scheme and the results for a mixture of two rank-2 tensors were only reported as the results for 3 tensors were unstable (22). This mixture modeling approach entailed a number of assumptions. The first assumption was that diffusion in each fiber population followed a single, independent Gaussian distribution. This may be the case if the fibers only cross in the voxel but that is not necessarily the case when the fibers actually merge. The second assumption was that there was no water exchange between fiber populations (19, 22).

Frank (23) presented the first model free approach to characterize anisotropy in HARDI images. He presented a simple algorithm based on the variance of the estimated ADC as a function of the diffusion measurement direction, which indicates where diffusion deviates from being isotropic. The measure estimated was termed the spherical diffusion variance. This method's inherent disadvantage is that it fails to characterize the diffusion structure and that it is sensitive to artifacts contributing to the variance. Another major disadvantage is that the diffusion anisotropy is not quantified in a very meaningful way; this method does not allow the quantitation of the magnitude or the direction of diffusion. Spherical diffusion variance does, on the other hand, have the advantage of identifying anisotropy regions that are not well characterized by the single tensor model.

Frank (24) later recognized that the HARDI measurements were made along directions covering the range of the spherical coordinates (θ, Φ). This influenced him to parameterize the ADC by the spherical coordinates. Tensors represented this way are called spherical tensors. The complex spherical harmonics form a complete orthonormal

basis. This allows an expansion of the ADC with a Laplace series. The coefficients of this expansion are determined in a way that is analogous to a Fourier decomposition of sinusoidal functions, but on the unit sphere. That was called the spherical harmonic transform (SHT) of the measured ADC. Isotropic diffusion falls in the zero'th harmonic, single-fiber diffusion in the zero'th and second harmonics, and multiple-fiber diffusion approximately in the zero'th, second, and fourth harmonics. The odd harmonics represent anti-symmetric properties in the diffusion profile – attributed to eddy currents and other artifacts – and thus were discarded. The coefficients of the Laplace series, representing the diffusivity profile, are truncated to include only the most significant terms. The main drawbacks of this approach are that the computation of the SHT is difficult, rotationally variant, and a need to select the truncation point.

Alexander *et al.* (19) presented a systematic procedure for using spherical harmonics to model the ADC profiles. The main drawback of a spherical harmonic based modeling methods is the need to truncate the harmonic series above a certain harmonic, typically the sixth or in some studies the eight. Inclusion of higher harmonics will lead to an over fitting of the data and can introduce the undesirable high frequency noise components.

In an attempt to remedy DTI's rank-2 tensor shortfall with non-Gaussian diffusion, generalized diffusion tensor imaging was introduced (25) by which Cartesian tensors of arbitrary ranks, not limited to just the rank-2 tensor, are estimated from the HARDI measurements. The generalized tensor approach made it unnecessary to calculate

the spherical harmonic coefficients of the Laplace series and the results were equivalent to those from the SHT. In a recent study, Minati *et al.* (26) showed using simulations and real HARDI data that elevating tensor rank in regions of intra-voxel orientational heterogeneity as in subcortical regions of the corona radiata, along the superior longitudinal fasiculus, and in the radiations of the genu of the corpus callosum, and in other regions, apparently increased the estimated anisotropy. They also reported that that was even true for regions of mono-modal diffusion patterns as the corpus callosum and the anterior limb of the internal capsule.

More recently a model-independent method for reconstructing the HARDI measurements by means of a spherical tomographic inversion using the spherical Radon transform was presented (27). The new imaging method was called *q*-ball imaging (QBI) (28) and was capable of resolving multiple intravoxel fiber orientations and makes no assumptions on the underlying diffusion process. The principles upon which QBI is based are presented in the following.

1.3.5 q-Space Imaging

In q-space imaging, using a PGSE sequence, nuclei are given a spatial label at one instant of time, and then that labeling is checked to see if the nuclei have moved. By measuring the label shift, the nuclei's motion can be deduced (29). It is that label shift that is the basic principle upon which q-space imaging methods work. Unlike imaging in the k-space where the stationary proton spins are imaged, q-space imaging methods depend on moving protons to create images. With q-space imaging methods, the

microscopic three-dimensional probability density function (diffusion function) can be directly measured in each voxel. The probability density function (PDF) (or diffusion function) is given by

$$P(\mathbf{r}) = (4\pi t)^{-3/2} |\mathbf{D}|^{-1/2} \exp\left(-\mathbf{r}^T \mathbf{D}^{-1} \mathbf{r}/(4t)\right) \quad [1.1]$$

where $\boldsymbol{D}$ is the diffusion tensor (covariance matrix), | | denotes determinant., t is the diffusion time, and $\mathbf{r}=\mathbf{r_1}-\mathbf{r_0}$, where $\mathbf{r_1}$ is the final position of the nuclei after time t, and $\mathbf{r_0}$ is the initial nuclei position. The multivariate three-dimensional normal, $P(\mathbf{r})$, is the net displacement that is measured from the PGSE sequence. $P(\mathbf{r})$ depends on the net displacement, $\mathbf{r}$, and not the initial position, $\mathbf{r_0}$, and also depends on the direction of the displacement. Q-space imaging methods are based on the Fourier relationship between the diffusion function and the diffusion MR signal $E(\mathbf{q})$, first mentioned by Stejskal. This relationship is the following,

$$P(\mathbf{r}) = F[E(\mathbf{q})] \quad [1.2]$$

where F is the Fourier transform (FT) with respect to the experimental diffusion vector $\mathbf{q} = \gamma\delta\mathbf{g}$, γ is the nuclear gyromagnetic ratio for water protons, $\mathbf{g}$ is the diffusion-encoding magnetic field gradient, and δ is the duration of the gradient. Based on this Fourier relationship, the diffusion function can be directly reconstructed by the Fourier transform of the diffusion signal.

Q-space imaging methods have been applied in the past to characterize the microstructure of complex inanimate materials (30), biological tissue in vitro (31, 32), and small animals in vivo (33). One dimensional q-space imaging has also been applied in humans in vivo (34). In this study, the diffusion function is measured along only one spatial dimension.

1.3.5.1 Diffusion Spectrum Imaging (DSI)

Diffusion Spectrum Imaging (DSI) is based on q-space imaging and was proposed as a means to reveal the three dimensional diffusion function within each voxel through direct measurements (35). Diffusion-weighted images are acquired for several hundred values of diffusion-encoding spatial modulation **q** at points contained within an isotropic 3D grid within a spherical volume of radius *r* (35). In each voxel, the diffusion signals are a sampling, in 3D Fourier transform space, of the PDF. The main drawbacks to routine clinical use of DSI still remain in long acquisition times and the need for strong magnetic field gradients.

1.3.6 Orientation Distribution Function (ODF)

The orientation distribution function (ODF) is a 3D spherical function constructed to extract the dominant fiber orientations in the underlying voxel. Formally, the ODF is the radial projection of the 3D PDF onto the unit sphere. The term ODF was first coined by Wedeen *et al.* (35). It was introduced in order to by pass the need to estimate the entire PDF which requires excessive scan times and extensive computing requirements. One of the most basic ODFs is the ellipsoid formed by the eigenvalues and eigenvectors of the

diffusion tensor. The ODF only portraits the areas where the PDF has the most mass by forming peaks in those directions. These peaks are assumed to coincide with the underlying fiber directions (36). The peaks coinciding with the underlying fiber directions is of importance because standard methods such as DTI break down in areas of the brain where there is partial voluming or multiple fiber directions in a given voxel. As mentioned previously, DTI's underlying assumption is that the underlying diffusion occurring is Gaussian in nature and dictates that the tensor has only one single peak thus providing only a single fiber orientation estimate in every voxel. In regions of multiple fiber crossings within a voxel, the diffusion PDF will exhibit multiple peaks which the tensor in DTI will fail to capture. The ODF formed by the tensor would, in these cases, be an incomplete representation of the complexity of the white matter.

Tournier *et al.* (37) presented a simple method for fiber orientation distribution extraction. It assumes that the diffusion characteristics of all fiber populations found in the brain are identical and that variations in white matter FA attributable to a change in the diffusion profile are entirely due to partial volume effects. They assume that the diffusion-weighted signal attenuations that would be measured if a single coherently oriented fiber population was present in a voxel are represented by an axially symmetric response function $R(\theta)$. The different diffusion profiles found in the brain are merely a convolution of this response function with the fiber ODF. Through a series of spherical harmonic decompositions, the fiber ODF can be extracted by a spherical deconvolution with the assumed response function $R(\theta)$.

1.3.7 Q-Ball Imaging (QBI)

QBI attempts to capture an approximate picture of the diffusion PDF in each voxel without incurring the many drawbacks that initial q-space imaging methods presented (e.g., long scan times) and without any a priori assumptions. As mentioned previously, with the diffusion PDF being related to the diffusion signal by a Fourier relationship, a direct reconstruction of that diffusion function can be obtained by a Fourier transformation of a three dimensional lattice sampling of *q*-space (28). The three dimensional PDF does provide a complete picture of the tissue microstructure but for purposes of orientation structure mapping of the tissue, an approximation of that PDF showing just the orientation structure inherent in the diffusion function would be sufficient. This is described through the diffusion ODF. Deriving the ODF from a three dimensional lattice sampling of *q*-space has a number of limitations however. ODF extraction requires explicit calculation of the radial projections which would introduce artifacts in the mapping from Cartesian to spherical coordinates (28). It would be substantially more efficient to measure the diffusion ODF by directly sampling the diffusion signal on a spherical shell in diffusion reciprocal space. This forms the basis of QBI. Of the main characteristics that lead to the immediate appeal of the QBI method are model independence and linear estimation.

QBI reconstruction is based on the Funk Radon transform (FRT). The FRT is defined as a transform from the sphere to the sphere. Given a function on the sphere $f(\mathbf{w})$, where $\mathbf{w}$ is a unit vector, the FRT is defined as the integration over the corresponding

equator, i.e., the set of equatorial points in a plane perpendicular to **w**. Thus the FRT for a direction **u** is written as

$$FRT[f(\mathbf{w})](\mathbf{u}) = \int_{\mathbf{w}\in\mathbf{u}^{\perp}} f(\mathbf{w})d\mathbf{w} \qquad [1.3]$$

Tuch *et al.* (20) showed that the FRT of the diffusion signal gives a very close approximation to the ODF, i.e.,

$$\psi(\mathbf{u}) \approx \frac{1}{Z} FRT_{q_r}[E(\mathbf{q})] \qquad [1.4]$$

where q_r is the radius of the sampling shell and Z is a normalization constant (28). This means that the sum of the diffusion signals over an equator approximately gives the diffusion probability in the direction normal to the plane of the equator.

There have been a number of studies (38, 39) validating that the ODFs reconstructed using QBI truly reflect the underlying tissue microstructure most notably the work done by Perrin et al. (38) using a diffusion fiber crossing phantom in a clinical scanner.

One of the drawbacks to QBI is in the interpolation and smoothing kernel parameter selections. Tuch (28) addressed the issue of spherical Gaussian interpolation kernel degree selection by setting the interpolation degree to the one that gives a minimum condition number to the reconstruction interpolation matrix. However, the smoothing kernel width has been predominantly selected by the investigator (27, 28, 40).

The basis of selection is purely subjective and is based on which smoothing kernel width gives the best-reconstructed ODFs visually.

1.3.7.1 Q-Ball imaging (QBI) using the spherical harmonic basis

HARDI data are customarily acquired on single spherical shell in diffusion reciprocal space. Taking advantage of that spherical geometry in the data, Hess *et al.* presented an implementation of QBI using the spherical harmonic basis leading to an analytical solution for the ODF reconstruction (41). With their proposed approach, the ODF is represented as a linear combination of spherical harmonics. It is important to note that, a harmonic model order number needs to be selected for the expansion up to a maximum determined by the number of measured data points. Larger series orders are used in order to achieve the highest possible angular resolution however higher frequency harmonics are less reliably estimated from the measured data and could lead to the emergence of spurious peaks in the ODFs reconstructed (41). In the authors attempt to decrease sensitivity to noise, they used matrix regularization based on the Tikhonov method while solving for the spherical harmonic coefficients when a large harmonic order approximation was desired. However, the choice of the regularization parameter value was left at the discretion the investigator. Subsequently, Descoteaux et al. (42) presented a regularized analytical solution for QBI in the spherical harmonic basis based on the Laplace-Beltrami operator. This operator is defined on the unit sphere and is a measure of smoothness for functions on the unit sphere which was more appropriate. They showed that the Laplace-Beltrami regularization performs better than the Tikhonov regularization. Again, the smoothing parameter value they used was set a priori to

provide a good separation of 1-fiber from 2-fiber distributions over a large range of SNR and *b*-values in the experimental simulations (43).

1.3.8 Diffusion-weighted MRI Clinical Applications

One of the main reasons behind the appeal of using diffusion imaging in clinical applications is that it is truly quantitative (44). DWI has been used very successfully in the clinical diagnosis and characterization of acute ischemic lesions. With the advent of DTI, measures derived from the tensor garnered even more attention. The reason is rotationally invariant measures. These measures have values that are independent of the direction of the applied diffusion gradient, independent of the orientation of the tissue structure in each voxel, and independent of the laboratory frame of reference, and are estimated from the diffusion tensor (17). Specifically, the eigenvalues from the eigen decomposition of the tensor are the elements used in constructing such rotationally invariant scalars. In anisotropic tissue, such as white matter, the largest eigenvalue represents the diffusivity of water in the direction parallel to the fiber bundles. This eigenvalue has been called synonymously the axial diffusivity ($\lambda_{\parallel}$). The average of the two smallest eigenvalues was called the radial diffusivity ($\lambda_{\perp}$). Radial diffusivity or $\lambda_{\perp}$, measures water diffusion perpendicular to the axonal wall. Other measures include the mean diffusivity (MD), which is the average diffusion in a given voxel, and fractional anisotropy (FA), which measures the eccentricity, or degree of anisotropy (45, 46). FA and MD have become very popular in studying a wide variety of brain white matter pathologies. These include but are not limited to acute stroke (47), multiple sclerosis (48), primary lateral sclerosis and amyotrophic lateral sclerosis (ALS) (49).

1.3.8.1 Amyotrophic lateral sclerosis (ALS)

ALS, also known as Lou Gehrig's disease, is a progressive and ultimately fatal neurological disease. Neuropathological features in ALS include degeneration and eventual loss of the large motor neurons in the cortex, brainstem, and spinal cord as well as the degeneration of the corticospinal tract (CST) (49). Upper motor neurons (UMN) transmit messages from the brain to the motor neurons in the spinal cord; lower motor neurons (LMN) that in turn relay them to muscles. In ALS, both UMN and LMN degenerate. With no specific test for ALS, it remains a clinical diagnosis. Electromyography and motor unit number estimation are useful biomarkers of LMN dysfunction but there are currently no biological markers of UMN dysfunction. Particularly in the early stages of the disease, UMN degeneration signs may be very discrete. Although, FA and MD have been the widely used measures of choice in the past for DTI studies in ALS, they may not be the most appropriate in detecting subtle diffusion changes especially in early stages of UMN involvement in ALS. The utility of $\lambda_{\parallel}$ and $\lambda_{\perp}$ in early ALS needs to be investigated.

1.3.8.2 Axial ($\lambda_{\parallel}$) and radial diffusivity ($\lambda_{\perp}$) in studying white matter neuropathology

There has been a recent interest in using $\lambda_{\parallel}$ and $\lambda_{\perp}$ to provide more insight into specific diffusion changes occurring in the diffusion tensor (50, 51). In a mouse model of dysmyelination, Song *et al.* studied $\lambda_{\parallel}$ and $\lambda_{\perp}$ and found that the absence of myelin appeared to increase $\lambda_{\perp}$ but did not significantly affect $\lambda_{\parallel}$ (50). Several other studies with

the mouse model have suggested that $\lambda_{\parallel}$ and $\lambda_{\perp}$ may communicate diffusivity changes in white matter pathology (52-55). Of these changes specifically, demyelination seems to increase $\lambda_{\perp}$ while axonal damage is associated with decreased $\lambda_{\parallel}$. And even though the underlying mechanisms are still unclear, the speculation has been that with demyelination a loss in the myelin membrane integrity may permit increased water movement across the myelin layers (perpendicular to the long axis of the fiber) and with axonal loss and degeneration and loss of coherence in axonal organization, $\lambda_{\parallel}$ would decrease. In human studies, increased $\lambda_{\perp}$ was reported in the corpus callosum of subjects with Autism (51), in frontal white matter of patients with early Alzheimer's disease (56), in the genu of the corpus callosum of cocaine dependent subjects (57) and in the remaining white matter tracts of the corpus callosum after corpus callosotomy in epilepsy patients (58). In the last study by Concha *et al.*, their results seem to suggest a dynamism in the $\lambda_{\parallel}$ and $\lambda_{\perp}$ seen changes with an initial decrease in $\lambda_{\parallel}$ one week after surgery and little increase in $\lambda_{\perp}$ followed by larger increases in $\lambda_{\perp}$ and a normalizing or even increase in $\lambda_{\parallel}$ at 2-4 months post-surgery.

1.4 General Summary

This chapter first provided a brief historical overview of past efforts in measuring the molecular diffusion phenomenon using NMR and MRI. Furthermore, it summarized the current state of HARDI techniques utilized in fiber ODF reconstruction and associated challenges due to low SNR levels in HARDI for accurate ODF reconstruction. With continued developments in scanner hardware capabilities and the increased interest

in acquiring HARDI data routinely as the diffusion-weighted scan in subject protocols, the issue of HARDI data's inherently depressed levels of SNR and the detrimental effects that that has on ODF reconstruction for tractography applications needed appropriate addressing. The application of HARDI in a clinical setting on ALS patients is investigated with the goal of finding an objective marker for UMN involvement in early stages of the disease.

Chapters 2 and 3 are the main contributions of this thesis and are individually self-contained. Chapter 2 introduces an application of the smoothing splines on the sphere algorithm with objective and adaptive smoothing of the HARDI measured diffusivity profiles in three dimensional diffusion space. The resulting smoothed diffusivity profiles are subsequently used for fiber ODF reconstruction based on the FRT in QBI and are compared with ODFs reconstructed using existing QBI methods. Chapter 3 applies HARDI in subjects clinically diagnosed with ALS at the early stages of the disease to investigate diffusion-sensitive changes in UMN white matter towards identifying objective markers for UMN involvement in early ALS.

1.5 References

1. Brown R. A brief account of microscopical observations made in the months of June, July and August, 1827, on the particles contained in the pollen of plants; and on the general existence of active molecules in organic and inorganic bodies. Edinburgh new Phiolosophical Journal 1828(July-September): 358-371.

2. Einstein A. Über die von der molekularkinetischen Theorie der Wärme geforderte Bewegung von in ruhenden Flüssigkeiten suspendierten Teilchen. Annalen der Physik 1905; 17: 549-560.

3. Einstein A. Investigations on the theory of Brownian motion. R. Furthe ADC, editor. Dover, New York: Dover publications; 1956.

4. Hagmann P, Jonasson L, Maeder P, Thiran JP, Wedeen VJ, Meuli R. Understanding diffusion MR imaging techniques: from scalar diffusion-weighted imaging to diffusion tensor imaging and beyond. Radiographics 2006; 26 Suppl 1: S205-223.

5. Hahn EL. Spin Echoes. Pysical Review 1950; 80: 580-594.

6. H. Y. Carr EMP. Effects of diffusion on free precession in nuclear magnetic resonance experiments. Physical Review 1954; 94(3): 630-638.

7. Torrey H. Bloch equations with diffusion terms. Physical Review 1956; 104(3): 563-565.

8. Stejskal E, Tanner JE. Spin diffusion measurements: Spin echoes in the presence of a time-dependent field gradient. J Chem Phys 1965; 42(1): 288-292.

9. Stejskal E. Use of spin echoes in a pulsed magnetic-field gradiant to study restricted diffusion and flow. J Chem Phys 1965; 43(10): 3597-3603.

10. Lauterbur P. Image formation by induced local interactions: Examples employing nuclear magnetic resonance. Nature 1973; 242: 190-191.

11. Le Bihan D, Breton E. Imagerie de diffusion *in vivo* par resonance magnetique nucleaire. CR Acad Sci Paris 1985; 301: 1109-1112.

12. Chenevert TL, Brunberg JA, Pipe JG. Anisotropic diffusion in human white matter: demonstration with MR techniques in vivo. Radiology 1990; 177(2): 401-405.

13. Basser PJ, Mattiello J, LeBihan D. MR diffusion tensor spectroscopy and imaging. Biophys J 1994; 66(1): 259-267.

14. Cleveland GG, Chang DC, Hazelwood CF. Nuclear magnetic resonance measurements of skeletal muscle. Anisotropy of the diffusion coefficient of the intracellular water. J Biophys. 1976, (16): 1043-1053.

15. Lin CP, Tseng WY, Cheng HC, Chen JH. Validation of diffusion tensor magnetic resonance axonal fiber imaging with registered manganese-enhanced optic tracts. NeuroImage 2001;14(5):1035-1047.

16. Basser PJ, Mattiello J, LeBihan D. Estimation of the effective self-diffusion tensor from the NMR spin echo. J Magn Reson, 1994; Series B 103: 247-254.

17. Pierpaoli C, Basser PJ. Toward a quantitative assessment of diffusion anisotropy. Magn Reson Med, 1996; 36: 893-906.

18. Anderson TW. An Introduction to multivariate statistical analysis. Wiley-Interscience, John Wiley & Sons, Inc., New Jersey 2003.

19. Alexander DC, Barker GJ, Arridge SR. Detection and modeling of non-Gaussian apparent diffusion coefficient profiles in human brain data. Magn Reson Med 2002; 48: 331-340.

20. Tuch DS, Reese TG, Wiegell MR, Wedeen VJ. Diffusion MRI of complex neural architecture. Neuron 2003; 40: 885-895.

21. Tuch DS, Weisskoff RM, Belliveau JW, Wedeen VJ. High angular resolution diffusion imaging of the human brain. In: Proceedings of the 7th Annual Meeting of the ISMRM, 1999: 321.

22. Tuch DS, Reese TG, Wiegell MR, Makris N, Belliveau JW, Wedeen VJ. High angular resolution diffusion imaging reveals intravoxel white matter fiber heterogeneity. Magn Reson Med 2002; 48: 577-582.

23. Frank LR. Anisotropy in High angular resolution diffusion-weighted MRI. Magn Reson Med 2001; 45: 935-939.

24. Frank LR. Characterization of Aanisotropy in high angular resolution diffusion-weighted MRI. Magn Reson Med 2002: 47: 1083-1099.

25. Özarslan E, Mareci TH. Generalized diffusion tensor imaging and analytical relationships between diffusion tensor imaging and high angular resolution diffusion imaging. Magn Reson Med 2003; 50: 955-965.

26. Minati L, Banasik T, Brzezinski J, Mandelli ML, Bizzi A, Bruzzone MG, Konopka M, Jasinski A. Elevating tensor rank increases anisotropy in brain areas associated with intra-voxel orientational heterogeneity (IVOH): a generalized DTI (GDTI) study. NMR Biomed 2008; 21(1): 2-14.

27. Tuch DS. Diffusion MRI of complex tissue structure. Ph.D. thesis, Division of Health Sciences and Technology, Harvard-MIT, MA 2002.

28. Tuch DS. Q-ball imaging. Magn Reson Med 2004; 52: 1358-1372.

29. Callaghan P. Principles of nuclear magnetic resonance microscopy. Oxford University Press, Oxford, England 1991.

30. Callaghan PT. Rheo-NMR: Nuclear magnetic resonance and rheology of complex fluids. Rep Prog Phys 1999; 62: 599-670.

31. Assaf Y, Cohen Y. Structural information in neuronal tissue as revealed by q-space diffusion NMR spectroscopy of metabolites in bovine optic nerve. NMR Biomed 1999;12: 335-344.

32. Assaf Y, Cohen Y. Assignment of the water slow-diffusion component in the central nervous system using q-space diffusion MRS: Implications for fiber tract imaging. Magn Reson Med 2000; 43: 191-199.

33. King MD, Houseman J, Roussel SA, van Bruggen N, Williams SR, Gadian DG. Q-space imaging of the brain. Magn Reson Med 1994; 32: 707-713.

34. Assaf Y, Ben-Bashat D, Chapman J, Peled S, Bilton IE, Kafri M, Segev Y, Hendler T, Korczyn AD, Graif M, Cohen Y. High b-value q-space analyzed diffusion-weighted MRI: Application to multiple sclerosis. Magn Reson Med 2002; 47: 115-126.

35. Wedeen VJ, Reese TG, Tuch DS, Weigel MR, Dou J–G, Weiskoff RM, Chessler D. Mapping fiber orientation spectra in cerebral white matter with Fourier-transform diffusion MRI. In: Proceedings of the 8th Annual Meeting of the ISMRM 2000: 82.

36. Alexander DC. Multiple-fiber reconstruction algorithms for diffusion MRI. Ann NY Acad Sci 2005; 1064: 113-133.

37. Tournier J-D, Calamante F, Gadian DG, Connelly A. Direct estimation of the fibre orientation density function from diffusion-weighted MRI data using spherical deconvolution. NeuroImage 2004; 23: 1176-1185.

38. Perrin M, Poupon C, Rieul B, Leroux P, Constantinesco A, Mangin, J-F, LeBihan D. Validation of *q*-ball imaging with a diffusion fibre-crossing phantom on a clinical scanner. Phil Trans R Soc B. 2005; 360: 881-891.

39. Campbell JS, Siddiqi K, Rymar VV, Sadikot AF, Pike GB. Flow-based fiber tracking with diffusion tensor and q-ball data: validation and comparison to principal diffusion direction techniques. NeuroImage 2005; 27: 725-736.

40. Khachaturian MH, Wisco JJ, Tuch DS. Boosting the sampling efficiency of Q-Ball imaging using multiple wavevector fusion. Magn Reson Med 2007; 57: 289-296.

41. Hess CP, Mukherjee P, Han ET, Xu D, Vigneron DB. Q-Ball reconstruction of multimodal fiber orientations using the spherical harmonic basis. Magn Reson Med 2006; 56: 104-117.

42. Descoteaux M, Angelino E, Fitzgibbons S, Deriche R. Regularized, fast, and robust analytical Q-Ball imaging. Magn Reson Med 2007; 58: 497-510.

43. Descoteaux M, Angelino E, Fitzgibbons S, Deriche R. Apparent diffusion coefficients from high angular resolution diffusion imaging: Estimation and applications. Magn Reson Med 2006; 56: 395-410.

44. Le Bihan D, Mangin J-F, Poupon C, Clark CA, Pappata S, Molko N, Chabriat H. Diffusion tensor imaging: Concepts and applications. J Magn Reson Imag 2001; 13: 534-546.

45. Basser PJ, Pierpaoli C. Microstructural and physiological features of tissues elucidated by quantitative-diffusion-tensor MRI. J Magn Reson B 1996; 111: 209-219.

46. Basser PJ, Jones DK. Diffusion-tensor MRI: theory, experimental design and data analysis - a technical review. NMR Biomed 2002; 15: 456-467.

47. Mukherjee P. Diffusion tensor imaging and fiber tractography in acute stroke. Neuroimaging Clin N Am 2005; 15: 655-665.

48. Ge Y, Law M, Grossman RI. Applications of diffusion tensor MR imaging in multiple sclerosis. Ann N Y Acad Sci 2005; 1064: 202-219.

49. Wang S, Melhem ER. Amyotrophic lateral sclerosis and primary lateral sclerosis: The role of diffusion tensor imaging and other advanced MR-based techniques as objective upper motor neuron markers. Ann N Y Acad Sci 2005; 1064: 61-77.

50. Song SK, Sun SW, Ramsbottom MJ, Chang C, Russell J, Cross AH. Dysmyelination revealed through MRI as increased radial (but unchanged axial) diffusion of water. NeuroImage 2002; 17: 1429-1436.

51. Alexander AL, Lee JE, Lazar M, Boudos R, Dubray MB, Oakes TR, Miller JN, Lu J, Jeong EK, McMahon WM, Bigler ED, Lainhart JE. Diffusion tensor imaging of the corpus callosum in Autism. NeuroImage 2007; 34(1): 61-73.

52. Song SK, Sun SW, Ramsbottom MJ, Chang C, Russell J, Cross AH. Diffusion tensor imaging detects and differentiates axon and myelin degeneration in mouse optic nerve after retinal ischemia. NeuroImage 2003; 20: 1714 – 1722.

53. Sun SW, Liang HF, Trinkaus K, Cross AH, Armstrong RC, Song SK. Noninvasive detection of cuprizone induced axonal damamge and demyelination in the mouse corpus callosum. Magn Reson Med 2006; 55: 302-308.

54. Kim JH, Budde MD, Liang HF, Klein RS, Russell JH, Cross AH, Song SK. Detecting axon damage in spinal cord from a mouse model of multiple sclerosis. Neurobiol Dis 2006; 21: 626-632.

55. Budde MD, Kim JH, Liang HF, Russell JH, Cross AH, Song SK. Axonal injury detected by in vivo diffusion tensor imaging correlates with neurological disability in a mouse model of multiple sclerosis. NMR Biomed 2008; 21: 589-597.

56. Choi SJ, Lim KO, Monteiro I, Reisberg B. Diffusion tensor imaging of frontal white matter microstructure in early Alzheimer's disease: a preliminary study. J Geriatr Psychiatry Neurol 2005; 18: 12-19.

57. Moeller FG, Hasan KM, Steinberg JL, Kramer LA, Valdes I, Lai LY, Swann AC, Narayana PA. Diffusion tensor imaging eigenvalues: preliminary evidence for altered myelin in cocain dependence. Psychiatry Res 2007; 154(3): 253-258.

58. Concha L, Gross DW, Wheatley BM, Beaulieu C. Diffusion tensor imaging of time-dependent axonal and myelin degradation after corpus callosotomy in epilepsy patients. NeuroImage 2006; 32: 1090-1099.

CHAPTER 2

ADAPTIVE SMOOTHING OF HIGH ANGULAR RESOLUTION DIFFUSION-WEIGHTED IMAGING DATA BY GENERALIZED CROSS-VALIDATION FOR Q-BALL ORIENTATION DISTRIBUTION FUNCTION RECONSTRUCTION[1]

This chapter presents an application of the smoothing splines on the sphere algorithm with GCV smoothing to noisy HARDI data in order to objectively and adaptively smooth the measured diffusivity profiles in three dimensional diffusion space. The resulting smoothed diffusivity profiles are subsequently used to reconstruct fiber ODFs by applying the Funk-Radon transform (FRT). Using GCV leads to a minimization in the ODF radii mean squared error (MSE) estimates but does not always lead to the estimate with the least MSE. ODFs reconstructed from the GCV smoothing splines outperform their analytical QBI counterparts in terms of lower MSE estimates in the ODF radii in all simulations studied. In situations when SNR of the acquired data is very poor, diffusion-weighting low to mid-range with HARDI angular sampling densities typically used today in the clinical setting (diffusion sampling directions around 60

---

[1] Partial work in this chapter has been accepted for publication as "Metwalli NS, Hu XP, Carew JD. Adaptive Smoothing of High Angular Resolution Diffusion-weighted Imaging Data by Generalized Cross-validation Improves Q-Ball Orientation Distribution Function Reconstruction" Magnetic Resonance Imaging, 2010, In Press.

directions), smoothing splines ODFs are more accurate than ODFs from all existing QBI methods.

2.1 Introduction

Diffusion-weighted images are inherently characterized by low signal-to-noise ratios (SNR) as a result of the signal attenuation due to diffusion during image acquisition. With high diffusion-weightings being utilized in HARDI in order to capture complex fiber crossings, raw HARDI data have even lower SNR levels than typically acquired diffusion-weighted data. This issue of noise has been addressed in DTI by a number of investigators with varying approaches. These denoising methods can be categorized as either being frequency domain based or image domain based. Frequency domain based approaches mainly deal with filtering in the wavelet domain (1-3). The image domain based methods included the application of partial differential equation (PDE) based anisotropic diffusion filters to the scalar-valued image (4-6), vector-based PDE anisotropic diffusion filtering applied to the eigenvector fields (7, 8) and applying chains of nonlinear three dimensional Gaussian filters (9). In relation to HARDI data, Papadakis and Smponias (10) proposed using bicubic spherical splines from a piecewise spherical harmonic transform to generate a continuous smooth function from the sampled diffusion-weighted data. The choice of the degree of smoothing was ad hoc. None of the aforementioned methods employs objective and adaptive means of smoothing raw diffusion-weighted data.

HARDI data are samples of an originally smooth diffusion profile in each imaging voxel with an added nuisance noise term. Noise in HARDI data is of concern because it is the raw data that are used to extract the angular structure from the diffusion PDF. Methods used to construct any of the orientational structure functions will be sensitive to and directly affected by this noise. As a result, noisy diffusion data will result in noisy reconstructed ODFs. A usual practice to increase SNR in HARDI acquisitions is to average multiple acquired data sets that may introduce other biasing factors such as bulk motion. A diffusivity profile that is more faithful to the true underlying smooth profile will ultimately result in more accurate ODF reconstruction. Better estimates of the diffusion ODF will be beneficial in fiber-tracking algorithms for extracting more accurate fiber orientations.

Pertaining to Q-Ball Imaging (QBI) (11), low SNR levels of the HARDI data have prompted recent efforts in introducing different forms of regularization to improve ODF reconstruction and reliability of fiber orientation estimation in the spherical harmonic basis approaches to QBI. Specifically, a matrix regularization based on the Tikhonov method was used while solving for the spherical harmonic coefficients when a large harmonic order approximation is desired (12). The regularization parameter is chosen subjectively on the basis of the data SNR. Later, Descoteaux et al. (13) used a regularization term based on the Laplace-Beltrami operator defined on the unit sphere which is more appropriate because it is a measure of smoothness for functions on the unit sphere. The smoothing parameter value was chosen as the one that provided good separation of 1-fiber from 2-fiber distributions over a large range of SNR and *b*-values in

the experimental simulations (14). Even though they state that an optimal regularization parameter could be obtained form the *L*-curve numerical method, they avoid computing it for each HARDI profile at every iteration (13). They show that the Laplace-Beltrami regularization performs better than the Tikhonov regularization. Regularization of the ODF in spherical deconvolution to attenuate spurious noisy peaks in the ODF has also been addressed using a modification on the Tikhonov method (15). No automatic updating of the regularization or smoothing to the data based on underlying data SNR occurs in any of the previously mentioned methods.

In this chapter, an objective and adaptive means of smoothing HARDI data in the three-dimensional diffusion space of each imaging voxel is applied. The smoothing splines on the sphere estimator (16) was used in modeling the noisy HARDI data that naturally reside on the surface of the sphere. This estimator smoothes the measured noisy samples of the diffusion profile directly in three-dimensional diffusion space. This differs from the image domain based denoising methods used previously in denoising DTI data in that the smoothing is done in the diffusion space and not in the two-dimensional image space. The smoothing parameter was chosen objectively by generalized cross-validation (GCV) (17) that, in most situations, minimized the mean squared error (MSE). The MSE is the sum of the square of the bias and the variance of the estimate.

Objectively smoothing the diffusivity profiles is important since noise in the HARDI measurements will propagate through any reconstructed ODF obscuring the orientational structure information extracted from the diffusion PDF. ODF reconstruction

from noisy HARDI data by means of the Funk-Radon transform (FRT) used in the analytical QBI technique (11), in particular, is addressed in this chapter. The ODFs reconstructed after applying the smoothing splines on the sphere method with GCV smoothing were contrasted in terms of performance with the existing QBI methods. The comparisons were carried out for both low-density and high-density HARDI sampling schemes, at different SNR levels and for different fiber crossing angle scenarios.

2.2 Theory

2.2.1 The Smoothing Splines on the Sphere Method

The smoothing splines on the sphere method attempts to model a smooth function residing on a sphere in the presence of random noise. It was proposed to solve a meteorological problem. Atmospheric pressure was measured (with error) at a large number of weather stations distributed around the world. The objective was to estimate a smooth function $u = u(\theta, \phi)$ defined on the surface of earth (θ = latitude, ϕ = longitude). The function specified atmospheric pressure at position (θ, ϕ). The situation is very similar for HARDI data acquisition. The three-dimensional diffusivity profile in each voxel is sampled in three-dimensional diffusion space in a number of specified positions (θ, ϕ) on the sphere in a typical HARDI acquisition. The diffusion-weighted signal intensities at high *b*-value HARDI sampling are marred by noise and therefore can be modeled as follows

$$z_i = u(P_i) + \varepsilon_i , \qquad [2.1]$$

where z_i is the sampled noisy diffusion-weighted data at positions $P_i=(\theta_i,\phi_i)$ and ε_i is assumed to have a zero mean and constant variance, σ^2.

The smoothing splines on the sphere method estimates a smooth function, *u*, on the sphere that minimizes:

$$\frac{1}{n}\sum_{i=1}^{n}(u(P_i)-z_i)^2+\lambda J(u), \qquad [2.2]$$

where *J* is the squared norm of a Laplace-Beltrami operation on the function *u* (16), *n* is the number of sampling directions and λ is a smoothing parameter. The first term in Eq. [2.2] is a goodness-of-fit term while the second penalizes the roughness of *u*. The smoothing parameter controls the tradeoff between the two conflicting goals (16, 17). As the smoothing parameter approaches zero, *u* approaches the minimum norm interpolant whereas when it approaches infinity, *u* approaches a constant function. The smoothing splines solution is given by

$$u(P)=\sum_{i=1}^{n}c_i R(P,P_i)+d, \qquad [2.3]$$

where *P* is the point where one wishes to evaluate the function, P_i are the diffusion encoding directions and $R(P,P_i)$, is a function called the reproducing kernel defined as

$$R(P,P_i)=\frac{1}{2\pi}\left[\frac{1}{2}q_2(x)-\frac{1}{6}\right], \qquad [2.4]$$

where $x=\cos\zeta(P,P_i)$, ζ is the angle between points *P* and P_i,

and

$$q_2(x)=\int_0^1(1-h)^2\left(1-2hz+h^2\right)^{-1/2}dh, \qquad [2.5]$$

where the subscript 2 denotes a second order penalty J in Eq. [2.2]. A closed form solution for Eq. [2.5] was derived elsewhere (16).

The c and d coefficients in Eq. [2.3] are determined by solving the following linear system

$$(\mathbf{R} + n\lambda I)\mathbf{c} + d\boldsymbol{t} = \boldsymbol{z}, \qquad [2.6]$$

with the constraint $\boldsymbol{t}^{\mathbf{T}}\mathbf{c} = 0$, i.e., the coefficients sum to zero, where n is the number of diffusion sampling directions, $\mathbf{R}$ is the n x n symmetric matrix with j, k th entry $R(P_j,P_k)$, $\boldsymbol{t} = (1\ldots1)^{\mathbf{T}}$, and $\boldsymbol{z}$ is the n x 1 column vector of sampled diffusion-weighted data. The $\mathbf{R}$ matrix is formed by evaluating the reproducing kernel for all possible pairs of the diffusion encoding directions.

First, performing a QR decomposition on $\boldsymbol{t}$ and some manipulation leads to (18)

$$\boldsymbol{t} = \mathbf{QK} = (\mathbf{Q}_1 \vdots \mathbf{Q}_2)\begin{pmatrix}\mathbf{K}^* \\ \mathbf{0}\end{pmatrix} = \mathbf{Q}_1\mathbf{K}^*. \qquad [2.7]$$

Premultiplying Eq. [2.6] by $\mathbf{Q_2}^{\mathbf{T}}$ we get

$$\mathbf{Q}_2^{\mathbf{T}}\left[(\mathbf{R} + n\lambda I)\mathbf{c}\right] + d\mathbf{Q}_2^{\mathbf{T}}\boldsymbol{t} = \mathbf{Q}_2^{\mathbf{T}}\boldsymbol{z}\ .$$

From $\boldsymbol{t}^{\mathbf{T}}\mathbf{c} = 0$, we have $\mathbf{Q_1}^{\mathbf{T}}\mathbf{c} = 0$ and $\mathbf{c} = \mathbf{Q_2}\mathbf{Q_2}^{\mathbf{T}}\mathbf{c}$ and noting that $\mathbf{Q_2}^{\mathbf{T}}\boldsymbol{t} = 0$, leads to the equation for $\mathbf{c}$

$$(\mathbf{Q}_2^{\mathbf{T}}\mathbf{R}\mathbf{Q}_2 + n\lambda I)\mathbf{Q}_2^{\mathbf{T}}\mathbf{c} = \mathbf{Q}_2^{\mathbf{T}}\boldsymbol{z},$$

$$\mathbf{Q}_2^{\mathbf{T}}\mathbf{c} = (\mathbf{Q}_2^{\mathbf{T}}\mathbf{R}\mathbf{Q}_2 + n\lambda I)^{-1}\mathbf{Q}_2^{\mathbf{T}}\boldsymbol{z},$$

$$\mathbf{c} = \mathbf{Q}_2(\mathbf{Q}_2^{\mathbf{T}}\mathbf{R}\ \mathbf{Q}_2 + n\lambda I)^{-1}\mathbf{Q}_2^{\mathbf{T}}\boldsymbol{z} \qquad [2.8]$$

Then premultiplying Eq. [2.6] by $\mathbf{Q_1}^{\mathbf{T}}$ we get

$$\mathbf{Q}_1^{\mathrm{T}}\mathbf{R}\mathbf{c} + n\lambda I\mathbf{Q}_1^{\mathrm{T}}\mathbf{c} + \mathbf{Q}_1^{\mathrm{T}} d\mathbf{Q}_1\mathbf{K}^* = \mathbf{Q}_1^{\mathrm{T}}\mathbf{z}.$$

With $\mathbf{Q_1}^{\mathrm{T}}\mathbf{c} = 0$ and some derivation we get an expression for *d*

$$d\mathbf{Q}_1^{\mathrm{T}}\mathbf{Q}_1\mathbf{K}^* = \mathbf{Q}_1^{\mathrm{T}}\mathbf{z} - \mathbf{Q}_1^{\mathrm{T}}\mathbf{R}\mathbf{c},$$

$$d = (\mathbf{K}^*)^{-1}\left(\mathbf{Q}_1^{\mathrm{T}}\mathbf{z} - \mathbf{Q}_1^{\mathrm{T}}\mathbf{R}\ \mathbf{c}\right) \qquad [2.9]$$

By evaluating **c** and *d* from Eqs. [2.8] and [2.9], the value of the smoothing splines on the sphere function, $u(P)$, can be estimated using Eq. [2.3] anywhere in three-dimensional space using the coordinates of *P* to evaluate the reproducing kernel n times for all the pairs of points *(P,P$_i$)*.

For subsequent ODF reconstruction, the new sets of points are the coordinates of the equator points for each of the ODF reconstruction directions. The diffusion-weighted signals are estimated at the equator points for each ODF reconstruction direction, and as per the FRT, are summed to calculate the ODF radius along each reconstruction direction. The entire algorithm is outlined further in Table 2-1.

2.2.2 Choice of the Smoothing Parameter

GCV is an objective method for automatically setting the amount of smoothing, λ. The GCV estimate of λ, $\hat{\lambda}$, minimizes the GCV criterion

$$\frac{1}{n}\frac{\sum_{i=1}^{n}\left(z_i - u(P_i)\right)^2}{\left(1 - n^{-1}tr\mathbf{A}(\lambda)\right)^2} \qquad [2.10]$$

where $\mathbf{A}(\lambda)$ is the n x n matrix satisfying $\left(u(P_1),\ldots,u(P_n)\right)^{\mathrm{T}} = \mathbf{A}(\lambda)\mathbf{z}$, that maps the data to their fitted values (17-19). The numerator of the GCV function measures the closeness

of the function to the data, while the denominator is related to the complexity of the model. Minimizing the GCV function can be seen as a tradeoff between fitting the observed data well and model complexity.

The smoothing splines on the sphere method has been applied recently (20) in order to smooth out spikes in the noisy MR measurements with application to the spherical deconvolution method for ODF extraction. However, the investigators did not evaluate the choice of the smoothing parameter. Kaden et al. (21) then later used smoothing spline modeling differently for fiber orientation density estimation with a non-objective means of choosing the smoothing parameter on a per voxel basis.

GCV has been used recently in selecting the regularization parameter in calculating the regularized FOD using damped singular value decomposition (DSVD) in a modification on the spherical deconvolution method termed DSVD-GCV (22) and in the estimation of QBI ODFs reconstructed in the spherical harmonic basis on 3T and 7T human brain data (23). It is important to note that this differs from our work in that DSVD-GCV is applied in reconstructing the QBI ODFs in the spherical harmonic basis with GCV used in selecting the regularization parameter. We estimate a smoothing splines on the sphere function for the diffusivity profile with the degree of smoothing chosen by GCV. This diffusivity profile estimate is subsequently used in reconstructing the ODF.

Table 2-1: Smoothing splines on the sphere estimation and orientation distribution function (ODF) reconstruction algorithms

n : Number of diffusion encoding sampling directions

m : Number of desired ODF reconstruction directions

k : Number of equator points around each ODF reconstruction direction

Input

S	n x 3 matrix of diffusion gradient sampling orientations
U	m x 3 matrix of desired ODF reconstruction points on the unit sphere
z	n x 1 column vector of sampled diffusion-weighted data

Output

u	n x 1 column vector of smoothed diffusion-weighted data (smoothing spline on the sphere estimate)
o	m x 1 column vector of estimated ODF radii at reconstruction locations in U

Intermediaries

R	n x n estimation reproducing kernel
t	n x 1 unity column vector
A(λ)	n x n 'hat' matrix that maps the data to their fitted values
λ	Smoothing parameter
c, *d*	Smoothing spline on the sphere function coefficients
I	(m x k) x n interpolation reproducing kernel
w	(m x k) x 1 column vector of diffusion-weighted signals at the equator points
P	m x (m x k) Kronecker tensor product matrix

Algorithm

To get *u*:

Construct the n x n estimation reproducing kernel matrix **R** using Eqs. (5-6).

Form the linear system $(\mathbf{R} + n\lambda I)\mathbf{c} + d\boldsymbol{t} = z$, with constraint $\boldsymbol{t}^{\mathrm{T}}\mathbf{c} = 0$ and I an n x n identity matrix.

Perform a QR decomposition on $\boldsymbol{t}$ to get $\boldsymbol{t} = \mathbf{QK} = (\mathbf{Q}_1 \vdots \mathbf{Q}_2)\begin{pmatrix}\mathbf{K}^* \\ \mathbf{0}\end{pmatrix} = \mathbf{Q}_1\mathbf{K}^*$.

Construct the $\mathbf{A}(\lambda)$ matrix in Eq. (11) as $\mathbf{A}(\lambda) = I_{nxn} - n\lambda\mathbf{Q}_2\left(\mathbf{Q}_2^{\mathrm{T}}\mathbf{R}\mathbf{Q}_2 + n\lambda I\right)^{-1}\mathbf{Q}_2^{\mathrm{T}}$.

Estimate λ that minimizes the generalized cross-validation (GCV) criterion (Eq. (11)).

Estimate **c** and *d* from Eqs. (9-10).

Estimate the smoothing spline on the sphere with GCV smoothing, ***u***, from ***u* = Rc + *d*,** Eq. (4).

To get *o*:

Construct the (m x k) x n interpolation reproducing kernel matrix **I** using Eqs. (5-6).

Estimate the (m x k) x 1 column vector of diffusion-weighted signals at the equator points, ***w***, for every ODF reconstruction direction m_i using ***w* = Ic + *d*.**

Compute the sum of the diffusion-weighted signals at the equator points for each ODF reconstruction direction m_i by pre-multiplying ***w*** with an m x (m x k) Kronecker tensor product matrix, **P**, of an m x m identity matrix and a 1 x k unity row vector to get the m x 1 column vector of estimated ODF radii, ***o***.

***o* = P*w*,** where $\mathbf{P} = \begin{pmatrix} [1\ldots1]_{1xk} & & \mathbf{0} \\ & [1\ldots1]_{1xk} & \\ \mathbf{0} & & [1\ldots1]_{1xk} \end{pmatrix}_{m\ x\ (mxk)}$.

2.3 Methods

Monte Carlo noise simulations were performed to quantify the benefit gained from using smoothing splines on the sphere with GCV smoothing on noisy HARDI data. Ground truth ODFs were calculated from the noise-free data and diffusion-weightings simulated by the two tensor mixture model. The MSE estimates of the ODFs from the new method were compared to existing QBI methods including the standard analytical QBI algorithm in addition to the spherical harmonic expansion QBI methods as they relate to the ground truth ODFs. As previously mentioned, the MSE is computed by the summation of the square of the averaged bias in the reconstructed ODF radius in each sampling direction and the averaged variance estimated in each direction over all noise trials. All methods were contrasted in terms of fiber crossing angle extraction accuracy at different SNR levels.

In vivo human brain data were acquired to validate our approach for ODF reconstruction and contrast their ODFs to the ODFs reconstructed using the standard analytical QBI algorithm.

2.3.1 Simulated Data

Two fiber populations in slow Gaussian exchange were simulated (24, 25) over a range of crossing angles from 60° to 90° in 5° increments. The tensors were assigned fractional anisotropy (FA) (26) and trace values of 0.7 and 2.1 x 10^{-3} mm^2/s, respectively. The tensor components were estimated from these parameters and the noise-free diffusion-weighted signals were calculated. Both tensors were simulated as occupying

equal partial volume fractions (12, 27). The diffusion-weighted data were sampled along 60 directions and along 252 directions from a three-fold tessellation of the icosahedron. The sampling direction sets were normalized to the unit sphere. The HARDI data were simulated at two *b*-weightings, b = 2000 s/mm^2 and b = 4000 s/mm^2. Rician noise (Gaussian noise in quadrature) was added to the noise-free data (28) to achieve SNR values of 10, 20, 35 and 50 in the signal with no diffusion weighting. SNR was defined as the ratio of the signal intensity in the signal with no diffusion weighting to the standard deviation σ of the complex Gaussian noise added. The noise simulations were conducted over 250 noise trials. The choice of the simulation parameters was based on a number of prior studies (11, 25, 27, 29, 12, 30, 31).

2.3.2 Orientation Distribution Function (ODF) Reconstruction

First, ODFs were reconstructed from the noisy data using spherical radial basis functions (sRBFs) as in the standard analytical QBI algorithm (11). The interpolation kernel width, σ_i, used was the minimizer of the log condition number of the sRBF interpolation matrix (11). The smoothing kernel width was set to 2° for the simulated data sampled at 60 directions with the lowest SNR, SNR = 10, whereas for higher SNR levels no smoothing kernel was applied. A smoothing kernel width of 3° was needed for the data sampled with 252 directions at all SNR levels. These widths were chosen to be the degree that achieved the least MSE estimates in the ODFs.

Secondly, ODFs were reconstructed following the spherical harmonic basis QBI techniques (12, 13). Specifically, for the spherical harmonic QBI technique with

Tikhonov regularization, a regularization parameter $\lambda = 2$ was used as per the investigators (12). For the spherical harmonic QBI approach with Laplace-Beltrami regularization, the authors recommended using a regularization parameter $\lambda = 0.006$ as at this value a good separation of single and two fiber distributions over a large range of SNR and diffusion-weightings is achieved (13). Spherical harmonic expansions up to order $l = 8$ were estimated in the two aforementioned techniques.

In attempts to eliminate subjective intervention in the spherical harmonic QBI approach with Laplace-Beltrami regularization whether in the choice of the regularization parameter value or the order of the harmonic expansion, two separate simulation studies were performed incorporating GCV. First, the regularization parameter value was chosen as the minimizer of a GCV criterion and in the second simulation study GCV was used to determine the harmonic order of the QBI spherical harmonic expansion.

Lastly, prior to ODF reconstruction, the smoothing splines on the sphere function with GCV smoothing parameter was estimated from the data in each noise trial. The original gradient sampling directions used to calculate the diffusion-weighted signals were used in the estimation of the smoothing splines on the sphere function. The order of the penalty in the estimation of the smoothing splines on the sphere function was varied from 2 through 10 to determine which degree gave the best reconstructed ODF in terms of MSE. The choice was with a second order penalty that in turn resulted in a cubic smoothing splines on the sphere function. The searching grid for the smoothing parameter spanned, $\lambda \in \left[10^{-8}, 10^{2}\right]$ on a log scale with step size of 0.1 to identify the

lambda that gave the minimum GCV criterion score over that range. This range was determined empirically according to the set simulation parameters as being the range where a minimum in the GCV score was typically found.

Subsequently, the FRT was applied to reconstruct the ODFs. Basically it is the integral of the diffusion-weighted signal intensities specified on the equatorial line in the plane perpendicular to each reconstruction direction. Diffusion-weighted data were estimated at 48 evenly spaced points across each equator plane (11). For the smoothing splines on the sphere method, the smooth function estimate is defined everywhere on the sphere. One needs to only specify the spherical coordinates of the equator points to estimate the diffusion signals there. The same number of equator points, 48, was used and the signals were summed along each equator to estimate the ODF radii in the reconstruction directions. ODFs from QBI and splines on the sphere modeling were reconstructed at 252 and 642 icosahedral directions for the 60 and 252 simulated sampling schemes, respectively.

MSE estimates of the ODF radii from all methods were compared with the calculated ground truth ODFs. Ground truth ODFs were reconstructed along the 252 and 642 sampling directions used to reconstruct the ODFs in the noise trials. Using the FRT, the ground truth ODF radii were reconstructed by summing the diffusion-weighted data along the equator perpendicular to each reconstruction direction. However, 480 equator points were used to obtain a more accurate calculation of the ODF radius along each reconstruction direction. Following the general assumption that the fiber directions are

determined by the local maxima of the ODFs, the fiber crossing angle estimates were extracted from all noise trials and estimated averages for all crossing angle cases studied were obtained.

2.3.3 *In Vivo* Human Brain Data

Two normal healthy volunteers (29 and 31 years of age) were recruited and informed consent was obtained prior to the experiment according to the guidelines set by Emory University's Institutional Review Board (IRB). HARDI data were acquired on a Siemens 3T Tim® whole body scanner (Siemens Medical Solutions, Erlangen, Germany) using a diffusion-weighted single-shot echo planar imaging (EPI) sequence. The imaging pulse sequence was a standard sequence used regularly for clinical studies and was approved by the IRB.

For the first volunteer, HARDI data were acquired using a 12 channel volume coil along 256 directions uniformly distributed on the northern hemisphere of the sphere. The diffusion-weighting used was *b*-value = 4000 s/mm^2 and imaging parameters: repetition time / echo time (TR/TE) = 3000/129ms, number of acquisitions = 1, field-of-view (FOV) = 200 mm x 200 mm, matrix size of 96 x 96, resolution of 2.1 x 2.1 mm^2, 5 mm slice thickness with parallel imaging (GRAPPA) acceleration factor of 2. The second volunteer was subsequently scanned with the same sequence using 60 directions. The diffusion-weighting used was *b*-value = 2000 s/mm^2 and imaging parameters: TR/TE = 9000/102ms, number of acquisitions = 1, FOV = 256 mm x 184 mm, matrix size of 128 x 92, resolution of 2 x 2 mm^2, 2 mm slice thickness with parallel imaging (GRAPPA)

acceleration factor of 2. T1-weighted MPRAGE scans of the entire head were also obtained at 1 x 1 x 1 mm^3 resolution for anatomical referencing of both volunteers. Acquisition time for the 60 direction diffusion scan was around 15 minutes while the 256 direction scan took 45 minutes. The T1-weighted scans took 6 minutes. For both QBI and for smoothing splines on the sphere, the ODFs were reconstructed at 252 and 642 directions from the tessellated icosahedron for the 60 and 256 sampling direction datasets, respectively. The 256 sampling directions were mirrored into the southern hemisphere to obtain uniform coverage across the entire sphere.

ODFs reconstructed using the standard QBI algorithm utilized widths for the interpolation and smoothing kernels of 10° and 20°, respectively, for the 60 direction dataset and 12° and 3° for the 256 direction dataset. The widths for the interpolation kernels were the minimizers of the log condition number of the interpolation matrices in each case. The smoothing kernel widths were varied to the value that gave the best-looking ODFs visually. The regularization parameters in the spherical harmonic QBI approaches were set at $\lambda = 2$ and $\lambda = 0.006$ for spherical harmonic QBI with Tikhonov regulariazation and spherical harmonic QBI with Laplace-Beltrami regularization, respectively. For visualization purposes, all ODFs were minmax normalized as in (11).

A flowchart depicting the processing pipelines done in this work on both the simulated and *in vivo* data is shown in Figure 2.1. All the simulations were performed in MATLAB® (The Mathworks Inc., Natick, MA) along with all the QBI and smoothing splines on the sphere estimation with GCV selected smoothing analysis and visualization for both the simulated and *in vivo* data. The smoothing splines estimates were verified

using Xianhong Xie's splines on the sphere package and library, 'sspline', in **R** (**R** Foundation for Statistical Computing, Vienna, Austria).

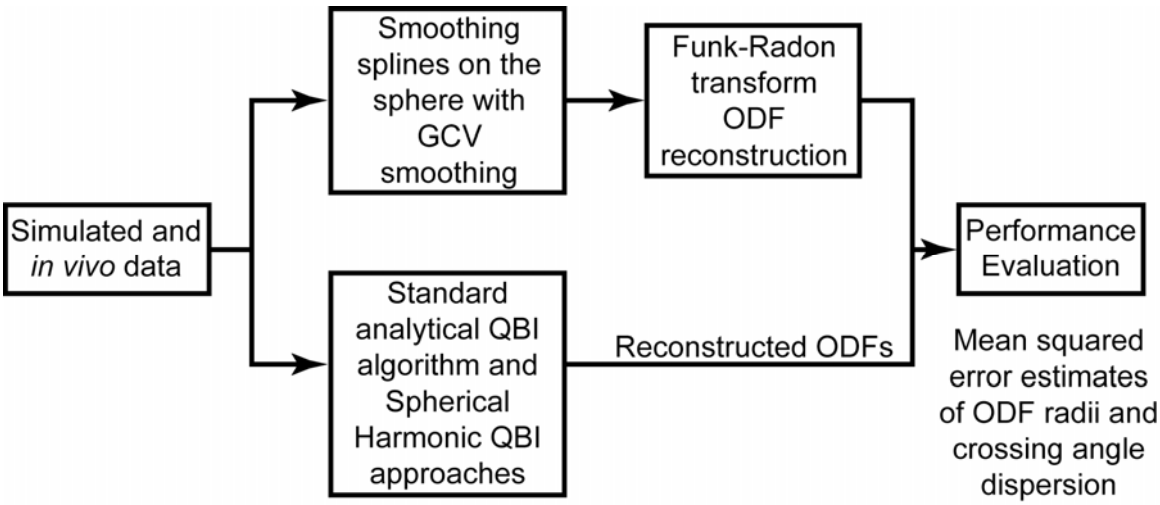

Figure 2.1 Flowchart showing the processing pipelines for the smoothing splines on the sphere method with generalized cross-validation (GCV) smoothing and existing QBI algorithms for reconstructing ODFs from simulated and in vivo human brain data.

2.4 Results

2.4.1 Simulated Data

2.4.1.1 Degree of smoothing adapts to the data signal-to-noise ratio (SNR)

The use of GCV in choosing the smoothing parameter in the smoothing splines on the sphere estimation problem offers an objective means of smoothing the noisy diffusivity profiles measured with high *b*-value HARDI scans. Figure 2.2 shows smoothing splines on the sphere reconstructed ODFs with three different smoothing parameter values utilized for a noisy 90° fiber crossing case at SNR = 20 and diffusion-

weighting of 4000 s/mm^2. With the smoothing parameter value that minimizes the GCV score, the reconstructed ODF is smoothed out to resemble to a great extent the ground truth ODF. Whereas when the smoothing is less than that selected by minimization of GCV, it leads to an under-smoothed ODF with residual noise. And at higher smoothing levels, the ODF is over-smoothed leading to an increased fusing of the ODF peaks.

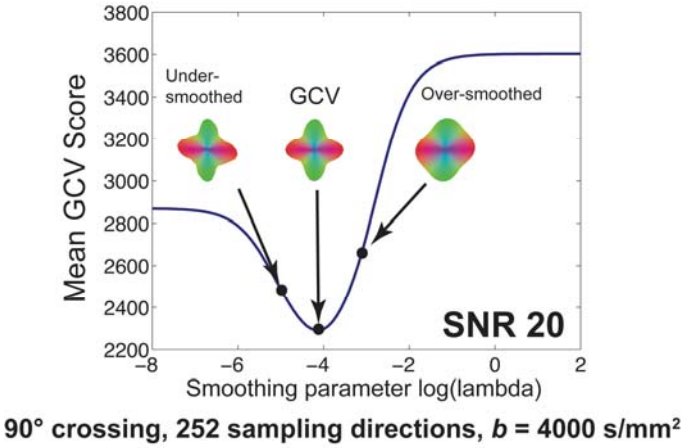

Figure 2.2 Generalized cross-validation (GCV) is an objective means of choosing the smoothing parameter. The displayed ODFs with their respective smoothing parameter values set as shown on the mean GCV score curve represent, from left to right, under-smoothed, GCV-selected smoothing, and over-smoothed ODFs. Note how the under-smoothed ODF still shows evidence of noise persisting in the data while the over-smoothed ODF shows a slight fusion between the ODF's dominant peaks.

Figure 2.3 displays plots of the mean GCV scores, blue lines, versus the logarithm of the smoothing parameter with the red lines being ± one standard deviation of the GCV scores at various SNR levels. Figure 2.3(a) shows the mean GCV score plots for a 90° crossing scenario sampled with 60 diffusion-gradient directions and *b*-value = 2000 s/mm^2 at SNR levels 10 and 20. Figure 2.3(b) displays the GCV scores for a 60° crossing case at the higher diffusion-weighting of b = 4000 s/mm^2 at SNR levels 20, 35, and 50.

The latter case was sampled with 252 sampling directions. As can be seen in Figures 2.3(a) and 2.3(b), the degree of smoothing increases as the SNR decreases and this is automatic via GCV without external intervention. In Figures 2.3(a) and 2.3(b) at the highest SNR levels tested, SNR = 20 and SNR = 50, respectively, the GCV chosen smoothing values are smaller, i.e. more negative logarithm of smoothing, than the values at lower SNR levels, highlighted by the dashed gray lines extending from the plots with lower SNR levels. An attribute worthy of mentioning is that the variability in the GCV scores decreases as the SNR increases.

2.4.1.2 Smoothing parameter chosen via generalized cross-validation (GCV) minimizes the mean squared error (MSE) of the estimated spline

The choice of the smoothing parameter value that minimizes the GCV scores in the smoothing splines on the sphere estimation problem minimizes the MSE of the estimate. This smoothing parameter value that minimizes the GCV score coincides with the value that when used in the smoothing splines on the sphere estimation problem would lead to a spline estimate with the minimum MSE. In a few cases when the SNR is too low (SNR $\leq$ 10) or is very high (SNR $\geq$ 50), the smoothing parameter that minimizes the GCV score does not lead to the estimate with the least MSE but does still lead to a minimization in the MSE overall. These cases are exemplified in Figure 2.4 for a 90° crossing sampled with 60 directions at b = 2000 s/mm^2 and SNR = 10. In this case the smoothing parameter chosen by GCV would lead to a slightly under-smoothed estimate than is required. GCV is an objective way of choosing the smoothing parameter but Figure 2.4 seems to suggest it may not be the optimal means for all sampling and SNR

combinations. GCV leads to a minimization of the MSE of the estimate but in some cases does not lead to the estimate with the least MSE.

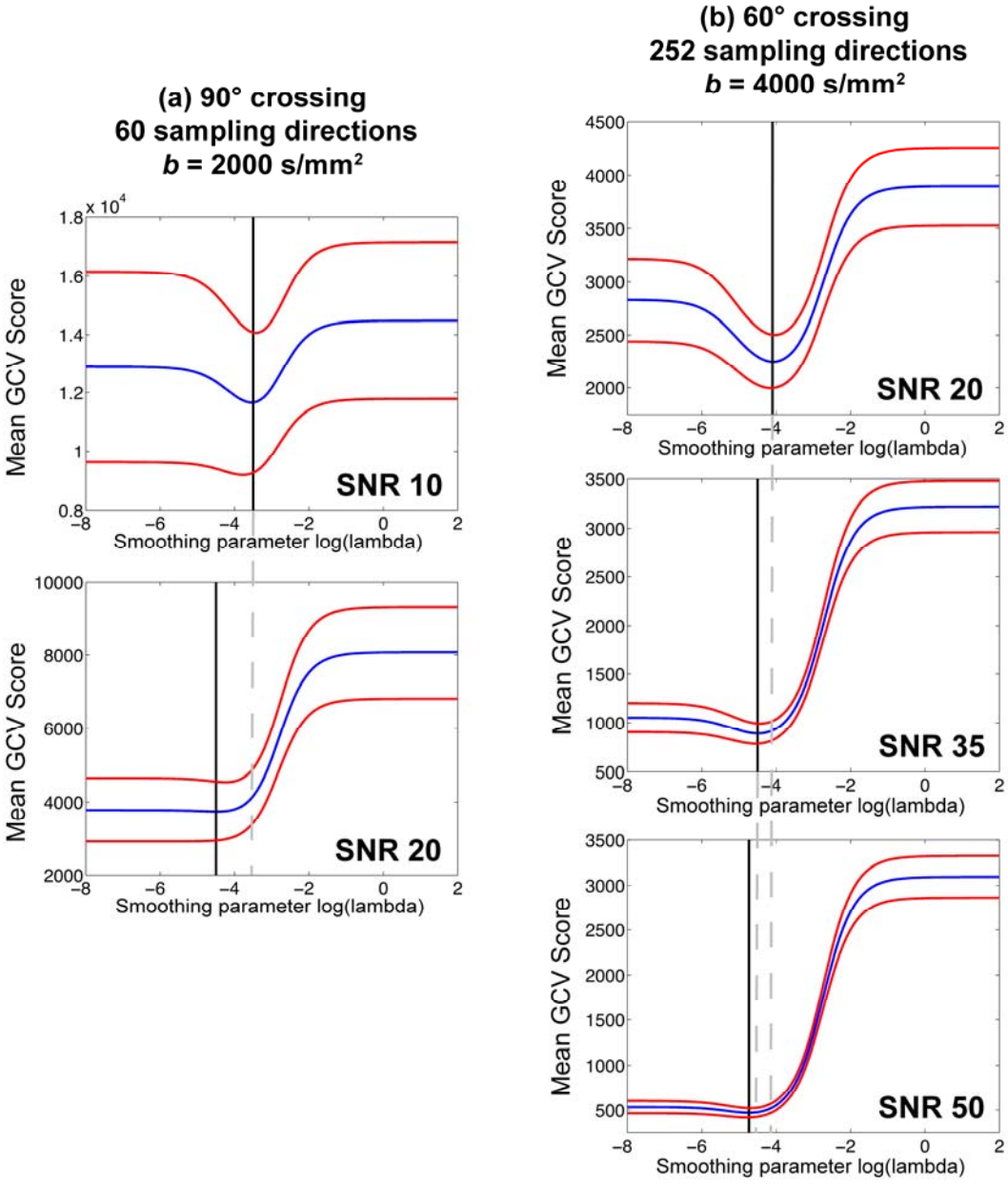

Figure 2.3 Use of generalized cross-validation (GCV) leads to adaptive smoothing of the noisy diffusion data concurrent with the data's signal-to-noise ratio (SNR). As the SNR decreases, more smoothing of the raw data is required and vice versa and GCV accomplishes that without external intervention. Figure 2.3(a) displays the mean GCV score plots for a 90° crossing sampled with 60 diffusion-gradient directions and b-value = 2000 s/mm^2 for SNR = 10 and SNR = 20. Figure 2.3(b) shows the GCV scores for a 60° crossing sampled with 252 sampling directions at b = 4000 s/mm^2 and SNR levels 20, 35 and 50.

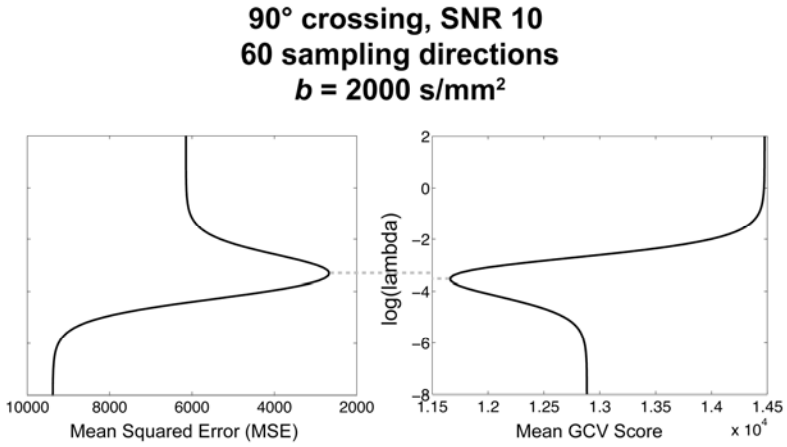

Figure 2.4 Generalized cross-validation (GCV) leads to a minimization of the mean squared error (MSE) of the smoothing spline estimate but in some cases does not lead to the estimate with the least MSE. Among the cases where GCV does not lead to the estimate with the least MSE is a 90° fiber crossing scenario sampled with 60 directions, SNR = 10 and b = 2000 s/mm^2. The left panel shows the smoothing parameter value at which the MSE is minimized is slightly higher than the value determined by minimizing the GCV score. The data in this case would be slightly under-smoothed.

2.4.1.3 Orientation distribution function (ODF) reconstruction comparisons

The ODFs reconstructed from the smoothing splines on the sphere outperform their counterparts reconstructed using the standard analytical QBI algorithm in terms of exhibiting an overall decreased MSE estimate in the ODF radii. This is evident across all tested SNR levels in the 60 and 252 sampling direction schemes and all crossing angle scenarios studied. Figure 2.5(a) shows plots of averaged MSE estimates in the ODF radii, averaged over all reconstruction directions, with ± one standard deviation for a 90° fiber crossing situation at b = 2000 s/mm^2 and at SNR levels 10, 20 and 35 for smoothing splines on the sphere ODFs, blue bars, and the analytical QBI ODFs, red bars. Figure 2.5(b) show plots of the averaged MSE estimates in ODF radii for 60° and 90° fiber crossing angles at SNR levels 20, 35, and 50 and b = 4000 s/mm^2. Again the MSE estimates for the smoothing splines on the sphere ODFs are the blue bars and the

analytical QBI ODFs are in red. There is marked improvement in ODF estimation and reconstruction as the SNR levels increase and as the crossing fiber angle separation increases. Variability in the MSE estimates of the smoothing splines ODFs decreases as the SNR level increases. This is most marked in Figure 2.5(a) for a 90° fiber crossing angle case sampled at 60 directions with $b = 2000$ s/mm^2 with SNR increased from 10 to 35. There is increasing variability in the MSE estimates of the ODF radii for both smoothing splines ODFs and analytical QBI ODFs as the diffusion-weighting increases, Figure 2.5(b), although the variability is higher for the smoothing splines ODFs.

In any smoothing procedure, bias is introduced in the estimate in order to reduce the variance in hopes of reducing the overall MSE. And despite increases in bias variability in the smoothing splines estimate, the substantial reduction in the variance seen when using smoothing splines for ODF reconstruction leads to the overall decrease in the MSE estimates of the ODF radii compared to the analytical QBI ODF MSE estimates, Figure 2.6. The increase in variability seen in the smoothing splines ODF MSE estimates is attributable to the increase in bias variability of the smoothing spline estimates.

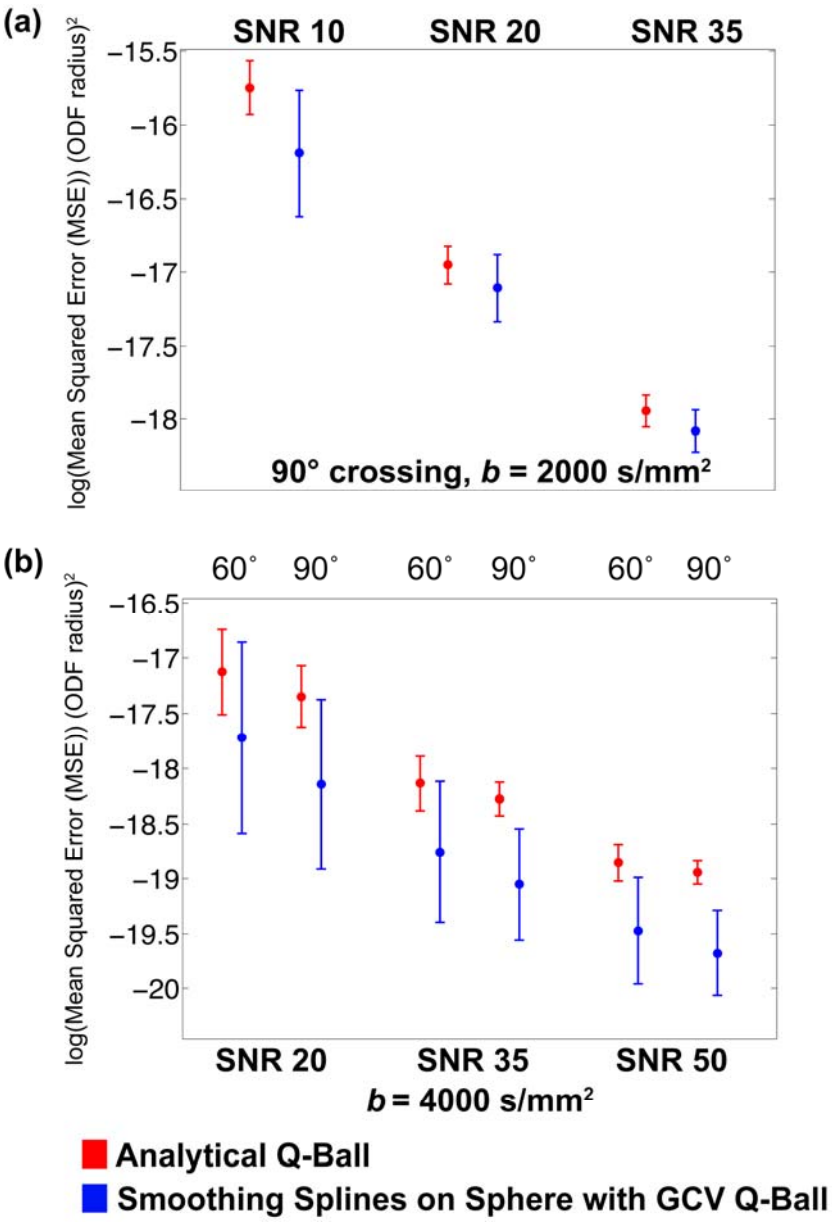

Figure 2.5 Orientation distribution functions (ODFs) reconstructed from the smoothing splines on the sphere exhibit an overall decreased mean squared error (MSE) estimate in the ODF radii compared to their counterparts reconstructed using the standard analytical QBI algorithm. Figure 2.5(a) displays plots of averaged MSE estimates in the ODF radii with ± one standard deviation for a 90° fiber crossing situation at b = 2000 s/mm^2 and at SNR levels 10, 20 and 35 for smoothing splines on the sphere ODFs, blue bars, and the analytical QBI ODFs, red bars. Figure 2.5(b) show plots of the averaged MSE estimates in ODF radii for 60° and 90° fiber crossing angles at SNR levels 20, 35, and 50 and b = 4000 s/mm^2.

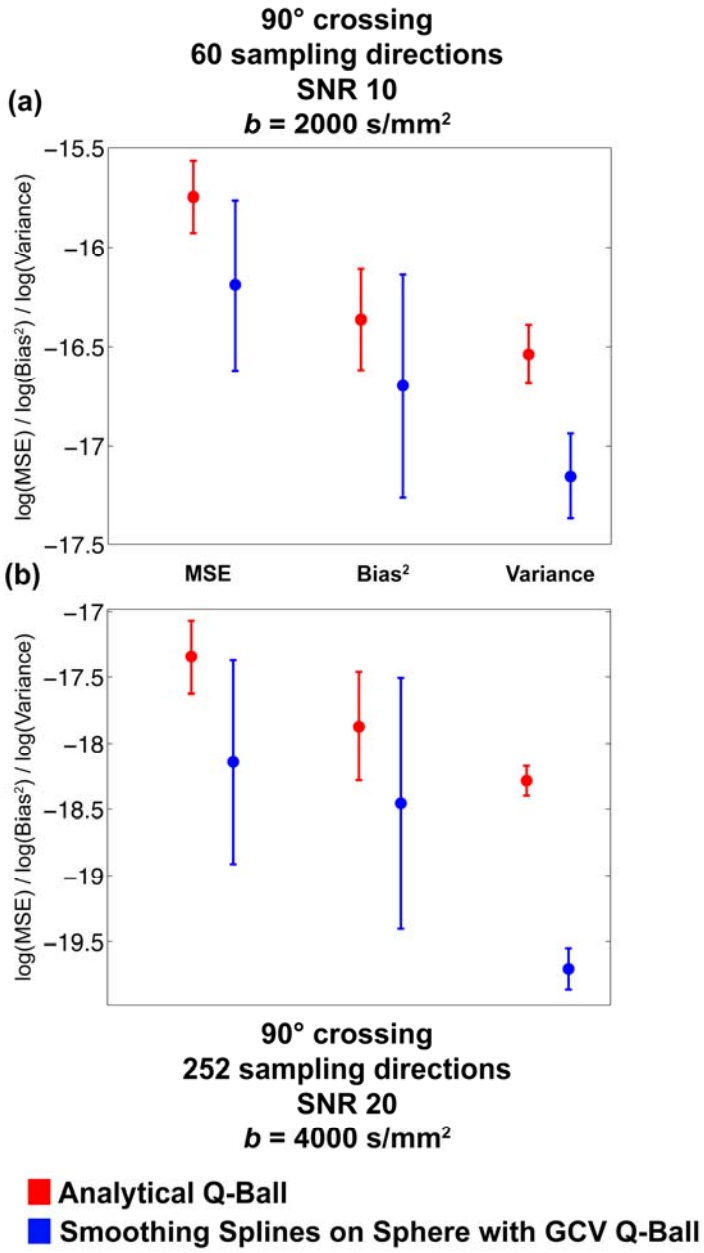

Figure 2.6 Any smoothing procedure introduces bias in order to reduce the variance in hopes of reducing the mean squared error (MSE) in the estimate. The increase in bias variability is the main contributor to the increase in variability seen in the smoothing spline orientation distribution function (ODF) MSE estimates. MSE, the square of the bias, and variance estimates in the ODFs from QBI and from smoothing splines on the sphere are shown for 90° crossing cases sampled with 60 directions, at SNR = 10 and b = 2000 s/mm^2, Figure 2.6(a), and sampled with 252 directions, at SNR = 20 and b = 4000 s/mm^2, Figure 2.6(b). The variance in the smoothing spline ODFs is substantially decreased leading to the overall decrease in the MSE estimates in the ODF radii.

In comparison with the spherical harmonic approaches to QBI, the smoothing splines on the sphere ODFs performance varies according to the HARDI data angular sampling density, diffusion-weighting applied, and data SNR. In the case of spherical harmonic QBI with Tikhonov regularization (regularization parameter $\lambda = 2$), the smoothing splines ODFs perform better, in terms of MSE, than the spherical harmonic ODFs of order 4, 6, and 8 at the low density sampling scheme of 60 directions with diffusion-weighting 2000 s/mm^2 and at the low SNR levels of SNR = 10 and SNR = 20, Figure 2.7(a). At higher SNR; SNR = 35, the smoothing splines ODF MSE estimates are only lower than the spherical harmonic ODFs of order 6 and 8. However, all spherical harmonic QBI ODFs with Tikhonov regularization outperform the smoothing splines on the sphere ODFs, in terms of MSE, in the high density sampling scheme (252 sampling directions) across all simulated crossing angle scenarios and SNR levels tested. This is exemplified in Figure 2.7(b) and 2.7(c) with a 60° fiber crossing case with $b = 4000$ s/mm^2 at SNR = 20 and SNR = 35 and a 90° crossing case at the same b-weighting and SNR levels, respectively.

In relation to the spherical harmonic approach with Laplace-Beltrami regularization (regularization parameter $\lambda = 0.006$), smoothing splines on the sphere ODFs only slightly outperform their spherical harmonic QBI counterparts of order 6 and 8, in terms of MSE, at the low density sampling scheme of 60 directions with diffusion-weighting 2000 s/mm^2 and SNR level of SNR = 10, Figure 2.8(a). In all other simulated cases, at low and high density HARDI sampling and at all SNR levels simulated, the

spherical harmonic QBI ODFs with Laplace-Beltrami regularization outperform the smoothing splines ODFs in terms of lower MSE, Figure 2.8(b) and 2.8(c).

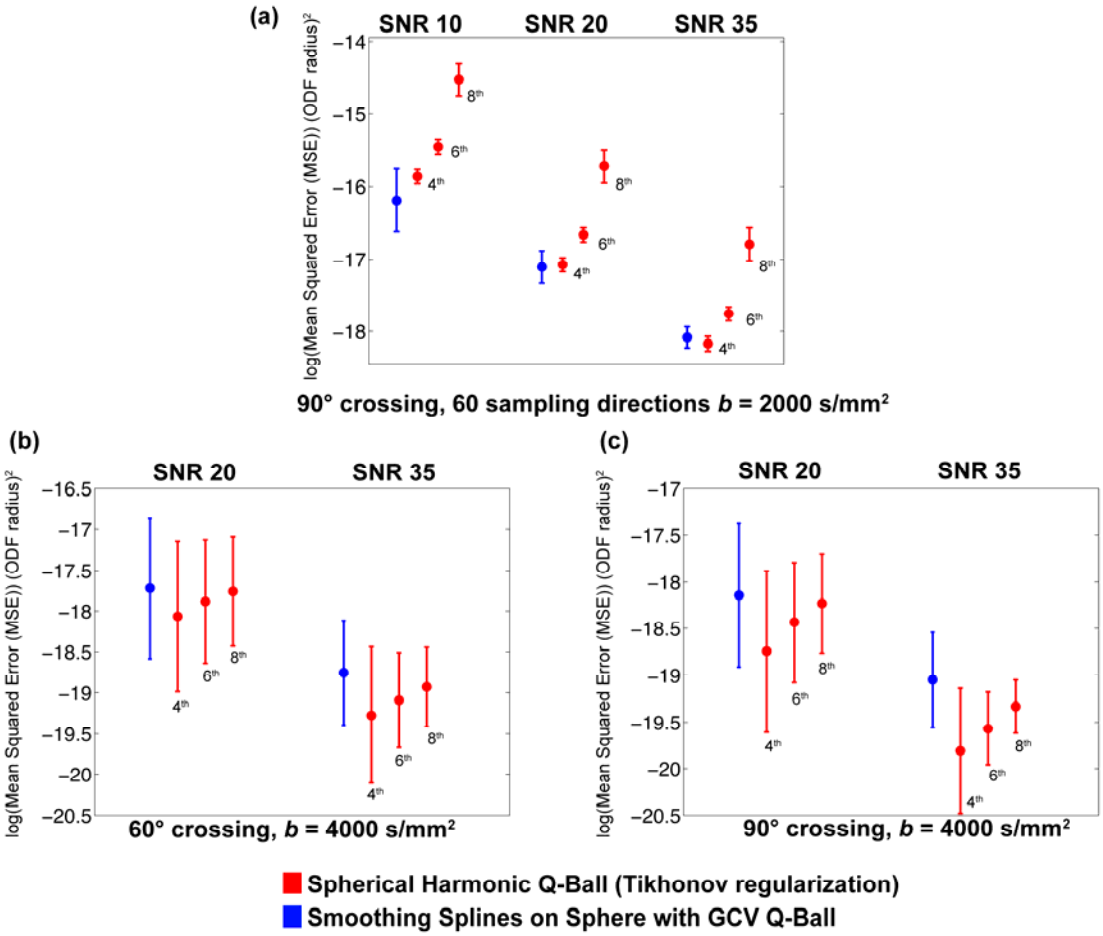

Figure 2.7 Orientation distribution functions (ODFs) reconstructed using smoothing splines on the sphere generally exhibit an overall decreased mean squared error (MSE) estimate in the ODF radii compared to their counterparts reconstructed from spherical harmonic QBI with Tikhonov regularization in the low density sampling scheme of 60 diffusion sampling directions with b = 2000 s/mm^2. The smoothing splines ODFs (in blue) outperform, in terms of MSE, the spherical harmonic ODFs (in red) of order 4, 6, and 8 at 60 directions with diffusion-weighting 2000 s/mm^2 and at the low SNR levels of SNR = 10 and SNR = 20, Figure 2.7(a). However at higher SNR; SNR = 35, the smoothing splines ODF MSE estimates are only lower than the spherical harmonic ODFs of order 6 and 8. All spherical harmonic QBI ODFs with Tikhonov regularization outperform their smoothing splines on the sphere ODFs, in terms of MSE, in the high density sampling scheme (252 sampling directions) across all simulated crossing angle scenarios and SNR levels tested, Figure 2.7(b) and 2.7(c).

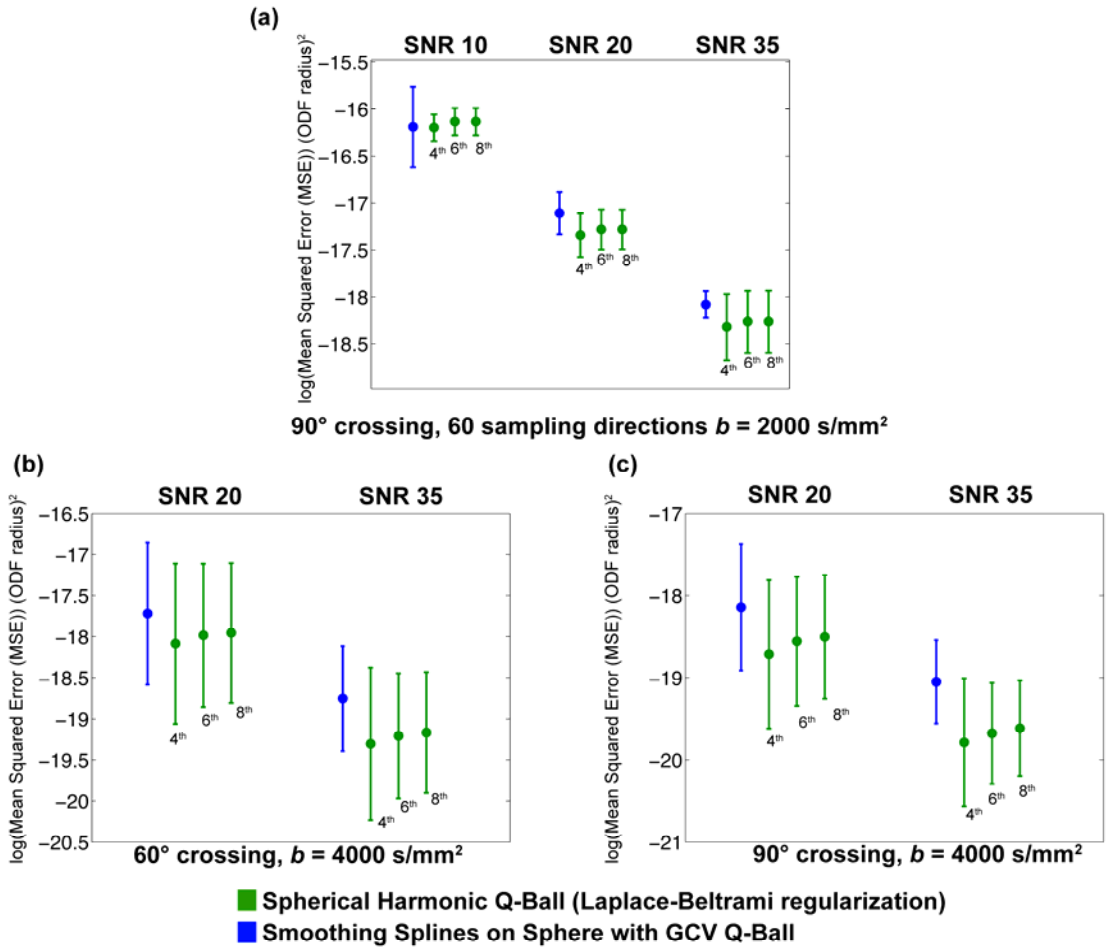

Figure 2.8 Orientation distribution functions (ODFs) reconstructed using smoothing splines on the sphere only slightly outperform their spherical harmonic QBI with Laplace-Beltrami regularization counterparts of order 6 and 8, in terms of mean squared error (MSE), at the low density sampling scheme of 60 directions with diffusion-weighting 2000 s/mm^2 and SNR level of SNR = 10, Figure 2.8(a). The spherical harmonic QBI ODFs with Laplace-Beltrami regularization outperform the smoothing splines ODFs in terms of lower MSE, in all other simulated cases, at low and high density HARDI sampling and at all SNR levels simulated, Figure 2.8(b) and 2.8(c).

2.4.1.4 Applying adaptive smoothing to spherical harmonic Q-ball imaging (QBI) with Laplace-Beltrami regularization using generalized cross-validation (GCV)

There are two parameters in the spherical harmonic QBI with Laplace-Beltrami regularization approach which need to be determined or set a priori to any processing.

The first is the value of the regularization parameter, λ, and the second is the order to which the spherical harmonic expansion extends. In an attempt to further automate this approach to spherical harmonic QBI, GCV was used to automatically determine a regularization value guided by the data SNR and was also used, in a separate simulation, to determine the spherical harmonic expansion order.

When choosing the regularization parameter value from a minimization of a GCV criterion, it was only at the low density HARDI sampling scheme (60 directions) and the very low SNR of 10 at which there was an improvement in terms of ODF radii MSE estimates over the original spherical harmonic QBI with Laplace-Beltrami regularization technique, Figure 2.9(a). In all other simulated cases, at low and high density HARDI sampling and at all SNR levels simulated, setting the regularization parameter value at $\lambda = 0.006$ lead to ODF radii with lower MSE estimates than when the regularization parameter value was chosen by GCV, Figure 2.9(b) and 2.9(c).

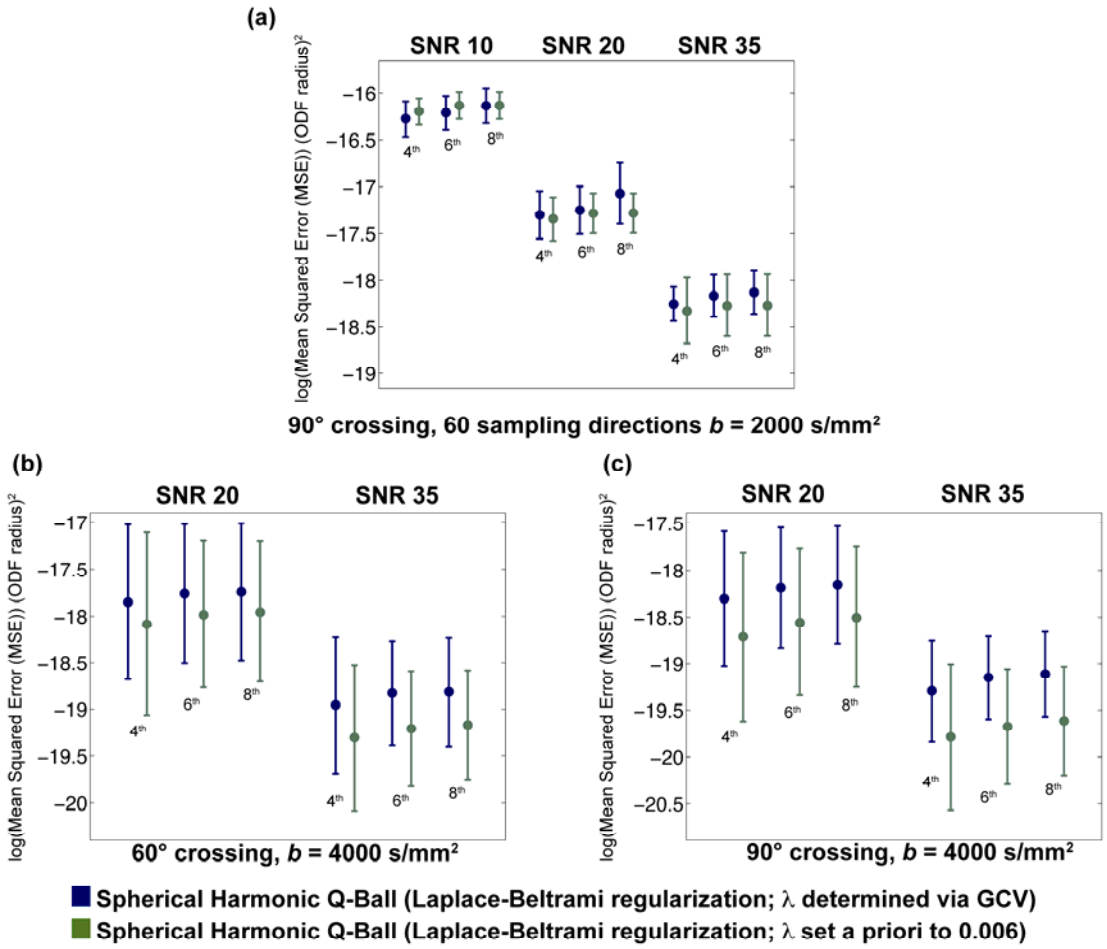

Figure 2.9 Using a generalized cross-validation (GCV) criterion in choosing the regularization parameter value in the spherical harmonic QBI approach with Laplace-Beltrami regularization does not - in general - lead to an improvement in the ODF radii mean squared error (MSE) estimates compared to the original approach in which the regularization parameter was set a priori to $\lambda = 0.006$.

Using GCV in choosing the spherical harmonic expansion order lead to ODFs with MSE estimates that were very comparable to those obtained using the original algorithm – for the simulated SNR levels and spherical harmonic expansion orders – in the low-density HARDI sampling scheme with diffusion-weighting 2000 s/mm^2, Figure 2.10 (a). However, performance deteriorates in the high-density HARDI sampling with elevated diffusion-weighting as is evident in Figure 2.10(b) and 2.10(c)

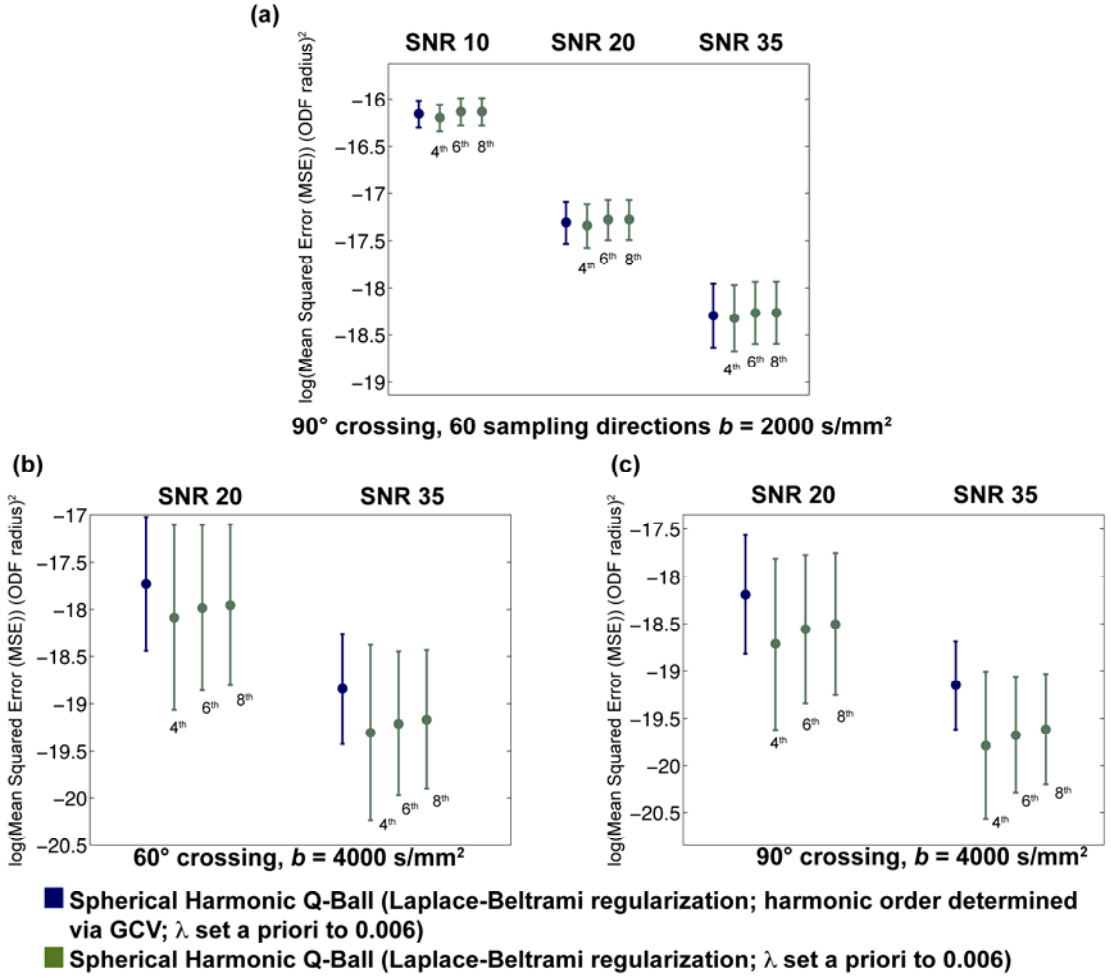

Figure 2.10 Using a generalized cross-validation (GCV) criterion in choosing the spherical harmonic order offers mixed results in the low-density sampling and low diffusion-weighting, Figure 2.10(a), and high-density sampling with high diffusion-weighting settings, Figure 2.10(b) and 2.10(c) .

In summary, using GCV whether in choosing the regularization parameter value or the spherical harmonic expansion order merely adds further computational burden with no improvement, in general, in the MSE. In these studies, bias in the estimates was slightly increased using GCV over the original algorithms and that, most likely, was the main contributor to the poor MSE performance.

2.4.1.5 Angular resolution comparisons

Angular resolution in QBI depends on the *b*-weighting, data SNR, amount of smoothing applied i.e. smoothing kernel width, spherical sampling density, and the ODF reconstruction directions density. It is expected that any smoothing done on the diffusivity profiles in diffusion space prior to ODF reconstruction would introduce some angular error in the crossing angles simulated. Applying smoothing splines on the sphere lead to an underestimation of the fiber crossing angles estimated below 75° compared to all QBI approaches. However for fiber crossing angles above 75°, the angles extracted from the smoothing splines on the sphere ODFs were closer to the ground truth ODF crossing angles compared to the angles from their analytical QBI ODF counterparts, Table 2-2. The smoothing splines ODFs exhibited comparable performance at 90° crossing with the spherical harmonic QBI ODFs with Tikhonov regularization and Laplace Beltrami regularization, Table 2-2. The smoothing splines ODFs and spherical harmonic QBI ODFs also exhibited less variability in the estimated fiber crossing angles compared to the analytical QBI ODFs.

Table 2-2: Average fiber crossing angles estimated using existing QBI methods and smoothing splines on the sphere for two crossing angle scenarios: 75° and 90°.

b = 4000 s/mm^2												
	SNR 20				**SNR 35**				**SNR 50**			
	QBI	ShQBI (T)	ShQBI (LB)	Smoothing Splines	QBI	ShQBI (T)	ShQBI (LB)	Smoothing Splines	QBI	ShQBI (T)	ShQBI (LB)	Smoothing Splines
75°	69° (13°)	69° (7°)	68° (9°)	66° (13°)	72° (8°)	71° (3°)	71° (3°)	71° (3°)	72° (5°)	72° (2°)	71° (2°)	71° (2°)
90°	80° (7°)	85° (3°)	86° (3°)	86° (3°)	85° (4°)	89° (1°)	90° (0°)	89° (1°)	88° (2°)	90° (0°)	90° (0°)	90° (0°)

The angles in the leftmost column are the true simulated fiber crossing angles. The values in the rest of the table are the average crossing angle estimates from all noise trials with the standard deviation in parentheses. 'ShQBI (T)' is spherical harmonic QBI with Tikhonov regularization and 'ShQBI (LB) is spherical harmonic QBI with Laplace-Beltrami regularization. All spherical harmonic QBI ODFs presented here were of the 6^{th} order harmonic with $\lambda = 2$ as the regularization parameter value for Tikhonov regularization and $\lambda = 0.006$ for the Laplace-Beltrami regularization approach. The diffusion-weighted data in this table was sampled with 252 sampling directions and the ODFs were reconstructed at 642 directions.

2.4.2 *In Vivo* Human Brain Data

The human data show an overall good agreement between the ODFs reconstructed directly from the raw data using existing QBI methods and those reconstructed after applying smoothing splines on the sphere with GCV smoothing as can be seen in Figures 2.11 and 2.12. The reconstructed ODFs from all methods compare nicely to previous works and investigations of the chosen regions-of-interest (ROIs) (21, 11). Figure 2.11 shows in vivo diffusion-weighted data sampled with 60 diffusion directions at $b = 2000$ s/mm^2 with an ROI in the parietal lobe where projections from the corpus callosum (CC) meet fiber projections from the internal capsule (IC) in the inferior-superior direction and posterior-anterior fibers of the superior longitudinal fasciculus (SLF). All methods perform comparably well depicting the underlying directionality in the data in the CC, showing fibers oriented in the left-right directions (encoded in red) and for the IC depicting fibers oriented in the inferior-superior directions (encoded in blue). However, spherical harmonic QBI ODFs with Laplace-Beltrami regularization and smoothing splines ODFs in the SLF region show more prominent ODFs indicating potential fiber crossings, in the upper right corner of their respective panels. This potential crossing is a little less obvious in the SLF QBI ODFs of analytical QBI. For analytical QBI, while the interpolation kernel width was determined by the minimizer of the log condition number of the sRBF interpolation matrix (11), the smoothing kernel width had to be changed and tested through trial-and-error to set the width that gave the best looking ODFs visually resembling ODFs in the remaining methods. For the spherical harmonic QBI approaches, the regularization parameter values $\lambda = 2$ and $\lambda = 0.006$ were used in the reconstruction of the spherical harmonic QBI ODFs

with Tikhonov regularization and Laplace-Beltrami regularization, respectively. A 4^{th} order harmonic expansion was used in ODF reconstruction for the spherical harmonic QBI with Tikhonov regularization while an 8^{th} order harmonic expansion was used for the spherical harmonic QBI with Laplace-Beltrami regularization. The regularization parameter value settings were the recommendations of their authors (12, 13). The smoothing parameter values estimated via GCV in the ROI in Figure 2.9 ranged from a minimum value of 10^{-5} to a maximum of 1.259×10^{-1}. The average smoothing parameter value over the entire ROI was 1.80426×10^{-3}.

Figure 2.12 shows data from the volunteer sampled with 256 diffusion directions at $b = 4000$ s/mm^2 with an ROI in the three-way fiber crossing area of the CC projections and corona radiata (CR) with the SLF. The QBI ODFs (upper left panel) are not as smooth as their counterparts from the spherical harmonic QBI approaches and smoothing splines on the sphere, especially in the CR and SLF regions. Three-way crossings between the CC, CR and SLF are more visible with the spherical harmonic QBI ODFs of both regularization approaches and smoothing splines ODFs in the SLF region (lower right panel) than with the analytical QBI ODFs. The GCV smoothing parameter values in the smoothing splines ODFs in the ROI in Figure 2.10 ranged from a minimum value of 6.3096×10^{-4} to a maximum of 10^{-1}. The average GCV smoothing parameter value over the entire ROI was 9.35704×10^{-3}. Again, the regularization parameter values $\lambda = 2$ and $\lambda = 0.006$ were used in the reconstruction of the spherical harmonic QBI ODFs with Tikhonov regularization and Laplace-Beltrami regularization, respectively, and with a 6^{th} order harmonic expansion. All ODFs were normalized as in (11) for visualization

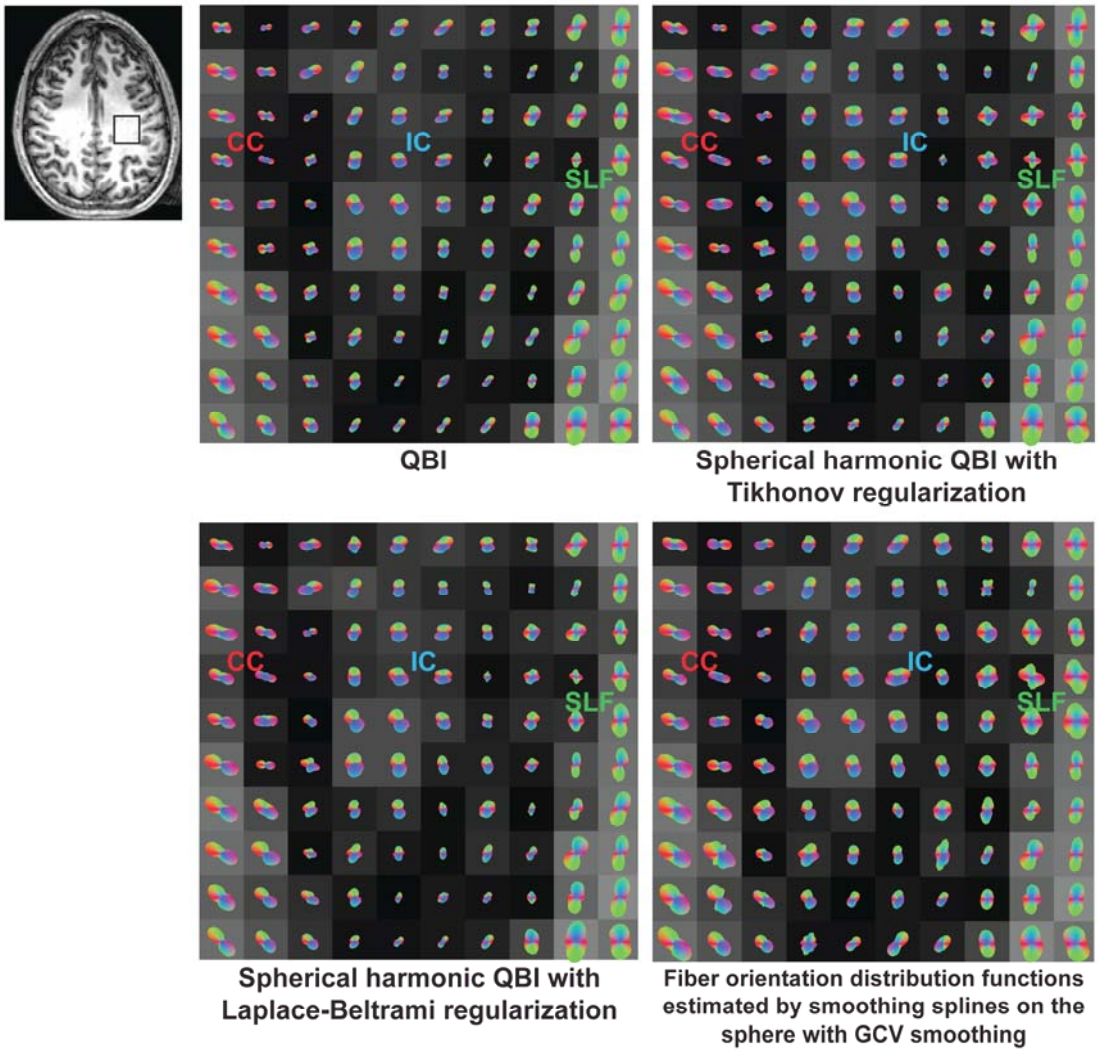

Figure 2.11 In vivo diffusion-weighted data sampled with 60 directions at b = 2000 s/mm^2 with a region-of-interest (ROI) outlined in black in the parietal lobe where projections from the corpus callosum (CC) meet fiber projections from the internal capsule (IC) in the inferior-superior direction and posterior-anterior fibers of the superior longitudinal fasciculus (SLF) on the T1-weighted MPRAGE image of the volunteer, upper left image. All methods are comparable depicting the underlying directionality in the data in the CC, showing fibers oriented in the left-right directions (encoded in red) and for the IC oriented in the inferior-superior directions (encoded in blue). The regularization parameter values $\lambda = 2$ and $\lambda = 0.006$ were used in the reconstruction of the spherical harmonic QBI ODFs with Tikhonov regularization and Laplace-Beltrami regularization, respectively. Spherical harmonic QBI ODFs with Laplace-Beltrami regularization and smoothing splines ODFs in the SLF region show more prominent ODFs indicating potential fiber crossings, in the upper right corner of the respective panesl. This potential crossing is a little less obvious in the SLF QBI ODFs of analytical QBI.

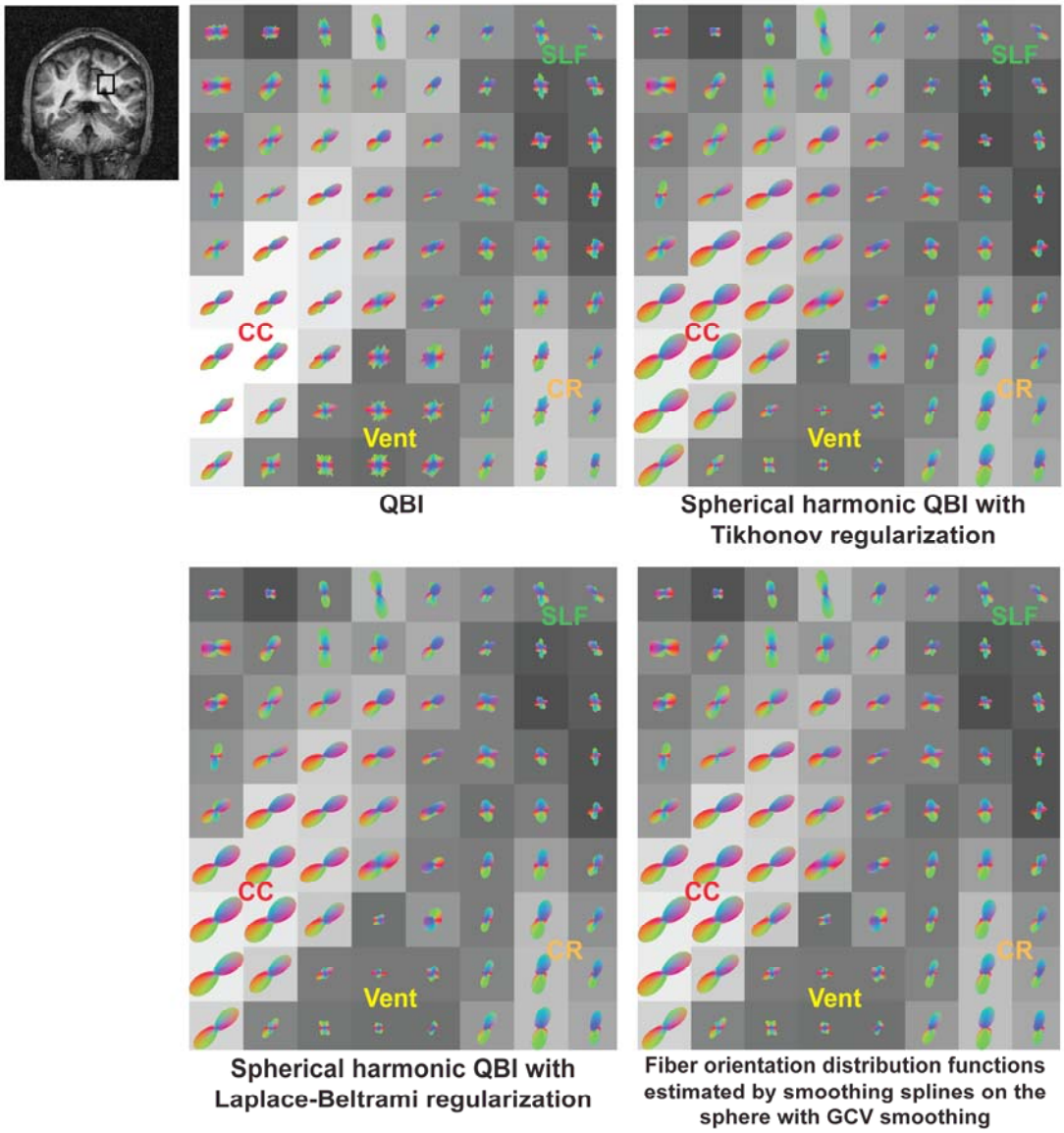

Figure 2.12 In vivo data sampled with 256 diffusion directions at b = 4000 s/mm^2 with a region-of-interest (ROI) outlined in black in the parietal lobe in the three-way fiber crossing area of the corpus callosum (CC) projections and corona radiata (CR) with the superior longitudinal fasciculus (SLF). Three-way crossings between the CC, CR and SLF are more visible with the spherical harmonic QBI ODFs of both approaches and with the smoothing splines ODFs in the SLF region (lower right panel) than with the analytical QBI ODFs (upper left panel). The regularization parameter values $\lambda = 2$ and $\lambda = 0.006$ were used in the reconstruction of the spherical harmonic QBI ODFs with Tikhonov regularization and Laplace-Beltrami regularization, respectively.

purposes and were displayed overlaying the generalized fractional anisotropy (GFA) metric also calculated as in (11). The GFA metric varies as its DTI counterpart, the fractional anisotropy (FA) (26), from zero for isotropic tissue to one for highly anisotropic tissue.

2.5 Discussion

Applying smoothing splines on the sphere with GCV smoothing to noisy simulated raw HARDI data prior to ODF reconstruction using the FRT minimizes the MSE in the ODF radii. The smoothing splines ODFs exhibit lower MSE estimates than their counterparts from the standard QBI algorithm across the different crossing angle scenarios and levels of SNR simulated. The smoothing splines ODFs had lower MSE estimates than their counterparts of the spherical harmonic QBI with Tickhonov regularization of all harmonic orders for the 90° crossing case at the low density HARDI sampling scheme (60 directions) at b = 2000 s/mm^2 for all SNR levels tested with the exception of the spherical harmonic ODFs with the 4th harmonic expansion at SNR = 35 that actually had lower MSE estimates than the smoothing splines ODFs. At higher HARDI sampling density (252 directions) and higher diffusion-weightings (b = 4000 s/mm^2) and for the SNR levels tested, the spherical harmonic QBI ODFs with Tikhonov regularization outperform their counterparts from the smoothing splines on the sphere approach even though adaptive smoothing is applied in the latter and not the former. In relation to the spherical harmonic QBI approach with Laplace-Beltrami regularization, the cases in which the smoothing splines ODFs slightly outperformed their spherical

harmonic counterparts were fewer. At low HARDI sampling density (60 directions), low SNR (SNR = 10) and low diffusion-weighting (b = 2000 s/mm^2), the smoothing splines ODF MSE estimates were the same or slightly lower than their spherical harmonic QBI ODF MSE estimates for all spherical harmonic order expansions. In all other simulation cases of higher sampling density and SNR, the spherical harmonic ODFs exhibited lower MSE estimates than their smoothing splines counterparts in the vast majority of simulated cases studied.

These results seem to suggest that when the SNR is poor, and low HARDI angular sampling densities and low diffusion weighting are used, the smoothing splines on the sphere reconstructed ODFs are, for the most part, more accurate in terms of MSE estimates than the ODFs from either spherical harmonic QBI approaches. This is possibly due to the fact that the regularization parameters for the spherical harmonic QBI approaches have been set a priori by the developers of each approach to work well within a range of SNR levels and diffusion-weightings. This essentially means that these setting will work very well in some situations and not as well in others as the results here suggest. When an objective method such as GCV is used in choosing the smoothing parameter, the selection is guided exclusively by the underlying data SNR. Surprisingly however, when a GCV criterion was used in choosing an objective value for the regularization parameter in this spherical harmonic QBI approach, it did not lead – in general - to ODFs with lower MSE estimates than the original spherical harmonic QBI with Laplace-Beltrami regularization with regularization parameter set a priori at λ = 0.006. GCV lead to a decrease in the MSE in this case and in the case of the smoothing

spline estimate but did not always lead to an estimate with the lowest MSE. GCV maybe an objective means of choosing the smoothing parameter but may not be the most optimal in terms of getting an estimate with the lowest MSE.

The spherical harmonic QBI approaches exhibited slightly better angular resolution power than the smoothing splines on the sphere approach at SNR = 20 as is evident from the noisy data in Table 2-2. However, the smoothing splines approach's performance improves at higher SNR and was comparable to the spherical harmonic QBI approaches. Both spherical harmonic QBI approaches and the smoothing splines approach reconstruct better 90° crossing angle ODFs across the simulated SNR levels compared to analytical QBI.

An additional limitation to the smoothing splines on the sphere approach with GCV smoothing is the added computational burden of locating the smoothing parameter value that minimizes the GCV criterion. This is largely due to the brute force nature of the search. Applying optimization in the GCV criterion minimization step would dramatically improve efficiency in the smoothing splines estimation problem. Furthermore, it is assumed when modeling the noisy diffusion-weighted data in Eq. [2.2] that the noise is zero mean with constant variance. The zero mean assumption is not accurate at all SNR levels. At high SNR, a Gaussian distribution assumption of the noise is a good approximation to the true Rician distribution however the approximation is inaccurate at low SNR levels that are typical of high diffusion-weighted HARDI data. This is likely leading to the increase in bias variability in the smoothing splines on the

sphere estimate. At high diffusion-weightings, the noise variance may not be constant along all sampling directions and will most likely be directly affected by the local diffusivity profile structure projected along the particular sampling directions. In the linear system solution, Eq. [2.6], the GCV smoothing parameter is applied with equal weighting over the entire function. Directions with more noise would require more smoothing which would not be achieved with the current method. Directionally heterogeneous variance could be addressed with a weighted estimation of the smoothing spline with the weights determined through optimization techniques.

As pertains to the *in vivo* brain datasets used, smoothing splines ODFs were comparable to all existing QBI methods in revealing the underlying directionality of the fibers in the 60 diffusion direction dataset. Like the spherical harmonic QBI ODFs with Tikhonov and Laplace-Beltrami regularizations, the smoothing splines on the sphere ODFs were devoid of small perturbations and spurious spikes due to noise that still persisted in the QBI ODFs in the 256 direction dataset. It is important to note that with the analytical QBI and spherical harmonic QBI approaches, a selection of the smoothing kernel width in the former and spherical harmonic expansion order selection in the latter need to be made. This represents an added burden in these approaches which essentially entails reconstructing the ODFs in any ROI several times with different smoothing kernel width settings and spherical harmonic expansion order numbers to choose, again subjectively, the most appropriate values, visually. Using an objective criterion, as with GCV, in selecting the amount of smoothing the data must undergo eliminates this exercise.

2.6 Conclusions

In this chapter, smoothing splines on the sphere modeling with GCV smoothing was applied to noisy HARDI data in order to estimate the underlying smooth diffusivity profiles. Using GCV in choosing the smoothing parameter value leads to adaptability of the smoothing applied concurrent with the data SNR. The smoothing splines on the sphere method with GCV smoothing when applied to the noisy raw HARDI data lead to better reconstructed ODFs, in terms of MSE, using the FRT as compared with ODFs reconstructed by the standard QBI algorithm in all simulated scenarios. GCV leads to a decrease in the MSE of the estimated spline however does not always lead to the smoothing spline estimate with the lowest MSE in the ODF radii. GCV maybe an objective means of choosing the smoothing parameter but clearly is not the optimal choice. In situations when SNR of the acquired data is very poor, diffusion-weighting low to mid-range with HARDI scans of low angular sampling densities (60 diffusion sampling directions), smoothing splines ODFs are more accurate than ODFs from existing QBI methods.

2.7 References

1. Grinstead JW, Sinha U, Sinha S. Application of a wavelet packet denoising algorithm to diffusion tensor images. In: Proceedings of the 10th Annual Meeting of the ISMRM, 2002, p. 155.

2. Pajevic S, Rohde GK, Basser PJ, Aldroubi A. Non-homogeneous wavelet denoising. In: Proceedings of the 12th Annual Meeting of the ISMRM, Kyoto, Japan, 2004, p. 2223.

3. Wirestam R, Bibic A, Lätt J, Brockstedt S, Ståhlberg F. Denoising of complex MRI data by wavelet-domain filtering: application to high-b-value diffusion-weighted imaging. Magn Reson Med 2006; 56: 1114-1120.

4. Perona P, Malik J. Scale-space and edge detection using anisotropic diffusion. IEEE Trans Patt Anal Machine Intell 1990; 12: 629-639.

5. Parker GJM, Schnabel JA, Symms MR, Werring DJ, Barker GJ. Nonlinear image smoothing for reduction of systematic and random errors in diffusion tensor imaging. J Magn Reson Imag 2000; 11: 702-710.

6. Ding Z, Gore JC, Anderson AW. Reduction of Noise in Diffusion Tensor Images Using Anisotropic Smoothing. Magn Reson Med 2005; 53: 485-490.

7. McGraw T, Vemuri BC, Chen Y, Rao M, Mareci T. DT-MRI denoising and neuronal fiber tracking. Med Imag Anal 2004; 8(2): 95-111.

8. Chen B, Hsu EW. Noise removal in magnetic resonance diffusion tensor imaging. Magn Reson Med 2005; 54: 393-401.

9. Hahn KR, Prigarin S, Hasan K. A novel denoising technique for very noisy diffusion tensor imaging data. In: Proceedings of the 12th Annual Meeting of the ISMRM, Kyoto, Japan, 2004, p. 1208.

10. Papadakis N, Smponias T. A continuous function approximation of scattered data on the sphere: application to diffusion tensor MRI. In: Proceedings of the 13th Annual Meeting of the ISMRM, Miami, Florida, 2005, p. 1225.

11. Tuch DS. Q-ball imaging. Magn Reson Med 2004; 52: 1358-1372.

12. Hess CP, Mukherjee P, Han ET, Xu D, Vigneron DB. Q-Ball reconstruction of multimodal fiber orientations using the spherical harmonic basis. Magn Reson Med 2006; 56: 104-117.

13. Descoteaux M, Angelino E, Fitzgibbons S, Deriche R. Regularized, fast, and robust analytical Q-Ball imaging. Magn Reson Med 2007; 58: 497-510.

14. Descoteaux M, Angelino E, Fitzgibbons S, Deriche R. Apparent diffusion coefficients from high angular resolution diffusion imaging: Estimation and applications. Magn Reson Med 2006; 56: 395-410.

15. Tournier J-D, Calamante F, Connely A. Robust determination of the fibre orientation distribution in diffusion MRI: non-negativity constrained super-resolved spherical deconvolution. NeuroImage 2007; 35: 1459-1472.

16. Wahba G. Spline interpolation and smoothing on the sphere. J Sci Stats Comput 1981; 2: 5-16.

17. Craven P, Wahba G. Smoothing noisy data with spline functions: estimating the correct degree of smoothing by the method of generalized cross-validation. Numer Math 1979; 31: 377-403.

18. Gu C. Smoothing Spline ANOVA Models. Springer-Verlag New York, New York, NY, USA; 2002.

19. Carew JD, Wahba G, Xie X, Nordheim EV, Elizabeth Meyerand M. Optimal spline smoothing of fMRI time series by generalized cross-validation. NeuroImage 2003; 18: 950-961.

20. Kaden E, Knosche TR, Anwander A. Parametric spherical deconvolution: inferring anatomical connectivity using diffusion MR imaging. NeuroImage 2007; 37: 474-488.

21. Kaden E, Anwander A, Knosche TR. Variational inference of the fiber orientation density using diffusion MR imaging. NeuroImage 2008; 42: 1366-1380.

22. Sakaie KE, Lowe MJ. An objective method for regularization of fiber orientation distributions derived from diffusion-weighted MRI. NeuroImage 2007; 34: 169-176.

23. Mukherjee P, Hess CP, Xu D, Han ET, Kelley DA, Vigneron DB. Development and initial evaluation of 7-T *q*-ball imaging of the human brain. Magn Reson Imag 2008; 26: 171-180.

24. Alexander DC, Barker GJ, Arridge S R. Detection and modeling of non-Gaussian apparent diffusion coefficient profiles in human brain data, Magn Reson Med 2002; 48: 331-340.

25. Tuch DS, Reese TG, Wiegell MR, Wedeen VJ. Diffusion MRI of complex neural architecture. Neuron 2003; 40: 885-895.

26. Pierpaoli C, Basser PJ. Toward a quantitative assessment of diffusion anisotropy. Magn Reson Med 1996; 36: 893-906.

27. Anderson AW. Measurement of fiber orientation distributions using high angular resolution diffusion imaging. Magn Reson Med 2005; 54: 1194-1206.

28. Jones DK. The Effect of gradient sampling schemes on measures derived from diffusion tensor MRI: a Monte Carlo study. Magn Reson Med 2004; 51: 807-815.

29. Tuch DS. Diffusion MRI of complex tissue structure. Ph.D. thesis, Division of Health Sciences and Technology, Harvard-MIT, MA, 2002.

30. Wu Y-C, Alexander AL. Hybrid diffusion imaging. NeuroImage 2007; 36: 617-629.

31. Berman JI, Chung S, Mukherjee P. Hess CP, Han ET, Henry RG. Probabilistic streamline Q-Ball tractography using the residual bootstrap. NeuroImage 2008; 39: 215-222.

CHAPTER 3

TOWARDS AN OBJECTIVE MARKER FOR UPPER MOTOR NEURON INVOLVEMENT IN AMYOTROPHIC LATERAL SCLEROSIS: A HIGH ANGULAR RESOLUTION DIFFUSION-WEIGHTED IMAGING STUDY[2]

This chapter applies high angular resolution diffusion-weighted imaging (HARDI) in subjects clinically diagnosed with amyotrophic lateral sclerosis (ALS) and at the early stages of the disease to investigate diffusion-sensitive changes in upper motor neuron (UMN) white matter as well as brain white matter in general. Currently, there are no widely accepted objective markers for upper motor neuron involvement in ALS. The diffusion tensor imaging (DTI) measures axial diffusivity ($\lambda_{\|}$), radial diffusivity ($\lambda_{\perp}$), in addition to the more commonly used fractional anisotropy (FA) and mean diffusivity (MD) were studied using the voxel-based statistical analysis tool, tract-based spatial statistics (TBSS). This study represents the first report of changes in MD, $\lambda_{\|}$, and $\lambda_{\perp}$ in ALS patients using TBSS and finds that MD, $\lambda_{\|}$, and $\lambda_{\perp}$ were significantly increased along the corticospinal tract (CST) of the UMN in ALS patients while significant changes in FA were more restricted. In ALS, $\lambda_{\|}$ and $\lambda_{\perp}$ may be useful DTI-derived indices to

---

[2] Partial work in this chapter has been accepted for publication as "Metwalli NS, Benatar M, Nair G, Usher S, Hu X, Carew JD. Utility of axial and radial diffusivity from diffusion tensor MRI as markers of neurodegeneration in amyotrophic lateral sclerosis. Brain Research 2010, In Press.

consider in addition to FA and MD to aid in demonstrating neurodegenerative changes associated with the disease. Applying generalized cross-validated (GCV) smoothing via smoothing splines on the spheres lead to objectively smoothed orientation distribution functions (ODFs) with suppressed spurious peaks that mislead fiber tractography.

3.1 Introduction

Amyotrophic lateral sclerosis (ALS) is a debilitating neurodegenerative disease characterized by the death of both the upper motor neurons (UMN) and lower motor neurons (LMN) in the brain, brainstem, and spinal cord. The disease results in weakness and wasting of muscles, impaired swallowing and ultimately death from respiratory failure (1). Currently, there is no specific test for ALS, which remains a clinical diagnosis. The clinical LMN signs can be demonstrated though electromyography and motor unit number estimation. Electromyography is an invasive test that evaluates the health of muscles and the nerves controlling them while motor unit number estimation is a non-invasive electrophysiological method to estimate the number of motor neurons innervating a muscle or group of muscles (2). Signs of UMN degeneration are more difficult to asses, especially when the disease is at its early stages and the UMN signs are very discrete. There is no widely accepted objective marker for UMN involvement in ALS (3).

Axonal degeneration in ALS alters tissue microstructure and hence diffusion of water molecules both perpendicular and parallel to the axonal wall. These changes, which

are not evident on conventional MRI, are measurable with diffusion tensor imaging (DTI). Sensitivity to microstructure and tissue organization makes DTI an important tool for studying neurodegenerative disease (4). Several measures derived from the diffusion tensor, **D**, have been shown valuable in characterizing microstructural diffusion occurring in the underlying tissue. These measures include trace, fractional anisotropy (FA), mean diffusivity (MD) (5), radial diffusivity ($\lambda_{\perp}$) and axial diffusivity ($\lambda_{\parallel}$) (6). The trace of **D** is the sum of the three eigenvalues while MD is the average of the three eigenvalues (MD = trace/3) and provides a measure of the degree of restriction to the diffusion of water molecules irrespective of direction (7). Conceptually, FA measures the eccentricity, or degree of anisotropy of diffusion (5, 8). FA values range from 0 (isotropic diffusion) to 1 (completely anisotropic diffusion). In anisotropic tissue, such as white matter, the largest eigenvalue represents the diffusivity of water in the direction parallel to the fiber bundles ($\lambda_{\parallel}$). Radial diffusivity, $\lambda_{\perp}$, which is the average of the two smallest eigenvalues, measures water diffusion perpendicular to the axonal wall. FA and MD have been used in the study of a variety of brain white matter pathologies (9-11) including primary lateral sclerosis (PLS) and ALS. However, there has been little study of the utility of $\lambda_{\parallel}$ and $\lambda_{\perp}$ in ALS.

Methods of quantitative DTI analysis include region-of-interest (ROI) and voxel-based approaches. Tract-based spatial statistics (TBSS) (12), the voxel-based approach used in this chapter, utilizes extracted and skeletonized white matter tracts in the FA images of all subjects. TBSS is used in an effort to overcome the problems associated with the use of standard registration algorithms in other voxel-based approaches.

Several investigators have reported reduced FA in the corticospinal tracts (CSTs) of ALS patients although the extent and distribution of these changes have been variable (3, 12-23). Reduced FA along the entire length of the CST from the corona radiata (CR) through the internal capsule (IC) and into the brainstem has been reported using both ROI (13, 17, 21) and voxel-based approaches (14, 18, 20, 23). Other reports have described more regionally restricted reductions in FA affecting only the posterior limb of the internal capsule (15), the brainstem (3, 19) or a gradient of FA reduction that was most marked in the pons, less prominent in the IC, and normal in the CR (16). Inconsistent results were reported in one of the studies that utilized TBSS (22). Furthermore, in a more recent TBSS analysis of subjects included in their first voxel-based study, Sage et al. reported finding reductions in FA in the splenium and body of the corpus callosum (CC) in addition to the previously reported reductions in the CST (23) (Table 3-1).

Table 3-1: Previously reported fractional anisotropy (FA) findings in the corticospinal tract (CST) and corpus callosum of patients with ALS.

Reference	Corona radiata	Posterior limb of the internal capsule	Cerebral peduncles	Pons	Medulla	Corpus callosum
Ellis et al. (13)	↓	↓	↓	-	-	-
Sach et al. (14)	↓	↓	↓	↓	-	↓
Graham et al. (15)	NS	↓	-	-	-	NS
Karlsborg et al. (16)	NS	NS	-	↓	-	-
Hong et al. (3)	-	-	↓	NS	NS	-
Cosottini et al. (17)	-	↓	↓	↓	↓	-
Thivard et al. (18)	↓	↓	-	-	-	-
Wong et al. (19)	NS	NS	↓	-	-	-
Sage et al. (20)	↓	↓	↓	NS	NS	NS
Iwata et al. (21)	↓	↓	↓	↓	↓	NS
Ciccarelli et al. (22)	↓	↓	↓	-	-	↓
Sage et al. (23)	↓	↓	↓	NS	NS	↓

'↓': *Significant decrease*. 'NS': *Not significant*. '–': *Not considered or reported*.

Reported changes in MD in ALS patients have been less consistent. Several studies have reported increased MD in selected regions of the CST of ALS patients – the IC more so than the pons, but not the CR (16), and the cerebral peduncles, but not the pons and medulla (3). Others found no significant differences in MD between patients and controls (15, 19). Cosottini et al. reported normal $\lambda_{\parallel}$ but increased $\lambda_{\perp}$ in ALS patients, indicating normal diffusion along the CST but increased diffusion perpendicular to the CST (17). However, Wong et al. found normal $\lambda_{\perp}$ but increased $\lambda_{\parallel}$ only in the CR of ALS patients (19). Using TBSS, Sage et al. reported finding significant increases in MD within the CST (23) in the same patients they had previously described (20) initially not finding those MD increases in the CST.

In this chapter, we apply high angular resolution diffusion-weighted imaging (HARDI) in subjects clinically diagnosed with ALS and at the early stages of the disease to investigate diffusion-sensitive changes in UMN white matter. We report DTI and TBSS analysis of FA, MD, $\lambda_{\parallel}$, and $\lambda_{\perp}$ maps of ALS patients and age-matched controls. We hypothesized that there would be utility in considering $\lambda_{\parallel}$ and $\lambda_{\perp}$ in addition to the more commonly considered FA and MD to aid in revealing neurodegenerative changes in ALS. This chapter presents the first report of changes in MD, $\lambda_{\parallel}$ and $\lambda_{\perp}$ in ALS patients using TBSS.

The diffusion tensor in DTI can have only one orientation maximum pointing in the direction where maximum diffusion occurs as was explained in Chapter 1. The resolution with which the data is acquired would lead to the existence of multiple

orientations due to fibers crossing or diverging within the millimeter scale voxels in numerous areas in the brain. These multiple orientations are problematic with DTI. A single fiber orientation estimate would be incorrectly identified as the mean of the underlying fiber directions that would mislead any fiber tractography applied to the data. HARDI data acquired at higher angular resolution facilitates the reconstruction of fiber orientation distribution functions (ODFs) that reveal multiple fiber orientations that would not be visible with DTI. QBI ODFs and generalized cross-validated (GCV) smoothing splines on the spheres ODFs are reconstructed to compare their respective performances with fiber crossing extraction and spurious peak suppression.

3.2 Methods

3.2.1 Study Participants

ALS patients were recruited from the neuromuscular clinic and electromyography laboratory at Emory University and via advertisements to ALS patients registered with the Georgia Chapter of the Muscular Dystrophy Association. Patients were examined clinically; the revised ALS functional rating scale (ALSFRS-R) (24) was administered and forced vital capacity (FVC) was measured. Age-matched healthy controls were recruited from several sources including spouses and other relatives of ALS patients and a registry of healthy subjects maintained by Dr. Michael Benatar, an associate professor of Neurology at Emory University's School of Medicine, and an investigator on this study. The study was approved by the Emory Institutional Review Board (IRB) and all participants provided written informed consent. Target enrollment was twelve ALS

patients and at least twelve controls. A total of twenty-one control subjects were recruited to achieve approximate age matching with the ALS group.

3.2.2 Study Protocol

HARDI data were acquired on a Siemens 3T Tim whole body system using a standard single-shot echo planar imaging (EPI) sequence in the coronal orientation with a twelve channel volume head coil. The imaging parameters were as follows: repetition time / echo time (TR/TE) = 3000/135 ms, field-of-view (FOV) = 135 mm x 135 mm, matrix size of 128 x 128, resolution of 1.1 x 1.1 mm^2, 16 coronal slices of 5 mm slice thickness were acquired with a 2.5 mm gap. Parallel imaging (GRAPPA) was employed with acceleration factor of 2 to reduce image distortions and scan time. Diffusion-weighting gradients were applied along 64 directions at *b*-value = 1000 s/mm^2 along with one whole brain volume with negligible diffusion weighting (*b*-value $\approx$ 0 s/mm^2, b0 image). Two consecutive acquisitions were made for subsequent averaging to increase the signal-to-noise ratio (SNR). Total acquisition time was 7 minutes and 30 seconds.

3.2.3 Diffusion Tensor Imaging (DTI) and Tract-based Spatial Statistics (TBSS) Analysis

The two acquisitions were corrected for eddy-current distortions and for simple head motion using an affine registration to the b0 image (25). All subject registrations had rotations less than 5° and translations less than 2 mm. Diffusion data with SNR below 10 in the b0 image were also excluded. FA and MD maps as well as the eigenvalue

maps were estimated for each subject using the FDT toolbox in FSL (26). Maps of $\lambda_{\parallel}$ and $\lambda_{\perp}$ were constructed.

The voxelwise statistical analysis of the FA maps using TBSS took the following steps:

1. All FA maps from all subjects were collected in a single folder and each subject's FA image was aligned into 1 x 1 x 1 mm^3 Montreal Neurological Institute (MNI152) standard space. The FSL standard space image template FMRIB58_FA was used as the target image for the alignment of each FA map. A single nonlinear registration step is involved per subject (27).

2. TBSS combined and averaged all transformed FA images to create a mean FA image of all subjects. This mean FA image was visually inspected to determine if the registration step was performed correctly by examining the areas of the major white matter tracts in the brain e.g. CC, IC, external capsule, etc.

3. The mean FA was then thinned and skeletonized within TBSS to create a mean FA skeleton that represents the centers of all tracts common to all subjects.

4. The mean FA skeleton image was visually inspected for the choice of an appropriate threshold that would exclude areas that were, on average, grey matter (low mean FA from all subjects) and/or had high inter-subject variability. The voxel-wise cross subject statistics were performed on the remaining mean FA

skeleton voxels surviving after application of the threshold. Obviously, this threshold is dependent on the quality of the diffusion data and as such is study specific. The threshold used in this study was set at 0.2 and a threshold value between 0.2 and 0.3 had been deemed appropriate (12).

5. TBSS then projected each subject's aligned FA image onto the mean FA skeleton. The goal being to assign each subjects FA skeleton map with the appropriate FA values from within the white matter tracts for that subject. The maximum FA value that was to be assigned for each voxel in each subject's FA skeleton image was found by performing a local search. The search direction taken was perpendicular to the local skeleton and was determined by the local gradient and second derivative of each subject's FA. This is significant in that all statistical analysis is ultimately performed on the raw unaltered and unwarped FA values in each subject.

6. The result was a 4D image of skeletonized FA maps with the fourth dimension being the individual subjects. Voxel-based statistics across subjects is performed on this 4D image.

7. A permutation test was performed in order to test for significant differences in the skeletonized FA maps between ALS patients and controls (28). Correction for multiple comparisons was also performed. For a more detailed overview of the performed permutation test the reader is referred to Nichols et al. (28). The

number of permutations to be performed was set at 10000. The resulting test statistic maps were thresholded using threshold-free cluster enhancement (29) with TBSS built-in 2D optimizations for white matter skeletons. A p-value <0.05 was considered to be statistically significant.

The MD, $\lambda_{\parallel}$ and $\lambda_{\perp}$ maps generated for all subjects were also aligned using the previous FA alignment transformation matrices. The MD, $\lambda_{\parallel}$ and $\lambda_{\perp}$ maps from all subjects were merged and subsequently projected onto the original mean FA skeleton, thinned and skeletonized. Permutation tests were used to test for significant differences in the skeletonized MD, $\lambda_{\parallel}$ and $\lambda_{\perp}$ maps between ALS patients and controls with the same parameters as previously specified.

The resulting TBSS statistic maps were thresholded at significance level $p<0.05$ (corrected for multiple comparisons by controlling the family-wise error rate). All TBSS results were displayed on the mean FA image of all studied subjects in standard space as the background.

In a separate analysis on the skeletonized measures, ROI volumes were outlined on the skeletons in standard space in the different regions along the CST as well as extra motor areas in all subjects guided by an anatomical atlas (30). The ROI volumes are shown in Figure 3.1 displayed on the mean FA image of all subjects. Mean skeletonized FA, MD, $\lambda_{\parallel}$, and $\lambda_{\perp}$ values in patients and controls were recorded and percentage changes

in these measures in ALS patients were calculated to compare with the findings from TBSS.

3.2.4 Correlation Analysis between Diffusion Tensor Imaging (DTI) and Clinical Measures of Disease Severity

Two separate correlation analyses were carried out. Initially a voxel-based correlation analysis was performed between the skeletonized FA, MD, $\lambda_{\parallel}$ and $\lambda_{\perp}$ of ALS patients and various clinical measures – the ALSFRS-R, FVC, and disease duration. A non-parametric permutation test was used to test the correlations. A significance level of $p<0.05$ (corrected for multiple comparisons by controlling the family-wise error rate) was the threshold used. Subsequently, a more focused ROI-based correlation analysis was attempted. The ROI volumes used in the analysis primarily included areas outlined in the CST such as the cerebral peduncles, posterior limb of the IC and the CR in addition to extra motor areas guided by an anatomical atlas (30). First, a simple linear regression was performed between the mean DTI measures in the ROIs of the ALS patients and their ages to control for the effect of age. The residuals from the fits were then used for the correlation analysis again by means of a simple linear regression. A p-value of $p<0.05$ was considered significant. The ROI-based correlation analysis was carried out in **R** (**R** Foundation for Statistical Computing, Vienna, Austria).

3.2.5 Adaptive Smoothing using Generalized Cross-validated (GCV) Smoothing Splines on the Sphere for Fiber Tractography

First, ODFs reconstructed using the standard QBI algorithm utilized widths for the interpolation and smoothing kernels of 10° and 15°, respectively. The widths for the interpolation kernels were the minimizers of the log condition number of the QBI interpolation matrix. The smoothing kernel widths were varied to the value that gave the best-looking ODFs visually. Second, prior to ODF reconstruction, the smoothing splines on the sphere functions with GCV smoothing parameters were estimated in each voxel. The searching grid for the smoothing parameter spanned, $\lambda \in \left[10^{-6}, 10^{2}\right]$ on a log scale with step size of 0.1 to identify the lambda that gave the minimum GCV criterion score. The Funk Radon transform (FRT), which is the basis of QBI, was applied to reconstruct the ODFs. For the smoothing splines on the sphere method, the smooth function estimate is defined everywhere on the sphere. Diffusion-weighted data were estimated at 48 evenly spaced points across each reconstruction direction equator plane and the signals were summed along each equator to estimate the ODF radii in the reconstruction directions. ODFs from QBI and splines on the sphere modeling were reconstructed at 252 icosahedral directions. ODF peaks coinciding with underlying dominant fiber orientations were identified and demarcated by drawing yellow lines passing through each peak and the center of the ODF. Only ODF peaks with radii passing a threshold of 0.75 of the maximum radius in each ODF were marked.

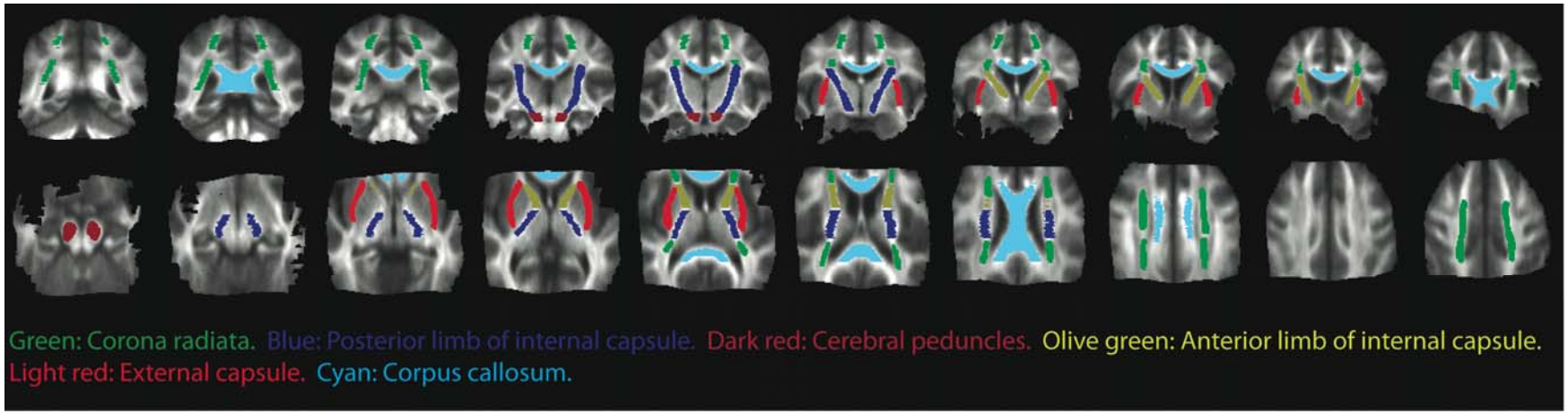

Figure 3.1 Region-of-interest (ROI) volumes outlined in standard space in regions along the corticospinal tract (CST) as well as other extra motor areas used for the ROI analysis. The ROI volumes were used in conjunction with the extracted mean fractional anisotropy (FA), mean diffusivity (MD), axial diffusivity ($\lambda_{//}$), and radial diffusivity ($\lambda_{\perp}$) maps to isolate the skeleton voxels upon which the ROI analysis was performed. The background image is the mean FA map for all subjects in MNI standard space.

3.3 Results

Of the twelve ALS patients (10 males, 2 females, mean age 56.2 ± 10.5 years), five patients were diagnosed with definite ALS according to the El Escorial criteria (24); two with probable ALS, four with possible ALS, and one with familial ALS. Mean ALSFRS-R score (±SD) was 41.3 ± 5.5 with mean disease duration of 26 ± 15 months, Table 3-2. The relatively high ALSFRS-R scores suggest that the study population included patients with relatively mild disease notwithstanding the relatively long duration of the disease and the high proportion of patients with El Escorial definite ALS. Twenty-one age-matched healthy controls were also scanned, two of whom were excluded because of an SNR < 10 in the b0 images. The analysis included the remaining nineteen healthy controls (11 males, 8 females, mean age 50.2 ± 12.7 years).

3.3.1 Fractional Anisotropy

FA was significantly reduced in the body and genu of the CC (16.2% decrease) and CR (14.8% decrease) in ALS patients compared to controls ($p<0.05$) (Figure 3.2(a), Table 3-3). No significant differences in FA were found along the CST tract in its course through the IC and cerebral peduncles (Figure 3.2(a), Table 3-3). There was, however, a trend towards a decrease in FA values in the white matter adjacent to the right precentral gyrus, anterior limb of the IC and the splenium of the CC in ALS patients ($p<0.1$).

Table 3-2: Detailed patient characteristics.

Patient	Sex	Age (years)	Disease Duration (months)	El-Escorial category	ALSFRS-R	FVC (% predicted)	Site of onset
PAT1	M	49	18.4	Definite	45	126%	Limb
PAT2	F	61	33.8	Definite	32	98%	Limb
PAT3	M	38	35.7	Definite	44	83%	Limb
PAT4	M	75	27.2	Probable	45	68%	Limb
PAT5	M	51	54.3	Definite	33	48%	Limb
PAT6	M	50	36.5	Possible	43	88%	Limb
PAT7	M	67	39.9	Possible	48	93%	Limb
PAT8	M	66	13.2	Possible	36	84%	Limb
PAT9	M	56	4.3	Familial	43	105%	Limb
PAT10	F	63	7.2	Possible	37	88%	Limb
PAT11	M	45	27.6	Definite	48	93%	Limb
PAT12	M	53	13.5	Probable	42	85%	Bulbar
	10M, 2F	56.2 ± 10.5	26 ± 15		41.3 ± 5.5		

Values in the last row for Age, Disease Duration and ALSFRS-R represent mean ± standard deviation.

3.3.2 Mean Diffusivity

MD was significantly increased along the CST, asymmetrically in the cerebral peduncles, bilaterally in the posterior limb of the IC (17.0% increase) and the CR (14.5% increase) as well as in the anterior limb of the IC, external capsule and the body, genu and splenium of the CC in ALS patients ($p<0.05$) (Figure 3.2(b), Table 3-3). The asymmetry of MD changes in the cerebral peduncles is likely due to image distortions in the mid-brain and brainstem regions. Significant increases in MD were also observed in several other white matter structures in ALS patients ($p<0.05$) (Figure 3.2(b), Table 3-3).

3.3.3 Axial Diffusivity

Among ALS patients, $\lambda_{\parallel}$ was significantly increased bilaterally in the posterior limb of the IC (14.0% increase), and the CR (12.1% increase), the anterior limb of the IC, external capsule as well as in the body, splenium and genu of the CC ($p<0.05$) (Figure 3.2(c)). $\lambda_{\parallel}$ was also significantly higher asymmetrically in the cerebral peduncle ($p<0.05$) (Figure 3.2(c), Table 3-3). Significant increases in $\lambda_{\parallel}$ were also observed in several other white matter structures in ALS patients ($p<0.05$) (Figure 3.2(c), Table 3-3).

3.3.4 Radial Diffusivity

Radial diffusivity, $\lambda_{\perp}$, was significantly increased in ALS patients over a more extensive region of the CST than the changes in FA, MD or $\lambda_{\parallel}$. Changes in $\lambda_{\perp}$ were most prominent bilaterally in the cerebral peduncles (39.3% increase), less so in the posterior limb of the IC (28.6% increase) and least so in the CR (16.3% increase) ($p<0.05$) (Figure 3.2(d),

Table 3-3). Significant increases in $\lambda_{\perp}$ in ALS patients were also found in other white matter structures ($p<0.05$) (Figures 3.2(d), Table 3-3).

3.3.5 Added Utility of Axial and Radial Diffusivity Measures

At higher levels of statistical significance ($p<0.005$), increases in $\lambda_{\perp}$ were still evident in the CST corona radiata, in white matter adjacent to the right precental gyrus, the anterior limb of the IC, right postcentral gyrus, right inferior frontal gyrus, and the body, splenium and genu of the CC in ALS patients (data not shown). There were no differences in FA, MD and $\lambda_{\parallel}$ between ALS patients and controls at these significance levels ($p<0.005$).

3.3.6 Lack of Correlation between Diffusion Tensor Imaging (DTI) and Measures of Disease Severity

Using both voxel and ROI-based approaches, there were no significant correlations between any of the DTI parameters and the various clinical measures of disease severity – ALSFRS-R, FVC, and disease duration – among patients with ALS.

3.3.7 Generalized Cross-validated (GCV) Smoothing Splines on the Sphere Orientation Distribution Function (ODF) and Q-Ball Imaging (QBI) ODF Comparisons

The GCV smoothing splines on the sphere ODFs show more consistency in extracting dominant fiber orientations in areas of fiber crossings over their QBI counterparts. In a fiber crossing area between the fiber projections of the body of the CC and projections from the posterior limb of the internal capsule, the GCV ODFs show more regularity and consistency

over the ROI area, even though the smoothing is done independently on a per-voxel basis (Figures 3.3 and 3.4). A number of QBI ODFs show persistent spurious peaks that have not been smoothed out effectively. The fear from spurious ODF peaks is that it would ultimately mislead and misguide fiber tracking.

3.4 Discussion and Conclusions

This is the first report of changes in MD, $\lambda_{\parallel}$ and $\lambda_{\perp}$ in ALS patients using TBSS. MD, $\lambda_{\parallel}$ and $\lambda_{\perp}$ were significantly increased along the CST in ALS patients. The changes in $\lambda_{\perp}$ were most marked in the ROI analyses and more widespread in the TBSS results than changes in FA, MD or $\lambda_{\parallel}$ (Table 3-3) suggesting that $\lambda_{\perp}$ may be the DTI-derived index that is more sensitive to the neurodegenerative process in ALS. Intuitively, parallel changes in $\lambda_{\parallel}$ and $\lambda_{\perp}$, the subcomponents of MD and FA, may not be apparent in the latter DTI measures. FA characterizes the eccentricity of the diffusion tensor, **D**; an increase (or decrease) in the primary eigenvalue of **D** (i.e., $\lambda_{\parallel}$) accompanied by an increase (or decrease) in the other two eigenvalues (which are measured by $\lambda_{\perp}$) may not lead to a change in the eccentricity of **D** so FA would remain unchanged. Similarly, since MD represents the average of diffusion in all directions, it provides no information about the direction in which diffusion is increasing or decreasing; $\lambda_{\parallel}$ and $\lambda_{\perp}$ by contrast provide just such information.

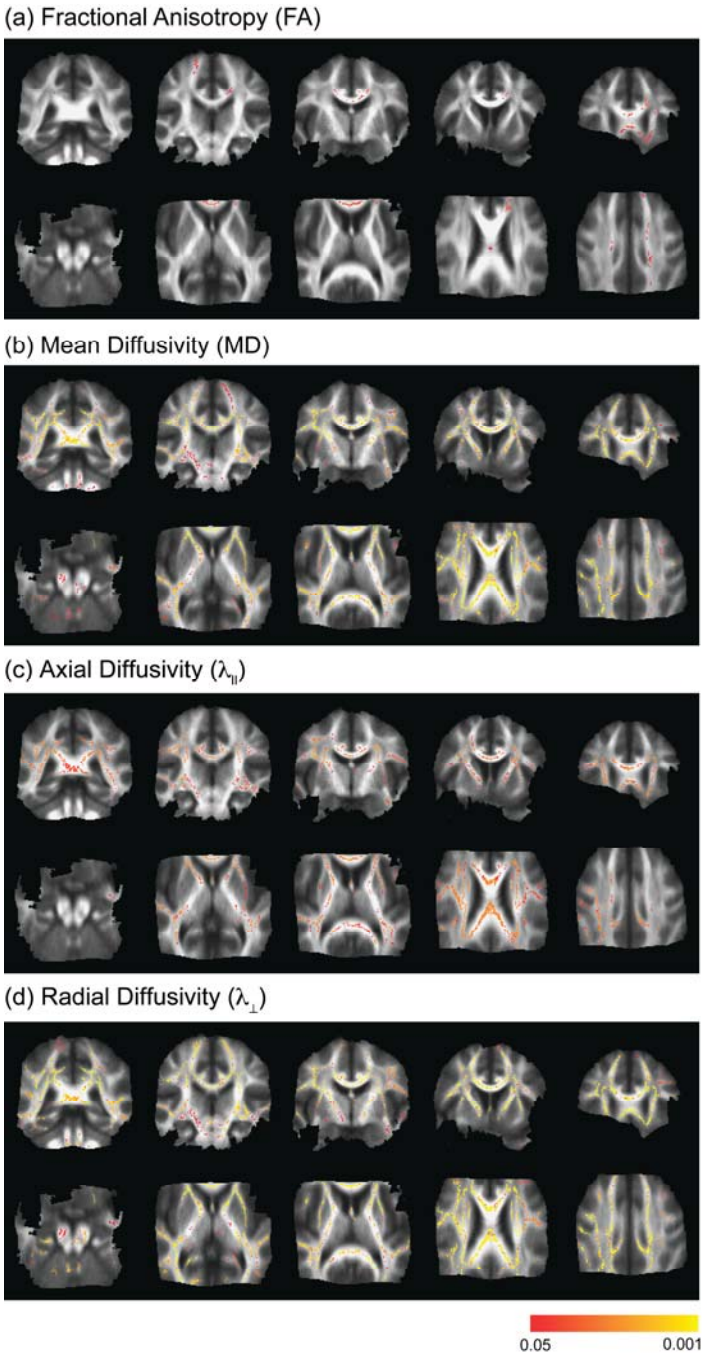

Figure 3.2 Widespread increases in radial diffusivity ($\lambda_{\perp}$) are seen in ALS patients. Voxels that show significant changes in (a) fractional anisotropy (FA), (b) mean diffusivity (MD), (c) axial diffusivity ($\lambda_{||}$) and (d) radial diffusivity ($\lambda_{\perp}$) in ALS patients are overlaid in color on coronal (upper row) and axial (lower row) slices of the mean FA image in Montreal Neurological Institute (MNI) standard space. The decrease in FA was confined to the corona radiata and the body and genu of the corpus callosum ($p<0.05$). MD and $\lambda_{||}$ increased more extensively along the entire corticospinal tract (CST), as well as in the corpus callosum of ALS patients ($p<0.05$). Increased $\lambda_{\perp}$ in ALS patients was more widespread and more prominent in the CST than the increases in MD or $\lambda_{||}$.

Table 3-3: Mean diffusion tensor imaging (DTI) measures in brain regions with significant differences between ALS patients and controls

Region	Measurement*	Controls	ALS	Change in ALS
Corona radiata	FA	0.54 ± 0.067	0.46 ± 0.070	14.8 % ↓
	MD	0.62 ±0.060	0.71 ± 0.073	14.5 % ↑
	λ_{II}	0.99 ± 0.12	1.11 ± 0.13	12.1 % ↑
	$\lambda_{\perp}$	0.43 ± 0.062	0.50 ± 0.076	16.3 % ↑
Posterior limb of internal capsule	FA	NS	NS	-
	MD	0.53 ± 0.076	0.62 ± 0.064	17.0 % ↑
	λ_{II}	1.00 ± 0.11	1.14 ± 0.10	14.0 % ↑
	$\lambda_{\perp}$	0.28 ± 0.074	0.36 ± 0.066	28.6 % ↑
Cerebral peduncles	FA	NS	NS	-
	MD (right)	0.50 ± 0.13	0.65 ± 0.15	30.0 % ↑
	λ_{II} (right)	1.03 ± 0.14	1.28 ± 0.12	24.3 % ↑
	$\lambda_{\perp}$	0.28 ± 0.081	0.39 ± 0.097	39.3 % ↑
Corpus callosum body, splenium and genu	FA (genu)	0.68 ± 0.074	0.57 ± 0.098	16.2 % ↓
	MD	0.63 ± 0.070	0.77 ±0.12	22.2 % ↑
	λ_{II}	1.23 ± 0.092	1.44 ± 0.11	17.1 % ↑
	$\lambda_{\perp}$	0.32 ± 0.088	0.45 ± 0.14	40.6 % ↑
Anterior limb of internal capsule	FA	NS	NS	-
	MD	0.52 ±0.076	0.63 ± 0.075	21.2 % ↑
	λ_{II}	0.88 ± 0.12	1.04 ± 0.11	18.2 % ↑
	$\lambda_{\perp}$	0.34 ± 0.082	0.43 ± 0.089	26.5 % ↑
External capsule	FA	NS	NS	-
	MD	0.61 ±0.057	0.72 ± 0.060	18.0 % ↑
	λ_{II}	0.88 ± 0.077	1.03 ± 0.078	17.0 % ↑
	$\lambda_{\perp}$	0.48 ± 0.065	0.57 ± 0.069	18.8 % ↑
WM adjacent to bilateral precentral gyri	FA	NS	NS	-
	MD	0.64 ± 0.059	0.74 ± 0.080	15.6 % ↑
	λ_{II}	0.93 ±0.074	1.06 ± 0.085	14.0 % ↑
	$\lambda_{\perp}$	0.48 ± 0.068	0.57 ± 0.091	18.8 % ↑
WM adjacent to bilateral	FA	NS	NS	-

Table 3-3 (contd.)

premotor cortex	MD	0.58 ±0.029	0.65 ± 0.035	12.1 % ↑
	λ_{II}	NS	NS	-
	$\lambda_{\perp}$	0.37 ± 0.051	0.43 ± 0.056	16.2 % ↑
WM adjacent to bilateral postcentral gyri	FA	NS	NS	-
	MD (right)	0.72 ± 0.10	0.85 ± 0.16	18.1 % ↑
	λ_{II}	1.02 ± 0.079	1.16 ± 0.12	13.7 % ↑
	$\lambda_{\perp}$ (right)	0.59 ± 0.12	0.72 ± 0.17	22.0 % ↑
WM adjacent to bilateral inferior frontal gyri	FA	NS	NS	-
	MD	0.55 ± 0.050	0.64 ± 0.057	16.4 % ↑
	λ_{II}	0.79 ± 0.029	0.90 ± 0.025	13.9 % ↑
	$\lambda_{\perp}$	0.41 ± 0.056	0.49 ± 0.067	19.5 % ↑
WM adjacent to bilateral superior temporal gyri	FA	NS	NS	-
	MD	0.63 ± 0.043	0.73 ± 0.058	15.9 % ↑
	λ_{II}	0.91 ± 0.049	1.04 ± 0.055	14.3 % ↑
	$\lambda_{\perp}$	0.50 ± 0.05	0.59 ± 0.064	18.0 % ↑
WM adjacent to bilateral middle temporal gyri	FA	NS	NS	-
	MD (right)	0.60 ± 0.035	0.68 ± 0.041	13.3 % ↑
	λ_{II}	NS	NS	-
	$\lambda_{\perp}$	0.43 ± 0.053	0.50 ± 0.060	16.3 % ↑
WM in parietal regions	FA	NS	NS	-
	MD	0.67 ± 0.050	0.75 ± 0.063	11.9 % ↑
	λ_{II}	0.98 ± 0.09	1.10 ± 0.10	12.2 % ↑
	$\lambda_{\perp}$	0.51 ± 0.061	0.58 ±0.080	13.7 % ↑
WM belonging to bilateral hippocampal formations	FA	NS	NS	-
	MD	0.61 ± 0.058	0.71 ± 0.057	16.4 % ↑
	λ_{II}	1.02 ± 0.11	1.16 ± 0.11	13.7 % ↑
	$\lambda_{\perp}$	0.41 ± 0.046	0.49 ± 0.049	19.5 % ↑

[*] *Differences are bilateral unless otherwise indicated.*

A ROI is considered significant if one or more skeleton voxels are significant
Mean and standard deviation values for fractional anisotropy (FA) are dimensionless.
NS: Not significant.
All mean and standard deviation values for mean diffusivity (MD), axial diffusivity (λ_{II}), and radial diffusivity ($\lambda_{\perp}$) are measured in 10^{-3} mm^2/sec.

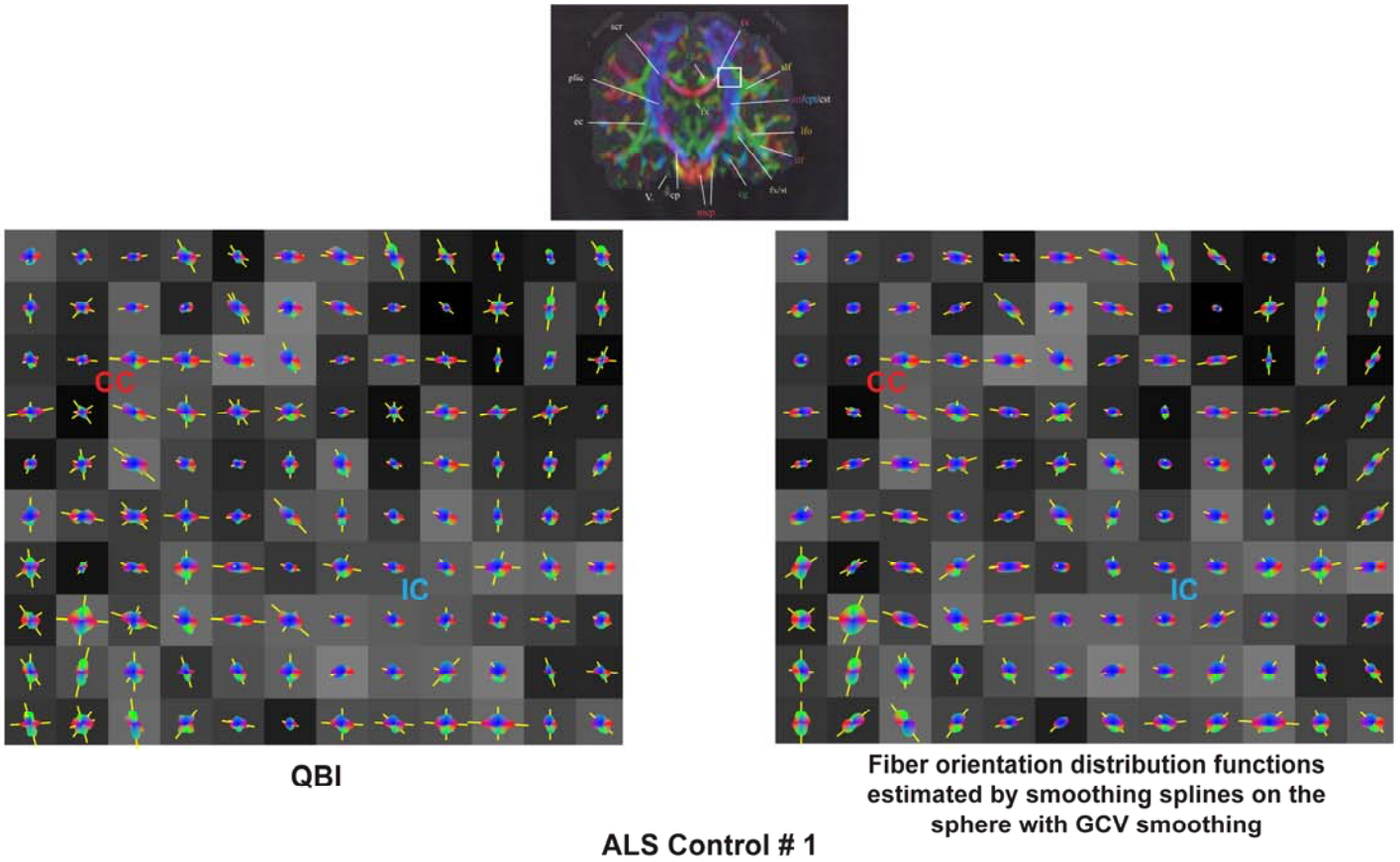

Figure 3.3 Generalized cross-validated (GCV) smoothing splines on the sphere orientation distribution functions (ODFs) show more consistency in dominant fiber orientation determination (yellow lines) (right panel). The QBI ODFs (left panel) still exhibit spurious ODF peaks in the corpus callosum (CC) projections and internal capsule (IC) projections. These spurious peaks often mislead fiber tractography. The upper panel shows a color-coded fractional anisotropy (FA) map with color correspondence of red for left-right oriented fibers, green for posterior-anterior oriented fibers and blue for inferior-superior oriented fibers. The white box in the upper panel outlines the region-of-interest (ROI) for which the QBI ODFs (left panel) and GCV Smoothing splines ODFs (right panel)from an amyotrophic lateral sclerosis (ALS) control are reconstructed.

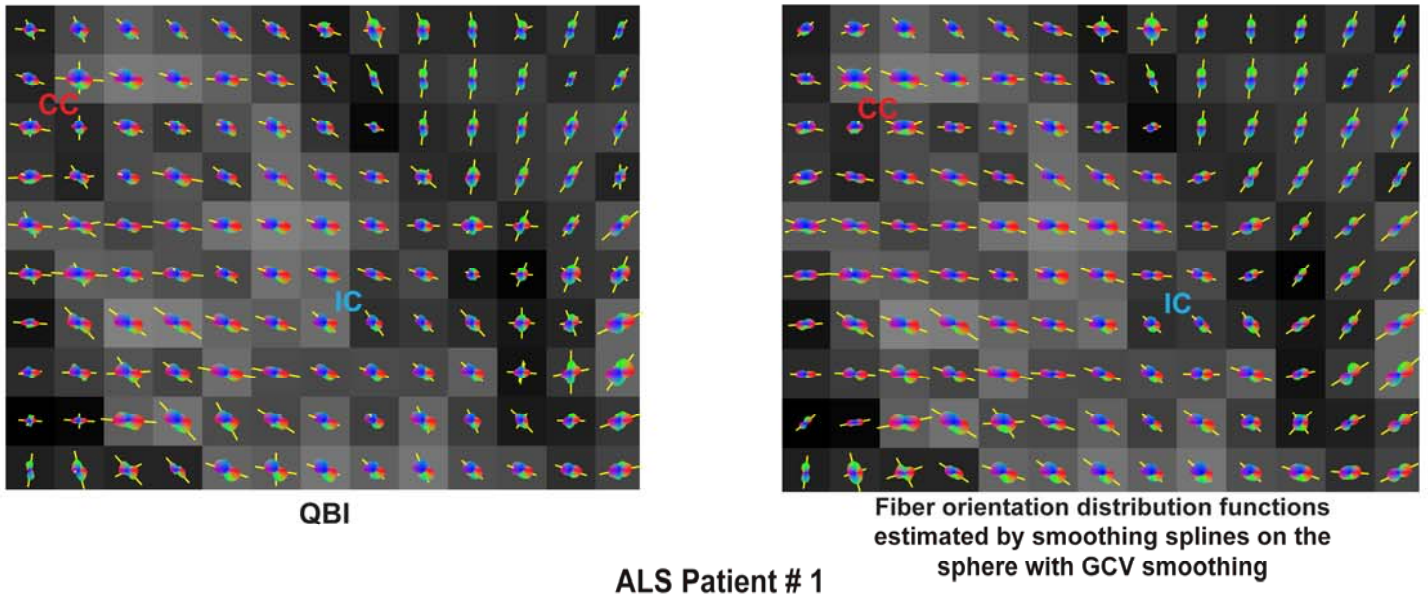

Figure 3.4 Generalized cross-validated (GCV) smoothing splines on the sphere orientation distribution functions (ODFs) (right panel) show more consistency in dominant fiber orientation determination (yellow lines) in this amyotrophic lateral sclerosis (ALS) patient. The region-of-interest (ROI) is the same as in Figure 3.3. The color correspondence is red for left-right oriented fibers, green for posterior-anterior oriented fibers and blue for inferior-superior oriented fibers.

The results of this study illustrate that DTI is sensitive to the neurodegenerative process that occurs in ALS, but the specific neuropathological substrate that underlies these DTI changes remains speculative. Unraveling the neurobiological basis for the observed DTI changes is difficult because of the complexity and dynamism of the underlying neuropathology in which various neuronal elements may be affected by different stages of the disease process at any point in time. An increase in $\lambda_{\perp}$ as seen in our results could potentially reflect either loss of integrity of the axonal wall or an increase in axonal diameter (31). In addition to the characteristic eventual atrophy and loss of motor neuron cell bodies and axons associated with ALS, common pathological changes of interest include the presence of ubiquitin-immunoreactive cytoplasmic inclusions in degenerating neurons, followed by a strong inflammatory reaction (32-35). Neuroinflammation is observed in pathologically affected areas of the brain and spinal cord from both ALS patients and mouse models of the disease (36). It is typically characterized by gliosis and the accumulation of large numbers of activated microglia and astroctyes. Astrocytes are relatively large glial cells and the phenomenon termed astrogliosis is an abnormal increase in the number of those astrocytes due to the destruction of nearby neurons. It has been suggested that inflammation could be occurring in the early presymptomatic phase of the disease (37). In a recent study attempting to define the effect of an inflammatory insult in developing rat pup brains after an inflammatory injury, increases in apparent diffusivity with associated increases in radial diffusivity in the corpus callosum corresponded, histologically, with widespread astrogliosis (38). And even though radial diffusivity increases have been typically attributed to myelin loss (39), the increases in this study occurred despite the absence of myelin at that

developmental stage in the rat pups' life indicating that radial diffusivity increases do not only occur as a result of loss of myelin. In our study, it could be speculated that the increases we see in diffusivity could be attributed to, at these early stages of disease, to a neuroinflammatory response accompanied by astrogliosis.

Other neurodegenerative processes may also contribute to the ALS associated changes found in our study. Neuropathological findings from almost all human ALS autopsy cases are of the terminal stages of the disease and provide limited insight on pathological changes during the course of the disease from onset. ALS animal models have been helpful in painting a general picture of changes associated with disease progression but fall short of replicating human ALS. Both longitudinal DTI human studies and DTI rodent studies with pathology would shed light on the relationship between changes in the DTI metrics and the neuropathology of ALS. Several other results are particularly noteworthy. We found a gradient in the changes in $\lambda_{\perp}$; these were most marked in the cerebral peduncles, less so in the IC and least so in the CR, consistent with the proposed dying-back hypothesis of axonal degeneration in ALS (40).

We also found that MD, $\lambda_{\parallel}$ and $\lambda_{\perp}$ were significantly increased in ALS patients in regions other than along the CST - the body, splenium and genu of the CC, as well as several other white matter structures. Our finding of abnormalities outside strictly motor areas is consistent with prior observations that ALS may be a multi-system degenerative disease (14, 20, 22, 41). Sach et al. reported finding significant decreases in FA in the entire CST, CC and thalamus in ALS patients (14) whereas other investigators in a more recent study found the

changes in the diffusion parameters to be diffuse throughout the brain, in the frontal, temporal and parietal lobes (20). In previous TBSS studies of FA changes in ALS, significant decreases were also found to be pervasive along the CST as well as in the frontal, temporal and parietal lobes (22, 23). Thus our findings of widespread changes in the diffusion parameters $\lambda_{\parallel}$ and $\lambda_{\perp}$ are not entirely surprising. Similarly unsurprising is the finding of such widespread evidence of the neurodegenerative process despite the relatively mild/early disease of patients included in this study; previous studies have found evidence for neurodegeneration even prior to symptom onset in people at risk for familial ALS (42). Degeneration of pyramidal tract bundles that connect the primary motor cortices across the CC may be partially responsible for the observed changes in DTI in the CC (43). In fact atrophy of the CC has been observed in advanced ALS using conventional MRI (44).

We were unable to show any correlation between the observed DTI changes and a variety of clinical measures of disease severity and duration. The evidence from prior studies in inconsistent in this regard (3, 13, 15, 17, 20). Possible explanations include heterogeneity of the disease and variability in the spectrum of disease duration and severity between different studies. The number of ALS patients in this study – twelve in number – may not be sufficient to show correlations. In addition, the ALSFRS-R scores of most of the twelve patients in the study was relatively high and the FVC percentage predicted values for a majority of those patients were in the normal ranges, Table 3-2, indicating that the patient pool is only mildly diseased. More importantly, the ALSFRS-R and FVC, as clinical measures, may not be entirely sensitive to the initial diffusivity changes occurring in the early stages of the disease.

Applying adaptive smoothing of the HARDI data via GCV smoothing splines on the sphere allows the reconstruction of ODFs for fiber tractography through areas of complex fiber crossings. GCV offers an adaptive and automatic means of smoothing the data guided by the SNR without the need for constant subjective trial and error in determining the amount of smoothing that is to be applied. The GCV smoothing spline ODFs are effectively smoothed showing less spurious ODF peaks compared to their QBI counterparts. Consistency or coherence metrics have been developed and applied in studies in the past with single tensor DTI (5, 45). A recent metric was defined as the mean dot-product of the eigenvector in a test voxel and the eigenvectors in its neighboring voxels. It measured the mean cosine for the angle between the principle directions in the test voxel and its neighbors. When considering a coherence metric for HARDI studies in which multiple fiber orientations could be estimated in a single voxel, a number of issues need to be taken into consideration. Of these include the correct identification of fiber pairs amongst multiple fiber orientations between neighboring voxels, the normalization constant in the coherence metric will most likely vary between each voxel and the next in a single ROI and finally the lack of an atlas gold standard for HARDI data displaying multiple fiber orientations.

Notwithstanding the many strengths of our study, it is also characterized by several weaknesses. Our image slices were relatively thick (5mm) with 2.5mm gaps between slides. The imaging parameters were selected to balance the trade-off between high quality images and limiting scan time for ALS patients. Increased slice thicknesses leads to partial voluming and a reduction in diffusion anisotropy. Although large slice thickness could potentially

hinder the skeletonizing step in TBSS, we did not encounter this problem. The FA skeletons for all subjects were individually examined and found to pass through the major white matter structures such as the CC, anterior and posterior limbs of the IC and external capsules. The mean FA skeleton overlaid on the mean FA image from all subjects was found to be relatively continuous through the averaged major white matter tracts within the imaging slices with few discontinuities (Figure 3.5). Additionally, the mean FA skeleton threshold value used in our analysis fell within the recommended range of values.

In summary, we report finding significant increases in MD, $\lambda_{\parallel}$, and $\lambda_{\perp}$ in ALS patients in regions along the CST and other white matter structures. Significant decreases in FA were only found in the CR of the CST. Changes in $\lambda_{\perp}$ were more widespread and more prominent than changes in the other DTI-derived measures we considered. Concurrent increases in $\lambda_{\parallel}$ and $\lambda_{\perp}$ may reduce the sensitivity of FA to detect neurodegenerative changes. MD is sensitive to changes in ALS, but lacks specificity to the components of change that are revealed with $\lambda_{\parallel}$ and $\lambda_{\perp}$. Furthermore, FA and MD may not adequately describe patterns of DTI changes that may vary with disease progression. These results suggest that $\lambda_{\perp}$ and $\lambda_{\parallel}$ are DTI–derived indices that have added utility as markers of neurodegeneration in ALS beyond the typical measures of diffusion anisotropy: FA and MD.

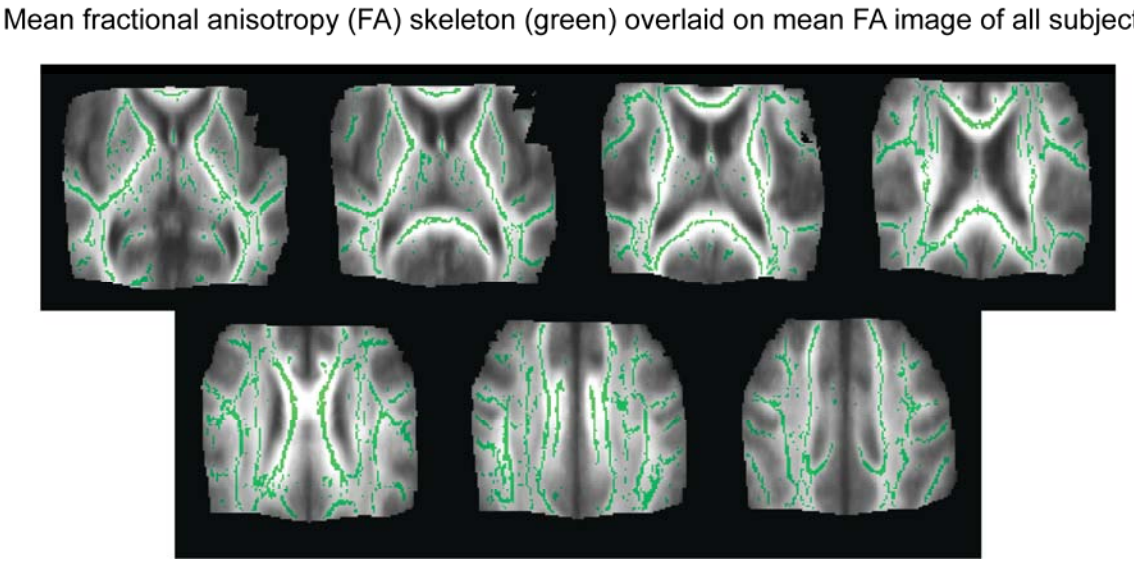

Figure 3.5 Mean fractional anisotropy (FA) skeleton is continuous in the major white matter tracts. The skeleton is fairly robust with few discontinuities in the major white matter tracts of all subjects such as the corpus callosum, anterior and posterior limbs of the internal capsule, external capsule and corona radiata among other white matter structures.

3.5 References

1. Wang S, Melhem ER. Amyotrophic lateral sclerosis and primary lateral sclerosis: The role of diffusion tensor imaging and other advanced MR-based techniques as objective upper motor neuron markers. Ann N Y Acad Sci 2005; 1064: 61-77.

2. Sica R, McComas A. Review of MUNE over 30 years. In: Motor Unit Number Estimation (MUNE): proceedings of the First International Symposium on MUNE, Snowbird, Utah, USA (Supplements to Clinical neurophysiology; Volume 55) edited by Bromberg, MB, Elsevier Science B.V.; Amsterdam, The Netherlands; 2003.

3. Hong YH, Lee KW, Sung JJ, Chang KH, Song IC. Diffusion tensor MRI as a diagnostic tool of upper motor neuron involvement in amyotrophic lateral sclerosis. J Neurol Sci 2004; 227(1): 73-78.

4. Horsfield MA, Jones DK. Applications of diffusion-weighted and diffusion tensor MRI to white matter diseases - a review. NMR Biomed 2002; 15: 570-577.

5. Basser PJ, Pierpaoli C. Microstructural and physiological features of tissues elucidated by quantitative-diffusion-tensor MRI. J Magn Reson B 1996; 111: 209-219.

6. Basser PJ. Inferring microstructural features and the physiological state of tissues from diffusion-weighted images. NMR Biomed 1995; 8: 333-344.

7. Le Bihan D, Mangin JF, Poupon C, Clark CA, Pappata S. Molko N, Chabriat H. Diffusion tensor imaging: concepts and applications. J Magn Reson Imaging 2001; 13: 534-546.

8. Basser PJ, Jones DK. Diffusion-tensor MRI: theory, experimental design and data analysis - a technical review. NMR Biomed 2002; 15: 456-467.

9. Mukherjee P. Diffusion tensor imaging and fiber tractography in acute stroke. Neuroimaging Clin N Am 2005; 15: 655-665.

10. Ge Y, Law M, Grossman RI. Applications of diffusion tensor MR imaging in multiple sclerosis. Ann N Y Acad Sci 2005; 1064: 202-219.

11. Kubicki M, Westin CF, McCarley RW, Shenton ME. The application of DTI to investigate white matter abnormalities in schizophrenia. Ann N Y Acad Sci 2005; 1064: 134-148.

12. Smith SM, Jenkinson M, Johansen-Berg H, Rueckert D, Nichols TE, Mackay CE, Watkins KE, Ciccarelli O, Cader MZ, Matthews PM, Behrens TE. Tract-based spatial statistics: voxelwise analysis of multi-subject diffusion data. Neuroimage 2006; 31: 1487-1505.

13. Ellis CM, Simmons A, Jones DK, Bland J, Dawson JM, Horsfield MA, Williams SC, Leigh PN. Diffusion tensor MRI assesses corticospinal tract damage in ALS. Neurology 1999; 53: 1051-1058.

14. Sach M, Winkler G, Glauche V, Liepert J, Heimbach B, Koch MA, Buchel C, Weiller C. Diffusion tensor MRI of early upper motor neuron involvement in amyotrophic lateral sclerosis. Brain 2004; 127: 340-350.

15. Graham JM, Papadakis N, Evans J, Widjaja E, Romanowski CA, Paley MN, Wallis LI, Shaw PJ, Griffiths PD. Diffusion tensor imaging for the assessment of upper motor neuron integrity in ALS. Neurology 2004; 63: 2111-2119.

16. Karlsborg M, Rosenbaum S, Wiegell M, Simonsen H, Larsson H, Werdelin L, Gredal O. Corticospinal tract degeneration and possible pathogenesis in ALS evaluated by MR diffusion tensor imaging. Amyotroph Lateral Scler Other Motor Neuron Disord 2004; 5: 136-140.

17. Cosottini M, Giannelli M, Siciliano G, Lazzarotti G, Michelassi MC, Del Corona A, Bartolozzi C, Murri L. Diffusion-tensor MR imaging of corticospinal tract in amyotrophic lateral sclerosis and progressive muscular atrophy. Radiology 2005; 237: 258-264.

18. Thivard L, Pradat PF, Lehericy S, Lacomblez L, Dormont D, Chiras J, Benali H, Meininger V. Diffusion tensor imaging and voxel based morphometry study in amyotrophic lateral sclerosis: relationships with motor disability. J Neurol Neurosurg Psychiatry 2007; 78: 889-892.

19. Wong JC, Concha L, Beaulieu C, Johnston W, Allen PS Kalra S. Spatial profiling of the corticospinal tract in amyotrophic lateral sclerosis using diffusion tensor imaging. J Neuroimaging 2007; 17: 234-240.

20. Sage CA, Peeters RR, Gorner A, Robberecht W, Sunaert S. Quantitative diffusion tensor imaging in amyotrophic lateral sclerosis. Neuroimage 2007; 34: 486-499.

21. Iwata NK, Aoki S, Okabe S, Arai N, Terao Y, Kwak S, Abe O, Kanazawa I, Tsuji S, Ugawa Y. Evaluation of corticospinal tracts in ALS with diffusion tensor MRI and brainstem stimulation. Neurology 2008; 70: 528-532.

22. Ciccarelli O, Behrens TE, Johansen-Berg H, Talbot K, Orrell RW, Howard RS, Nunes RG, Miller DH, Matthews PM, Thompson AJ, Smith SM. Investigation of white matter pathology in ALS and PLS using tract-based spatial statistics. Hum Brain Mapp 2009; 30: 615-624.

23. Sage CA, Van Hecke W, Peeters R, Sjibers J, Robberecht W, Parizel P, Marchal G, Leemans A, Sunaert S. Quantitative diffusion tensor imaging in amyotrophic lateral sclerosis: revisited. Hum Brain Mapp 2009, 30, 3657-3675.

24. Brooks BR, Miller RG, Swash M, Munsat TL. El Escorial revisited: revised criteria for the diagnosis of amyotrophic lateral sclerosis. Amyotroph Lateral Scler Other Motor Neuron Disord 2000; 1: 293-299.

25. Jenkinson M, Smith S. A global optimisation method for robust affine registration of brain images. Med Image Anal 2001; 5: 143-156.

26. Smith SM, Jenkinson M, Woolrich MW, Beckmann CF, Behrens TE, Johansen-Berg H, Bannister PR, De Luca M, Drobnjak I, Flitney DE, Niazy RK, Saunders J, Vickers J, Zhang Y, De Stefano N, Brady JM, Matthews PM. Advances in functional and structural MR image analysis and implementation as FSL. Neuroimage 2004; 23 Suppl 1: S208-219.

27. Andersson J, Smith SM, Jenkinson M. FNIRT - FMRIB's non-linear image registration tool. In: Proceedings of the 14th Annual meeting of the Organization for Human Brain Mapping (OHBM); June 17, 2008; Melbourne.

28. Nichols TE, Holmes AP. Nonparametric permutation tests for functional neuroimaging: a primer with examples. Hum Brain Mapp 2002; 15: 1-25.

29. Smith SM, Nichols TE. Threshold-free cluster enhancement: addressing problems of smoothing, threshold dependence and localisation in cluster inference. Neuroimage 2009; 44: 83-98.

30. Mori S, Wakana S, Van Zijl PCM. MRI atlas of human white matter, 1st ed. Amsterdam, The Netherlands; San Diego, CA: Elsevier, 2004.

31. Sasaki S, Maruyama S. Increase in diameter of the axonal initial segment is an early change in amyotrophic lateral sclerosis. J Neurol Sci 1992; 110: 114-120.

32. Bruijn LI, Miller TM, Cleveland DW. Unraveling the mechanisms involved in motor neuron degeneration in ALS. Annu Rev Neurosci 2004; 27: 723-749.

33. Rothstein JD. Current hypotheses for the underlying biology of amyotrophic lateral scelrosis. Ann Neurol 2009; 65: S3-S9.

34. Vickers JC, King AE, Woodhouse A, Kirkcaldie MT, Staal JA, McCormack GH, Blizzard CA, Musgrove REJ, Mitew S, Liu Y Chuckowree JA, Bibari O, Dickson T. Axonopathy and cytoskeletal distruption in degenerative disease of the central nervous system. Brain Res Bull 2009; 80: 217-223.

35. Glass CK, Saijo K, Winner B, Marchetto MC, Gage FH. Mechanisms underlying inflammation in neurodegeneration. Cell 2010; 140(6): 918-934.

36. McGeer PL, McGeer EG. Inflammatory processes in amyotrophic lateral sclerosis. Muscle Nerve 2002; 26: 459-470.

37. Vargas MR, Pehar M, Diaz-Amarilla PJ, Beckman JS, Barbeito L. Transcriptional profile of primary astrocytes expressing ALS-linked mutant SOD1. J Neuroscir Res 2008: 86: 3515-3525.

38. Lodygensky GA, West T, Stump M, Holtzman DM, Inder TE, Neil JJ. In vivo MRI analysis of an inflammatory injury in the developing brain. Brain Behav Immun 2010; 24(5): 759-767.

39. Song SK, Sun SW, Ramsbottom MJ, Chang C, Russell J, Cross AH. Dysmyelination revealed through MRI as increased radial (but unchanged axial) diffusion of water. Neuroimage 2002; 17(3): 1429-1436.

40. Fisher LR, Culver DG, Tennant P, Davis AA, Wang M, Castellano-Sanchez A, Khan J, Polak MA, Glass JD. Amyotrophic lateral sclerosis is a distal axonopathy: evidence in mice and man. Exp Neurol 2004; 185, 232-240.

41. Hammad M, Silva A, Glass J, Sladky JT, Benatar M. Clinical, electrophysiologic, and pathologic evidence for sensory abnormalities in ALS. Neurology 2007; 69: 2236-2242.

42. Agosta F, Rocca MA, Valsasina P, Sala S, Caputo D, Perini M, Salvi F, Prelle A, Filippi M. A longitudinal diffusion tensor MRI study of the cervical cord and brain in amyotrophic lateral sclerosis patients. J Neurol Neurosurg Psychiatry 2009; 80, 53-55.

43. Brownell B, Oppenheimer DR, Hughes JT. The central nervous system in motor neurone disease. J Neurol Neurosurg Psychiatry 1970; 33: 338-357.

44. Yamauchi H, Fukuyama H, Ouchi Y, et al. Corpus callosum atrophy in amyotrophic lateral sclerosis. J Neurol Sci 1995; 134: 189-196.

45. Klingberg T, Vaidya CJ, Gabrieli JD, Moseley ME, Hedehus M. Myelination and organization of the frontal white matter in children: a diffusion tensor MRI study. Neuroreport 1999; 10(13): 2817-2821.

CHAPTER 4

CONCLUSIONS

With the current advances in MRI scanner hardware, acquiring diffusion-weighted data with high angular resolution is now more feasible in a clinical setting. HARDI techniques have allowed the mapping of fiber tracts in areas of complex white matter fiber crossings via fiber tractography. Of the main drawbacks with HARDI is the depressed SNR levels of the data and images. This issue has prompted current research in ODF reconstruction from HARDI data to apply smoothing or regularization techniques to reconstruct smooth ODFs. The accuracy of fiber tractography is dependent on the performance of the varoius ODF reconstruction techniques in extracting dominant fiber orientations from the noisy HARDI data. This dissertation work attempts to address this issue by applying an objective and adaptive smoothing to the HARDI data via GCV with the smoothing splines on the sphere method (Chapter 2). The resulting ODFs sunsequently reconstructed from the smoothed diffusivity profiles required no subjective intervention of smoothing or regularization as existing QBI ODF reconstruction techniques do (Chapter 2).

In an application of HARDI to patients clinically diagnosed with ALS and in the early stages of the disease, changes in the radial diffusivity, $\lambda_{\perp}$, were more widespread and more prominent than changes in the other DTI-derived measures we considered (Chapter 3). The work in Chapter 3 represents the first reporting of significant changes in MD, axial and radial diffusivity in ALS using TBSS. The results suggest that $\lambda_{\perp}$ and $\lambda_{\|}$, which directly reflect

changes in the diffusion tensors, would be useful to consider in addition to the more commonly considered FA and MD to aid in revealing neurodegenerative changes in ALS. Applying adaptive smoothing of the HARDI data via GCV smoothing splines on the sphere allows the reconstruction of ODFs for fiber tractography through areas of complex fiber crossings. GCV offers an adaptive and automatic means of smoothing the data guided by the SNR without the need for constant subjective trial and error in determining the amount of smoothing that is to be applied. The GCV smoothing spline ODFs are effectively smoothed showing less spurious ODF peaks compared to their QBI counterparts.